Mechanics, Characterization, and Design of an Adaptive Variable Friction Base Isolation System

Sarah Bergquist

A thesis
submitted in partial fulfillment of the
requirements for the degree of

Master of Science in Civil Engineering

University of Washington

2019

Committee:

Paolo M. Calvi, Chair

Richard Wiebe

Jeffrey Berman

Program Authorized to Offer Degree:
Civil and Environmental Engineering

University of Washington

Abstract

Mechanics, Characterization, and Design of an Adaptive Variable Friction Base Isolation System

Sarah Bergquist

Chair of the Supervisory Committee:
Professor Paolo M. Calvi
Civil and Environmental Engineering

With the growing desire for high performing and resilient structures, base isolation has increasingly been utilized to reduce seismic forces on structures and further tailor structural response. Though many isolators are currently available, few offer the ability to tailor structural response at more than one demand level, and devices that are capable of performance-based design can be geometrically complex and have low damping at high displacements. Thus, the Adaptive Variable Friction (AVF) bearing is presented as a simple isolation alternative, capable of changing period as a function of ground motion intensity. This thesis studies the behavior of the AVF bearing and develops and tests a Direct Displacement Based Design process for single and multiple-degree-of-freedom systems (SDOF, MDOF), including an expression for equivalent viscous damping. Preliminary results from many nonlinear time history analyses show an advantage of AVF bearings over the commonly used Friction Pendulum in extreme events, achieving a lower maximum displacement for a similar maximum force and re-centering capability. Additionally, the proposed design process predicts the base shear and displacement of the system with reasonable precision at two demand levels, but improvements for the MDOF design should be made to better predict other structural responses. The results show that the AVF bearing is a promising isolation alternative capable of performance-based design and should be explored in further studies.

TABLE OF CONTENTS

LIST OF FIGURES

LIST OF TABLES

ACKNOWLEDGMENTS

Throughout the research process, I have received much support for which I am incredibly grateful. I would first like to thank my advisors, Professor Calvi and Professor Wiebe, for guiding me through the research process. You both were wonderful teachers and mentors, and though research was demanding at times, you both pushed me to do my best. I am grateful that you believed in me and my work. I am also grateful to Professor Berman for encouraging me to come to the University of Washington in the first place, and for serving on my defense committee.

My research was made possible in part to the University of Washingtons Valle Scholarship, which provided one year of funding, and the SERA fund, which sponsored the research project. I am thankful to both of these sponsors for making it financially possible for me to attend graduate school.

I had an incredible research partner, Andrew Yang, who answered countless questions about our research project. I am so thankful for your guidance, your lack of judgement, and your friendship. I would also like to thank Sandip Timsina, my predecessor, whose thesis I read countless times to learn more about variable friction isolation.

I am so grateful to all of the friends that I have made at University of Washington. To my cohort, Alec, Anne, Gloria, Kelsey, and Mitchell, I would not have wanted to suffer through graduate school with anyone else. From the countless homework assignments to the many projects, you all mean so much to me, and I hope that our friendship lasts long past the halls of More. I am also grateful to Tasha, Sarah, and Tom for being mentors and for always being willing to grab lunch and have a quick conversation.

My family has been supporting me academically long before I set foot at the University of

Washington. I would like to thank my parents for constantly sacrificing during my schooling so that I could succeed. Thank you for instilling a good work ethic and for only asking me to do my best; I hope I have made you proud. I am also grateful to my wonderful in-laws for supporting me as if I was their own, and to my grandparents for their love and encouragement. And to my new family, Blake: I could not have gotten through this program without your support. Thank you for cooking countless meals for me when I was too busy, being okay with me studying on the weekend, and for always helping me believe in myself. I love you.

Finally, I would like to thank God for being faithful in my doubts. I did not think that writing a thesis would be possible, but clearly I was wrong. I hope that this research can be used to help improve our world in a small way, making the world safer one base isolator at a time.

Chapter 1
INTRODUCTION

1.1 Motivation

Earthquakes are one of the most common and costly natural disasters that affect society. Their often deadly force perpetually disturbs millions worldwide, precipitating destruction and loss of life. In just the past decade, hundreds of thousands of people have been killed in earthquakes occurring from Nepal to Chile [Lackey, 2017]. This cost to society is felt not only through loss of life, but also in structural damage, lost economic revenue, and emotional distress. The 7.0 magnitude earthquake that struck Haiti in 2010 caused billions of dollars of damage to the economy and displaced more than 1.5 million people [Amadeo, 2019]. The effects from the earthquake had long lasting effects: as of 2017, over 55,000 people on the island were still homeless [UN, 2017]. Many of the structures affected by these earthquakes were designed with the primary objective of collapse prevention. Though this objective may preserve life, it results in severely damaged, uninhabitable buildings, greatly decreasing the resiliency of society.

One way to achieve more desirable structural behavior is to reduce the demand that the structure experiences, a task which can be accomplished using base isolation. Base isolation is currently one of the most advanced strategies for protecting structures from seismic loading. A simple period shift gives isolation its appeal: isolators have a low lateral stiffness, which increases the fundamental period of the system. Increasing the period usually results in a decreased acceleration demand, which decreases the forces experienced by the structure during an earthquake. The decrease in acceleration demand is generally accompanied by an increase in displacement demand, but this extra displacement demand is absorbed by the isolator. Many isolation devices also provide energy dissipation through lead cores or

added friction on sliding surfaces. This additional dissipation results in a a higher reduction of acceleration demands experienced by the structure, making isolation an efficient way to reduce acceleration demand on a structure.

The reduced acceleration demand provides many structural benefits. For example, base isolation allows a structure to stay elastic during a ground motion, something that would be unfeasible in a fixed-base structure. Experiments have shown that base isolation reduces floor accelerations, provides a more controlled displacement response, and lowers the force transmitted to the structure. Base isolation technology has the potential to improve the resiliency of cities and preserve human life following an earthquake, which is why it is important to continually research and improve this technology. This thesis will introduce and demonstrate the capabilities of a new isolation technology, coined the Adaptive Variable Friction (AVF) bearing, with the hope that AVF bearings can be offered as an alternative to existing bearings for achieving adaptive behavior.

1.2 Background

Historically, many versions of base isolation bearings have been studied and used in practice, with lead-rubber and friction bearings being the most common. The lead-rubber bearing is efficient at decreasing the demand on the super structure, but results in a large residual displacement of the system. Additionally, due to the yielding of the lead core these devices often need to be replaced following an earthquake.

The Friction Pendulum (FP) bearing is a popular isolation option, but can only be designed for one demand level, making it not effective in a performance-based context. For example, a small radius of curvature allows for a higher force capacity and small residual displacement and maximum force, making the device useful in rare seismic events. However, a higher activation force causes the device to not activate during a more frequent event, causing a large amount of force to be transferred to the structure. Conversely, a low friction coefficient allows the device to activate during a more frequent earthquake, but experiences excessive maximum displacements during rare events. Clearly, the FP has advantages in both

configurations, but cannot achieve desirable behavior for both frequent and rare earthquakes simultaneously.

The Double and Triple Friction Pendulum (DFP, and TFP, respectively) were introduced as an way to achieve adaptive behavior. The TFP especially has been shown experimentally to be effective at reducing force transferred to the structure while achieving multiple performance goals. However, the TFP has low energy dissipation at large displacements and a complex geometry, increasing the number of failure modes.

In the pursuit of alternative devices capable of achieving adaptive behavior, [Calvi and Ruggiero, 2016] proposed the use of Variable Friction (VF) systems. The BowTie and BowC VFS devices studied by [Timsina, 2017] showed improved behavior from the FP by reducing maximum displacement and force; yet, these devices are not capable of adaptive behavior. This research introduces and studies a variation of the VF device, the Adaptive Variable Friction (AVF) device. The AVF bearing can be used in a performance-based context and potentially offers improvement by having a simple geometry and high energy absorption at large displacements. The work presented in this thesis is promising, it is preliminary in nature, and further numerical and experimental work is needed to bring VF and AVF bearings into practice.

1.3 Objectives

The work of this thesis is part of a larger research project to better understand, model, and design VFS devices, with the ultimate goal of moving VFS devices into practical use. The objectives of this research, lettered below, align with two of the overall proposed research goals, numbered below:

1. Computationally explore promising applications of VFS:

   (a) Derive the behavior of the AVF bearings using a mechanics-based approach;

   (b) Develop numerical models for nonlinear time history analysis (NLTHA); and

(c) Characterize the behavior of AVF bearings and compare to existing isolation systems.

2. Develop a framework for the design of VF isolated structures:

   (a) Derive and validate an expression for estimating the damping ratio of AVF bearings to be used in design;

   (b) Adapt existing design procedures for AVF isolated single degree of freedom and multiple degree of freedom systems; and

   (c) Validate the postulated design process with a wide variety of input ground motions and case study structures.

These objectives will be achieved using one dimensional NLTH analyses performed with customized Matlab programs [MATLAB, 2018]. A series of single and multiple degree of freedom structures will be isolated by various AVF devices and subjected to a large suite of ground motions with both far-field and pulse characteristics. The results from these analyses will be used to evaluate both the viability of the proposed design procedures and the compare the performance of different AVF systems.

1.4 Thesis Outline

This thesis is organized into two parts, followed by overall conclusions:

- Part 1: *Mechanics and Characterization of the Adaptive Variable Friction Device.* This part discusses the history of friction bearings and respective modeling and mechanics, which informed the numerical modeling assumptions and algorithms employed in this thesis. The device mechanics are derived, and the isolator behavior is characterized using a parametric study using many non-linear time history analyses.

  – Chapter 2: *Mechanics Literature Review.* This chapter aims to provide context to this research by reviewing existing bearings, focusing on friction bearings. The

mechanics of previous devices are discussed alongside experimental findings and conclusions, which further show the need for alternative isolation technology, such as the AVF bearing.

  - Chapter 3: *Mechanics and Numerical Modeling of the Adaptive Variable Friction Device*. This chapter introduces the physical device and discusses its mechanics and force-displacement curve. Assumptions and the numerical modeling algorithms are defined and discussed. The ground motion selection, scaling, and spectra used throughout the thesis are also included.
  - Chapter 4: *Characterizing Behavior of the Adaptive Variable Friction Device*. With the modeling assumptions outlined, this chapter focuses on exploring the performance of an AVF bearing through evaluating hundreds of various devices with NLTHA. A discussion on the relationship between device parameters and overall performance is included.

- Part 2: *Design of Adaptive Variable Friction Base Isolated Systems*. With a better understanding of AVF device behavior, a design methodology is postulated and verified using both single and multiple degree of freedom systems. The damping of the device is estimated using a derived and validated damping expression.

  - Chapter 5: *Design Literature Review*. This review encompasses a comparison of base isolation design methods from various international codes, highlighting a lack of guidance. A case is built for using a direct displacement-based design (DDBD) approach for isolator and structure design and essential equations are reviewed.
  - Chapter 6: *Derivation and Verification of AVF Device Damping Properties*. The damping of a device must be estimated in order to calculate the reduction in demand from a spectrum. An equivalent viscous damping (EVD) expression is derived based on a Jacobsen approach, and is validated using many NLTH analyses.

  - Chapter 7: *Design Procedure, Verification, and Performance Comparison of AVF Base Isolated SDOF Systems*. Using the discussed DDBD approach and validated EVD expression, a design approach for a AVF isolated SDOF system is postulated. The design method is tested using a series of case study structures designed using a broad range of input parameters for the seismic demands of various U.S. cities. A comparison of analysis and design values for performance parameters give preliminary evidence on the reliability of the presented design process. The results allow comparison between equivalent Friction Pendulums and AVF bearings in a design setting.
  - Chapter 8: *Design Procedure and Performance Comparison of AVF Base Isolated MDOF Systems*. This chapter adapts the design process from Chapter 7 for a MDOF system. Various iterations of the design method are discussed and findings from design comparisons with NLTH analyses are presented. Given the limited number of MDOF case study structures studied, further study is required to evaluate the validity of the MDOF design process.

- Chapter 9: *Conclusions and Future Work*. Findings from this research are presented, outlining advantages and drawbacks to AVF bearing performance and the design method presented. Unexplored topics and additional areas of question are posed as topics for future work.

Part I

MECHANICS AND CHARACTERIZATION OF THE ADAPTIVE VARIABLE FRICTION DEVICE

Chapter 2

MECHANICS LITERATURE REVIEW

This chapter details previous research which forms the basis for this proposed work. A brief history of base isolation will be presented alongside a short overview of the most commonly used isolation bearings, with a focus on friction bearings. Experimental evidence validating the behavior of these devices will be discussed and a new category of friction bearings will be introduced as an alternative to currently available friction bearings.

2.1 Historic Overview of Isolation Systems

2.1.1 Pre-Modern Era

The first known record of seismic isolation dates back to 1870, when a U.S. patent for a double-concave rolling ball bearing was filed in San Francisco [Touaillon, 1870]. Later in 1909, Mario Viscardini patented a similar device; a more detailed description can be found in [Barucci, 1990]. Both devices were very similar to the modern Double Friction Pendulum device (discussed in Section 2.1.4). Though the device was never manufactured, the Viscardini device properties were estimated to have an average coefficient of friction, μ, of 0.4% and corresponding equivalent damping ratio of 3.2% [Calvi and Calvi, 2018]. The low friction and damping reduced the activation shear force, causing oscillations under low lateral loading such as moderate winds. A higher energy dissipation was unachievable at the time due to technology limitations.

2.1.2 Rubber and Lead-Rubber Bearings

Modern-day base isolation began in the 1960s with the New Zealand Department of Scientific and Industrial Research, with the development of the rubber bearing [Reys, 1993]. Later

in 1985, the first rubber-bearing isolated structure in the U.S. was built [Naeim and Kelly, 1999]. Modern rubber bearings consist of alternating layers of natural or synthetic rubbers with thin steel shim plates; these plates help to prevent excessive bulging and enhance the vertical stiffness of the bearing [Roeder et al., 1990] (Figure 2.1(a)). The steel shims, however, have no effect on the lateral stiffness of the system, which can be calculated as:

$$K_h = \frac{GA_b}{T_r}, \tag{2.1}$$

where G is the shear modulus, A_b is the bonded rubber area, and T_r is the thickness of the rubber. The damping ratios for natural rubber are lower than other isolation devices (between 2 and 3%); however, high damping rubber can reach damping ratios of 10-20% at 100% shear strain [Warn and Ryan, 2012].

Lead-rubber bearings were introduced in New Zealand in 1970s as a way to increase the damping capacity of the elastomeric bearing [Robinson, 1982]. These devices build on the rubber bearing by adding a lead plug core which yields under large lateral loads, dissipating additional energy; a schematic force-displacement curve can be seen in Figure 2.1(b). The horizontal stiffness of the isolator can be estimated using the the secant stiffness of the force-displacement curve, similar to a Friction Pendulum. The secant stiffness of a system can be calculated by dividing the force at maximum displacement by the maximum displacement ($V(\Delta_{max})/\Delta_{max}$). The mechanics and behavior of this device are described in more detail in [Naeim and Kelly, 1999]. Both the rubber and lead-rubber bearings have been used in practice due to their ability to mitigate seismic forces.

2.1.3 Friction Pendulum Bearings

In the 1980s, the first patent for a Friction Pendulum (FP) bearing was filed by Victor Zayas [Zayas, 1987]. The Friction Pendulum consists of a sliding bearing which rests on a spherical surface and is defined by radius of curvature R. The surface is typically polished to have a coefficient of friction between 7 and 18%, but it can vary from 3 to 20% [Warn and Ryan,

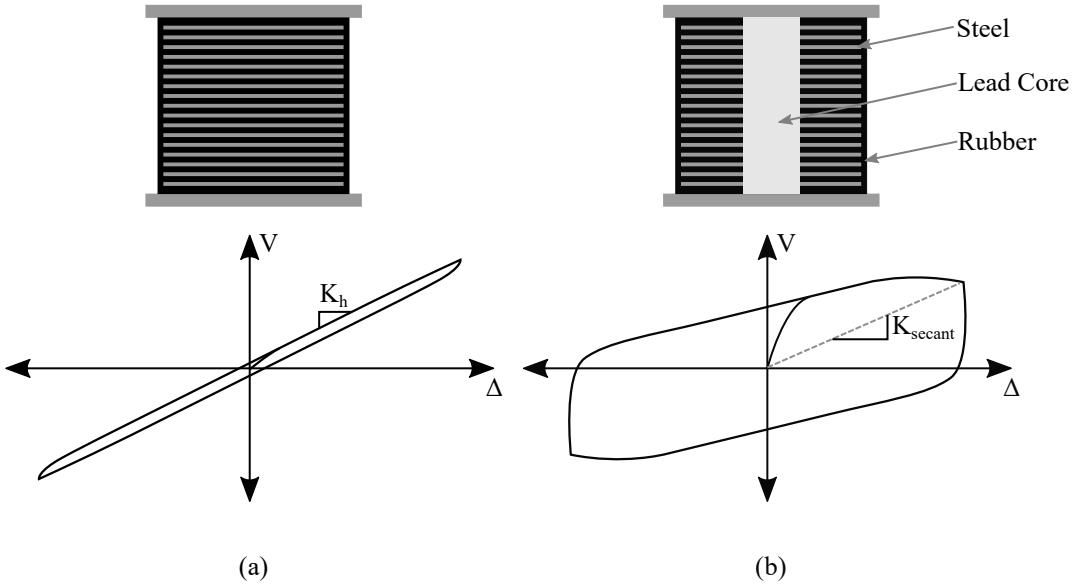

Figure 2.1: Cross sections and illustration of force-displacement curves for (a) Rubber and (b) Lead-Rubber bearings.

2012]. The curved sliding surface provides a restorative force and defines the horizontal stiffness of the device:

$$K_{FP} = \frac{W}{R}. \tag{2.2}$$

The device mechanics are derived from a simple pendulum, giving a period of:

$$T_{FP} = 2\pi\sqrt{\frac{R}{g}}. \tag{2.3}$$

The force displacement relationship of a Friction Pendulum can be found in Figure 2.2(a), and a more detailed description of Friction Pendulum mechanics follows in subsequent chapters.

Analytical studies on flat friction bearings performed by [Mostaghel and Tanbakuchi, 1983] showed the a friction device is relatively insensitive to variations in frequency content and amplitude, making them a robust option for seismic isolation. This favorable property, alongside high energy dissipation and good re-centering capabilities have made the Friction Pendulum the subject of thorough research, with studies performed by [Mokha et al., 1990;

Constantinou et al., 1990; Ceresa et al., 2004; Casarotti and Pavese, 2014], among others. The Friction Pendulum has been used in many real-world applications such as retrofitting the Benicia-Martinez bridge [Zayas et al., 2001], as well as rebuilding 4,500 apartments after the 2009 L'Aquila earthquake in Italy [Calvi, 2010].

Despite its wide range of potential applications, there are limitations associated with the device. Cost is a function of bearing size, so it can be costly to have high displacement capacities. Additionally, the FP cannot achieve optimal performance for more than one level of ground shaking [Fenz and Constantinou, 2008c]. These characteristics promoted research into a new iteration in the friction bearing called the Double Friction Pendulum.

2.1.4 Double Friction Pendulum Bearings

Though the idea for the Double Friction Pendulum (DFP) bearing was first introduced in 1870, the first known development and test was performed by [Hyakuda et al., 2001]. The DFP has two concave sliding surfaces which can have different R and μ values; details of the DFP mechanics can be found in [Fenz and Constantinou, 2006]. Varying the R and μ values allows the device to have a more adaptive behavior; however, a main benefit over the FP is the cost savings due to the decreased bearing size. The FP has an advantage over the DFP in moment transfer: the DFP transfers moment to both the upper and lower column, whereas the FP transfers moment to just one [Calvi and Calvi, 2018]. The DFP can be modeled as two FP in series, as shown in Figure 2.2(b).

2.1.5 Triple and Quadruple Friction Pendulum Bearings

The Triple Friction Pendulum was invented as a way to improve the adaptive behavior of friction bearings. The device has four sliding surfaces, which can be modeled as three FP bearings in series [Fenz and Constantinou, 2008b]. A cross sectional view and typical force-displacement curve can be found in Figure 2.2(c). There are some cases where the DFP can achieve adaptive behavior, but the TFP improves on this [Morgan, 2007]. The device

mechanics have been extensively characterized, modeled, and tested [Fenz and Constantinou, 2006, 2008a; Becker and Mahin, 2012], showing that the TFP can achieves adaptive behavior by limiting isolator displacements for rare earthquakes, while controlling drifts and accelerations at lower demands. Because of the favorable behavior, the TFP bearing has been applied in many real-world constructions, such as the Sabiha Gökçen International Airport in Turkey [Zekioglu et al., 2009] and the San Bernardino Court facility in California [Sarkisian et al., 2012].

Recently, the Quadruple Friction Pendulum (QFP) has been postulated by [Tsai et al., 2010] and modeled by [Lee and Constantinou, 2016]. Early testing shows additional adaptive behavior from the TFP, but the device is still in early development and has not been extensively tested or used in practice. A potential downside to the QFP and TFP bearings is the lack articulation on the innermost slider, which would make the bearing unstable [Sarlis and Constantinou, 2013]. Rotation capacity is important in some scenarios, such as adjusting to traffic loads on a bridge deck [Calvi and Calvi, 2018].

2.1.6 Tension-Capable Bearings

None of the friction bearings discussed provide any resistance to uplift force. This is important to consider when the isolator is on the perimeter of a slender structure or under a braced frame [Warn and Ryan, 2012]. The first isolator with tension capacity was used in 1990 for the Excel Minami-Koshigaya in Japan. The device had orthogonal steel arms which connected the structure and the foundation and interlock in the case of uplift. Little is known about the behavior of the device since the impact of the system on the structural behavior has not been addressed in detail [Roussis, 2009]. Another seldom used researched approach involves prestressing the isolator, proposed by [Logiadis et al., 1996], but it has been suggested that prestressing the bearing may impact the bearing performance [Roussis, 2009].

Most recently, the XY-FP was introduced by [Roussis and Constantinou, 2006], which consists of a set of orthogonal concave rails that allow the device behave as a Friction

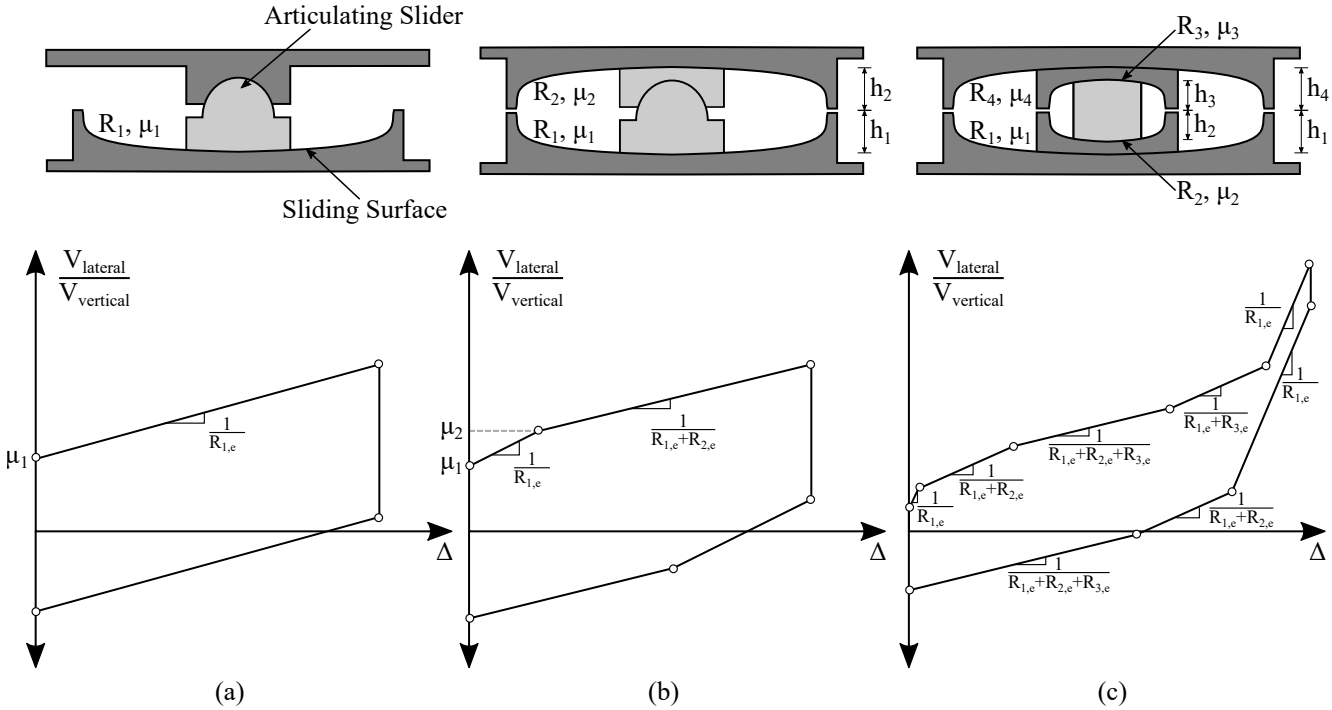

Figure 2.2: Cross sections and general force-displacement curves for (a) Friction Pendulum, (b) Double Friction Pendulum, and (c) Triple Friction Pendulum bearings. Note, $R_{i,e} = R_i - h_i$. Adopted from [Fenz and Constantinou, 2006, 2008b].

Pendulum, moving freely in the XY plane. The device has the same force-displacement as a FP in tension (shown in Figure 2.2), and a mirrored force-displacement in compression. The interlocking of the rails has been shown to provide tension resistance against uplift and has been used in both California and China [Roussis, 2009]. Despite having tension capabilities, none of these devices can achieve adaptive behavior.

2.1.7 Variable Frequency Bearings

An alternative approach for achieving adaptive behavior without the use of multiple sliding surfaces includes varying the radius of curvature on just one surface. The Variable Frequency Bearing, proposed by [Murnal and Sinha, 2002], has been analytically shown to reduce secondary super structure response more than an equivalent FP. The sliding profile is generally flatter than an equivalent FP, resulting in less inherent vertical acceleration. Despite promising preliminary results, the device has not yet entered real-world applications. Additionally, the changing curvature will need to be addressed with a new slider geometry.

2.2 Experimental Demonstration

An extensive set of shake table testing has paralleled isolator development in the past 40 years. Some of the earliest proof of concept tests for rubber and lead-rubber bearings were done at University of California's Earthquake Engineering Research Center [Kelly et al., 1980; Kelly and Hodder, 1981]. These early tests showed that higher levels of damping allowed for lower isolator displacements, but consequently increased floor accelerations. Real-world validation of these experiments are discussed in [Nagarajaiah and Xiaohong, 2000], where data from a lead-rubber isolated building in California showed that had significantly lower forces than an equivalent fixed-base structure.

Friction Pendulum bearings were first tested by [Zayas et al., 1987] using a 2-story frame with the isolators at the top of the first story. This test, as well as other tests conducted by [Mokha et al., 1990] and [Constantinou et al., 1990] showed that the early versions of the FP provided effective horizontal isolation. Additional tests have been performed regarding the

response of the structure from FP base isolation. [Wolff and Constantinou, 2004] measured floor accelerations on an isolated and scaled 6 story structure and showed that the story drifts, velocities and accelerations over a wide range of frequencies were reduced when using the FP.

As the FP family developed, the TFP became the focus of much experimentation due to its advantages over the FP and DFP bearings in adaptive behavior. A comprehensive suite of experiments performed by [Fenz and Constantinou, 2008b] and [Morgan, 2007] showed that the TFP was effective at limiting isolator displacements during extreme earthquake loading. As understanding of TFP behavior improved, testing began to move past proof-of-concept and scaled structures to full size shake table tests and more realistic loading schemes. A suite of full-scale, 5 story steel MRF structures were subjected to 3D loading on the world's largest shake table, E-Defense, in Japan [Ryan et al., 2012]. The tests revealed the importance a long-overlooked area in isolation research: vertical accelerations. The TFP protected the structure from damage in the horizontal direction, but coupling of the vertical and horizontal accelerations caused large amounts of nonstructural damage. Vertical accelerations are not typically considered in isolator design or experimentation, making this topic an open research area.

There is still a great deal of uncertainty in bearing behavior during extreme events. [Becker et al., 2017] recently tested a suite TFP isolated structures until failure. Each bearing failure mechanism was unique and occurred at a ground motion much higher than the design expectation. Two of the failures were related to the bearing geometry: in one, the inner slider turned on its side, and the other, the inner bearing separated. This highlights a potential advantage of the FP in failure scenarios; the FP has a less-complicated geometry, reducing the number of ways the device can fail.

2.3 Variable Friction Bearings

Variable friction bearings have been introduced as an alternative way to achieve adaptive behavior without geometric complexity. A Friction Pendulum with a continuously changing

friction profile was recently introduced by [Panchal and Jangid, 2009]. This device has a proposed friction profile for use in near-fault ground motions, but the profile could be adapted to accommodate other types of ground motions. When compared with an FP system, analytical results showed an that the variable friction bearings had an increased reduction in base shear and maximum isolator displacement. The results also showed that considering bi-directional effects is important for capturing the response of the structure; not considering this effect leads to underestimated displacements and overestimated accelerations. Though the results from the study were promising, the result was purely theoretical, as a continuously changing gradient of friction coefficients cannot currently be manufactured.

The predicted performance of [Panchal and Jangid, 2009]'s device prompted further investigation about the potential for variable friction devices, leading to [Calvi and Ruggiero, 2016]'s introduction of a different way to approach variable friction devices. In this approach, variable friction is achieved through a series of discrete concentric rings, with increased friction as one moves to the outside of the device. There exist an infinite set of combinations of ring size, number of rings, and friction values, giving the designer a great deal of flexibility when tailoring the force-displacement curve and the ability to achieve adaptive behavior. Variable friction could also be combined with multi-surface concepts, further increasing adaptive behavior and control over the hysteretic shape.

2.3.1 BowTie, BowC Systems

Two combinations of the variable friction devices, the BowTie and BowC, have been computationally studied [Calvi and Ruggiero, 2016; Calvi et al., 2016; Timsina and Calvi, 2018]. The BowC is defined by a radius of curvature, similar to a FP, but has concentric rings of varying size and friction values. The BowTie is a flat device and therefore has no restoring force; however, the device has a greater energy dissipation than the BowC. The rings and friction values can be designed in a way to achieve a linear force-displacement curve [Calvi and Ruggiero, 2016]. A typical force-displacement curve for the BowTie and BowC devices compared with a Friction Pendulum can be seen in Figure 2.3.

The properties of the BowTie and BowC devices have been thoroughly analytically and compared them to a Friction Pendulum System [Timsina, 2017]. In a comparison of NTLHA results for devices designed with the same maximum displacement and post-activation stiffness, the BowTie had a lower maximum displacement than the BowC and FPS, but had a much higher residual displacement and more variability. The highest maximum acceleration was experienced by the FPS, with the BowTie having the lowest maximum acceleration. Though the BowTie does not have re-centering capabilities, it is effective at limiting displacements and vertical accelerations due to its flat surface, making it economical and simple to produce. This device could be ideal for protecting low-mass elements that need to be immediately operable following an earthquake (such as an MRI machine) or for protecting temporary construction structures [Timsina, 2017]. The BowC improves on the behavior of the FP; it has very similar re-centering capabilities, yet experiences a lower maximum force and displacement.

The BowTie and the BowC are just two examples of ways in which variable friction can be used to tailor a hysteretic shape. Both the BowTie and the BowC offer improvements in force-displacement behavior, but neither offer adaptive behavior. The Adaptive Variable Friction (AVF) bearing presented in this work uses variable friction to produce a bi-linear hysteretic shape, making the device's period a function of earthquake intensity.

2.3.2 Adaptive Variable Friction Bearings

This research aims to introduce an Adaptive Variable Friction bearing (AVF), which offers potential improvements on existing devices and can be an alternative way to achieve adaptive behavior. The AVF bearing potentially has a higher energy dissipation capacity at large displacements than an equivalent TFP. Additionally, the simple geometry of the AVF bearing make it simpler to manufacture. This thesis characterizes the mechanics of the device and proposes and validates a design procedure for practical use. Additional concurrent research on the AVF bearing is discussing how to model the device in 3D, and considers bi-directional effects on performance [Yang et al., 2019a].

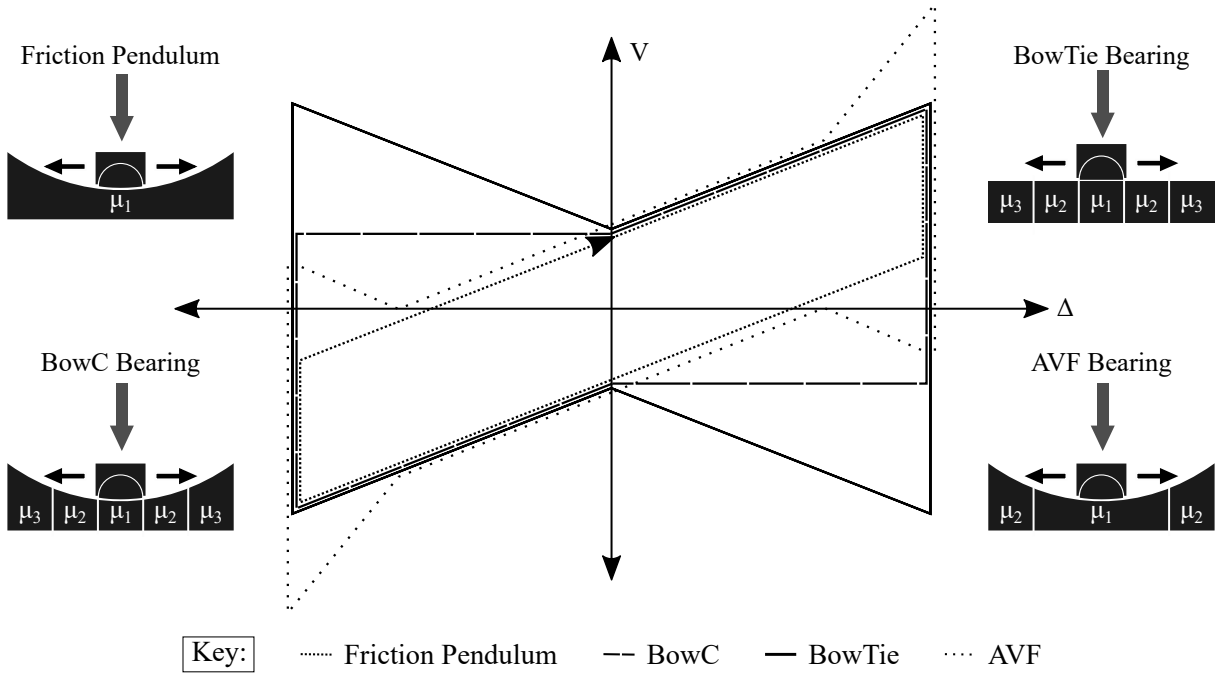

Figure 2.3: Force-displacement curves for Friction Pendulum, BowC, BowTie, and AVF Bearings

Chapter 3

MECHANICS AND NUMERICAL MODELING OF THE ADAPTIVE VARIABLE FRICTION DEVICE

While the Adaptive Variable Friction bearing is similar to other variable friction isolation devices such as the BowTie and BowC, the AVF bearing has yet to be explicitly defined numerically. The first section of this chapter discusses the physical features of the device and presents a qualitative force-displacement relationship for a generic AVF bearing. The second part outlines the assumptions made when modeling the AVF bearing in this study and shows the algorithm used in the nonlinear time history analyses. Additionally, the ground motions used throughout the study are defined.

3.1 Adaptive VFS Mechanics

3.1.1 Physical AVF Device

The Adaptive Variable Friction System, shown in Figure 3.1, consists of a fixed-base stainless steel spherical cap defined by radius of curvature R. Concentric rings on the spherical cap are defined by two friction and displacement values: the friction coefficients, μ_1 and μ_2 (note, $\mu_1<\mu_2$), correspond to the inner and outer rings, and the displacement demands, Δ_1 and Δ_2, correspond to two different demand levels that can be selected by the designer. In this study, Δ_1 will correspond to a Design Based Earthquake (DBE), having a return period of 475 years, and Δ_2 will correspond to the Maximum Considered Earthquake (MCE), which corresponds to a return period of 2475 years. An articulating slider of radius r_s is free to move throughout the device with a surface that is finished using a low-friction material, such as polytetrafluorethylene [Calvi et al., 2016]. The slider moves over the stainless steel base, which is treated to obtain the desired friction coefficients.

When a lateral load is greater than the activation force V_0 (or the weight of the structure multiplied with μ_1), the device will activate, at which point the friction between the low friction material and the steel plate provides energy dissipation and frictional resistance. Gravity provides a restorative force due to the curved surface, making the lateral strength and stiffness of the device a function of both the curvature of the sliding surface and the friction properties selected. Having a curved surface introduces the potential for damaging vertical fluctuation; however, this is mitigated by keeping the radius of curvature within the range of devices currently produced.

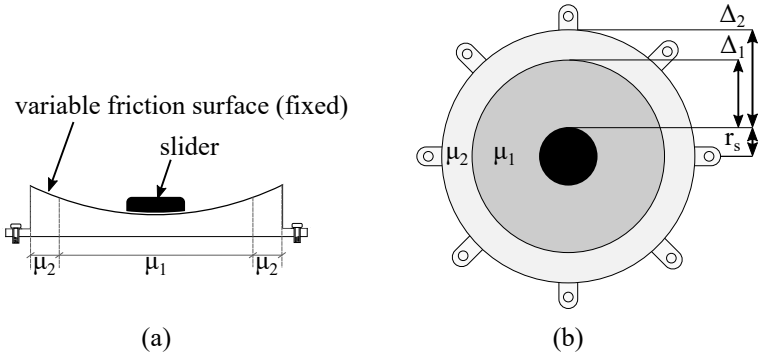

Figure 3.1: (a) Cross-sectional and (b) ariel view of an AVF device

3.1.2 Force Displacement Relationship for the AVF Device

A qualitative sketch of an AVF bearing force-displacement relationship response can be seen in Figure 3.2. The adaptive response of the device comes from the slider transitioning from the first to the second coefficient of friction. For this discussion, it is assumed that the axial stress is uniform over the slider area, that there is no difference between static and dynamic friction [Fagà et al., 2015], and that friction is well defined and perfectly stable. These assumptions could all be relaxed if necessary.

An AVF bearing has a perfectly rigid response until the device is activated at the activation force V_0. Once the device is activated, the slider begins to move with respect to the

bottom fixed plate, with lateral resistance coming from the area of the slider on the first ring as well as the curvature of the device (Figure 3.2(a)). As the slider transitions to the outer ring, the lateral resistance comes from both rings, proportional to the overlapping areas multiplied by the appropriate friction coefficients (Figure 3.2(b)). This transition is nonlinear depending on the sizes of the rings and their friction properties and can be described mathematically as:

$$V = \frac{W}{A}(A_1\mu_1 + A_2\mu_2) + \frac{W}{R}\Delta, \tag{3.1}$$

where R is the radius of curvature, Δ is the displacement of the slider, A is the area of the slider, and A_1 and A_2 are the areas of the rings that intersect with the slider [Calvi and Ruggiero, 2016].

When the load is reduced and reversed, the device will again exhibit a perfectly rigid response until it is activated in the opposite direction, which happens at a value that depends on the shape of the hysteresis curve and the input excitation. After activation, the lateral load required to push the slider back changes depending on the steepness of the second post-activation slope; an example stiffness is shown in Figure 3.2(c). The force-displacement curve is axisymmetric about the origin, and therefore the left side exhibits a mirrored response of the right side (Figure 3.2(d)).

The AVF device's force-displacement relationship is composed of two components: the restorative force of gravity, and the resistance from friction. The gravity force comes from the curved surface of the device, and the friction from the two different coefficients of friction on the device's surface. The restorative force has a slope of W/R, which can be derived from a simple pendulum. The frictional force comes from the static friction coefficient multiplied with the weight of the structure. Adding the gravity and frictional forces in parallel yields the AVF device's hysteretic shape, shown in Figure 3.3.

Also shown in Figure 3.3 is unintended behavior when the slider moves fully onto the second ring. It was previously shown that the adaptive behavior of the AVF bearing comes

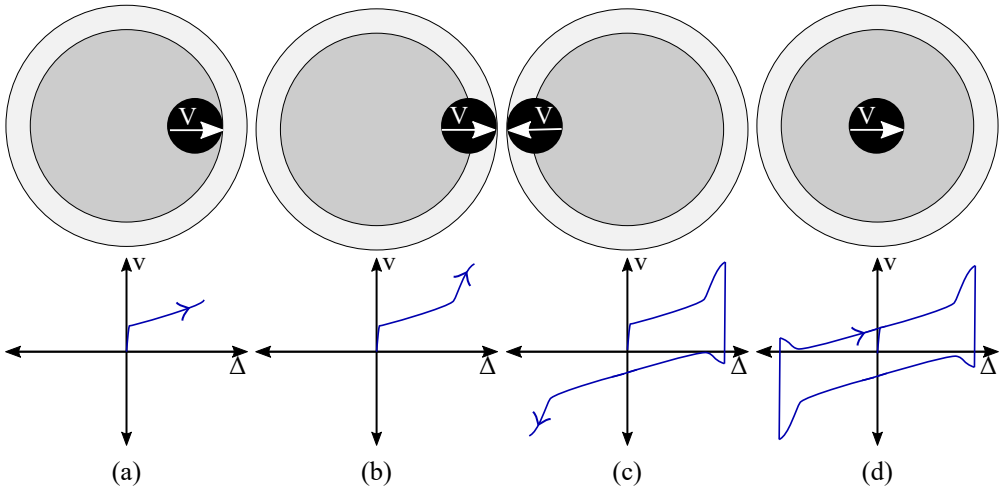

Figure 3.2: (a) Force-displacement response of AVF bearing at post-activation, (b) at maximum displacement, (c) at lateral load reversal, and (d) return to initial position

from the slider transitioning from the first to the second ring of friction. Once the slider is fully on the second ring, the slope of the force displacement relationship returns to what it was after initial activation, as seen in Figure 3.3. This is a valid VFS response, but this behavior is not included in this study. Therefore, the AVF device is designed so that the difference between Δ_1 and Δ_2 should be made equal to or less than the diameter of the slider in order to avoid the undesired hysteretic behavior.

3.2 AVF Device Numerical Modeling

3.2.1 Modeling Parameters

In order to model the hysteretic shape, a common language must be developed. Table 3.1 outlines the parameters developed in order to describe the AVF bearing hysteresis. As previously mentioned, in this study, the design levels 1 and 2 will refer to DBE and MCE, respectively. The shears corresponding to design levels 1 and 2 are V_1 and V_2, respectively.

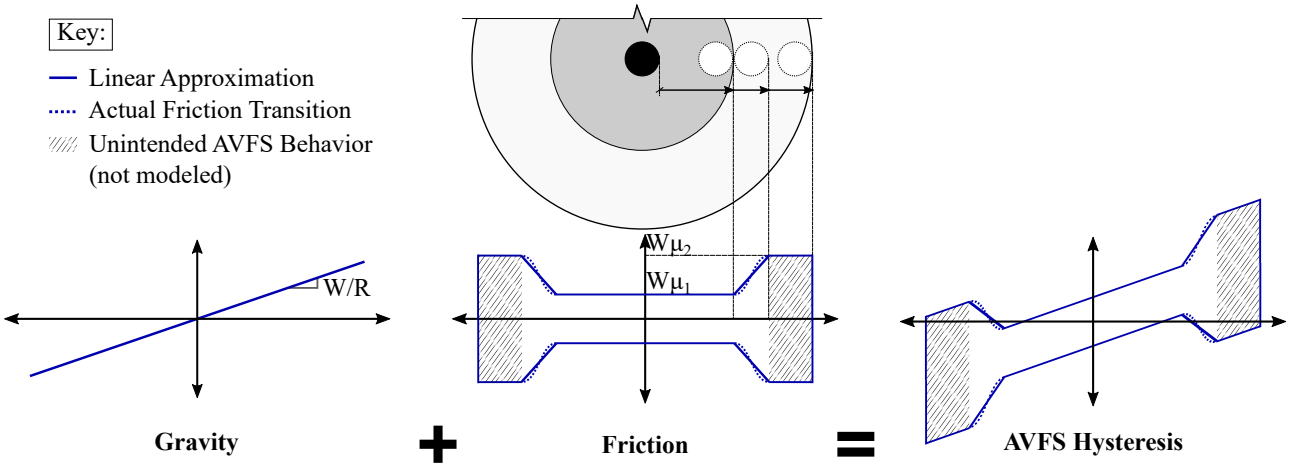

Figure 3.3: Components of the AVF bearing hysteresis.

The post activation stiffness of the system can be defined as:

$$K_1 = \frac{V_1 - V_0}{\Delta_1}. \tag{3.2}$$

The re-centering post activation stiffness can be defined as:

$$K_{1_{rec}} = \beta_1 K_1 = \frac{V_{1-} - V_{0-}}{\Delta_1}, \tag{3.3}$$

where β_1 represents the ratio between the re-centering and post activation stiffness. In this discussion, β_1 will always equal 1 (meaning the device behaves as a friction pendulum up to Δ_1). Different values of β_1 for a device with one design displacement have been studied extensively in [Timsina and Calvi, 2018].

The second post-activation stiffness defines the adaptive branch of the device, and can be calculated as:

$$K_2 = \beta_2 K_1 = \frac{V_2 - V_1}{\Delta_2 - \Delta_1}. \tag{3.4}$$

β_2, or the ratio between the second and first post-activation stiffness, is a critical design

parameter and will be discussed in detail in Chapter 4. Note this parameter helps to define the second coefficient of friction, μ_2.

The second post-activation re-centering stiffness can be derived by considering the components of stiffness. The gravity portion of stiffness, $K_{gravity}$, is the same as K_1 denoted earlier. The second post-activation stiffness, K_2, can be written as the sum of the stiffness from friction and gravity, or $K_{gravity} + K_\mu$. By plugging in β_2, K_μ can be written as:

$$K_\mu = \beta_2 K_1 - K_1. \tag{3.5}$$

When subtracting K_μ from $K_{gravity}$, the equation for the second post-activation re-centering stiffness can be simplified to:

$$K_{2_{rec}} = K_{gravity} - K_\mu = (2 - \beta_2)K_1 = \frac{V_{2-} - V_{1-}}{\Delta_2 - \Delta_1}. \tag{3.6}$$

Two key design parameters that control V_1 and V_2 are the parameters α_1 and α_2, defined below:

$$\alpha_1 = \frac{V_1}{V_0}; \tag{3.7}$$

$$\alpha_2 = \frac{V_2}{V_1}. \tag{3.8}$$

Finally, γ defines the relationship between the displacement parameters, and is defined as:

$$\gamma = \frac{\Delta_2}{\Delta_1}. \tag{3.9}$$

These relationships are used in both modeling of an AVF bearing and in design, and are summarized in Table 3.1.

Table 3.1: AVF bearing modeling parameters

Parameter	Symbol	Computation
Seismic Weight	W	User-Defined
Radius of Curvature	R	User-Defined
Slider Radius	r_s	User-Defined
Friction 1	μ_1	User-Defined
Friction 2	μ_2	From Iterative Design Process
Activation Force	V_0	Wμ_1
Negative Activation Force	V_{0-}	-Wμ_1
Design Force 1	V_1	$V_0 + K_1\Delta_1$
Negative Design Force 1	V_{1-}	$V_{0-} + K_{1_{rec}}\Delta_1$
Design Force 2	V_2	$V_1 + \beta_2 K_1(\Delta_2 - \Delta_1)$
Negative Design Force 2	V_{2-}	$V_{1-} + K_{2_{rec}}(\Delta_2 - \Delta_1)$
Activation Displacement	Δ_0	V_0/K_0
Plastic Offset	Δ_p	$\Delta_{current} - V_{current}/K_0$
Displacement 1	Δ_1	User-Defined
Displacement 2	Δ_2	From Iterative Design Process
Activation Stiffness	K_0	10,000K_1
Post-Activation Stiffness 1	K_1	W/R
Re-centering Stiffness 1	$K_{1_{rec}}$	$\beta_1 K_1$
Post-Activation Stiffness 2	K_2	$\beta_2 K_1$
Re-centering Stiffness 2	K_{2rec}	$(2 - \beta_2)K_1$
Force 1 Coefficient	α_1	V_1/V_0
Force 2 Coefficient	α_2	V_2/V_0
Displacement Coefficient	γ	Δ_2/Δ_1
Slope 1 Coefficient	β_1	K_{1rec}/K_1
Slope 2 Coefficient	β_2	K_2/K_1

3.2.2 Model Algorithm

In order to study the AVF device, a numerical model was developed to compute structural excitations resulting from input ground motions. Though the actual restoring force of the AVF bearing is nonlinear, [Calvi and Ruggiero, 2016] showed that in most applications, the hysteresis of a VFS system can be approximated using a linear, piecewise function as shown in Figure 3.4. Note that [Yang et al., 2019a] concurrently developed a 3D numerical element in OpenSees capable of modeling the exact behavior of all VFS devices and could be used in future studies for modeling the exact behavior.

Previously, [Calvi et al., 2016] suggested that in simple non-linear dynamic analyses, base isolators could be modeled using a lumped plasticity approach. The isolator is therefore modeled as a translational spring that gives the appropriate hysteresis for the device. Since few experiments have been conducted on VF systems, the hysteretic model is based entirely on the mechanical considerations presented in this chapter.

The expressions denoted in Figure 3.4 are presented in Equation (3.10), and are derived from the linear approximation of the hysteresis. Four assumptions are made regarding the initial stiffness of the device: 1) The initial stiffness K_0 should ideally be considered rigid, but is modeled as 10,000 times the first post activation stiffness for numerical convergence reasons, and is exaggerated in Figure 3.4 for visualization purposes; 2) It is assumed that this level of initial stiffness will not change the response of the isolator. From a small sensitivity study, such a large initial stiffness was shown to not affect analysis results; 3) The contribution of the initial stiffness to the first post activation stiffness, K_1, is negligible when added in series and is therefore neglected in the calculation of K_1; 4) Since the initial stiffness is large, the displacement at which the device will start to move (V_0/K_0) is negligible; it is therefore assumed in stiffness calculations that the activation force V_0 occurs at zero displacement (i.e. not at Δ_0).

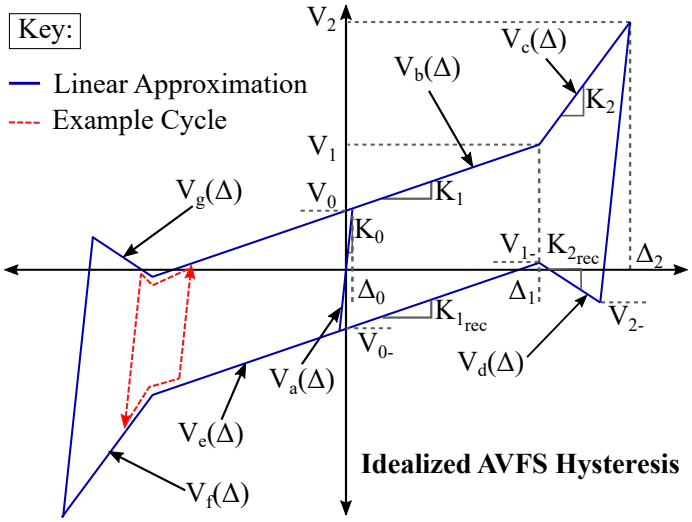

Figure 3.4: Idealized hysteretic response of AVF bearings used for numerical modeling

$$
\begin{aligned}
V_a(\Delta) &= K_0(\Delta - \Delta_p) \\
V_b(\Delta) &= V_0 + K_1\Delta \\
V_c(\Delta) &= V_0 + K_1\Delta_1 + \beta_2 K_1(\Delta - \Delta_1) \\
V_d(\Delta) &= -V_0 + K_1\Delta_1 + (2 - \beta_2)K_1(\Delta - \Delta_1) \\
V_e(\Delta) &= -V_0 + K_1\Delta \\
V_f(\Delta) &= -V_0 - K_1\Delta_1 + \beta_2 K_1(\Delta + \Delta_1) \\
V_g(\Delta) &= V_0 - K_1\Delta_1 + (2 - \beta_2)K_1(\Delta + \Delta_1)
\end{aligned}
\tag{3.10}
$$

The seven expressions presented in Equation (3.10) fully define the AVF bearing. The expressions are then used according to the algorithm outlined in Equation (3.11). Note, the plastic offset Δ_p is used to take into account the initial stiffness; it is calculated at each converged stage of the analysis. Also, the equations in (3.11) can either be the linear ones

presented in (3.10) or nonlinear depending on the level of accuracy desired.

$$V(\Delta) = \begin{cases} max[min(V_a(\Delta), V_b(\Delta)), V_e(\Delta)] \text{ if } -\Delta_1 \leq \Delta \leq \Delta_1 \\ max[min(V_a(\Delta), V_c(\Delta)), V_d(\Delta)] \text{ if } \Delta > \Delta_1 \\ max[min(V_a(\Delta), V_g(\Delta)), V_f(\Delta)] \text{ if } \Delta < -\Delta_1 \end{cases} \tag{3.11}$$

The analysis program for this study, written in MATLAB [MATLAB, 2018], uses linear acceleration Newmark-Beta algorithm for integration [Rosenblueth, 1971]. In order to minimize numerical errors, the well-known Newton-Raphson method is used to calculate the secant stiffness of the system [Chopra, 2014], which is summarized in Figure 3.5.

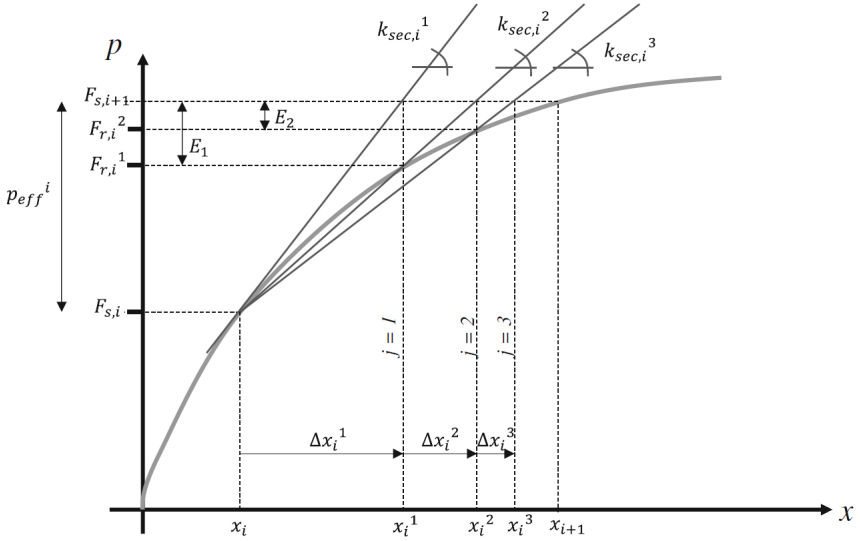

Figure 3.5: Secant stiffness calculation using Newton-Rhapson method [Calvi and Ruggiero, 2016]

μ_2 *Calculation*

The parameter μ_2 is dependent on the size of the slider, as shown in Figure 3.6. The transition between the first and second coefficients of friction is only as wide as the diameter of the slider. The slider diameter is selected by the designer and is dependent on what

pressure is desired; [Calvi and Calvi, 2018] recommends a pressure between 40-65 MPa. The μ_2 calculation is always based on the diameter of the slider, even if the slider does not fully enter the second ring of friction. The force at which the the slider is fully on the second ring, V_s, can be calculated as follows:

$$V_s = V_1 + \beta_2 \frac{W}{R} d_s, \tag{3.12}$$

where d_s is the diameter of the slider. The second coefficient of friction can be calculated by subtracting out the restorative gravity force:

$$\mu_2 = \frac{(V_s - \frac{W}{R}(\Delta_1 + d_s))}{W} \tag{3.13}$$

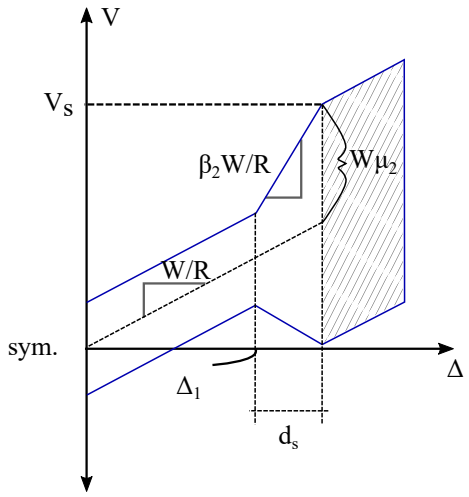

Figure 3.6: Calculation of second coefficient of friction.

Bi-Linear vs. Tri-Linear Model

As shown in Section 3.2.2, a tri-linear model would be needed to accurately describe AVF bearing behavior if the slider moves past being fully on the outer ring. However, the transition length is solely defined by the slider's diameter, a parameter which can be changed

Table 3.2: Ground motion selection requirements

Parameter	Units	Los Angeles	Portland	San Diego	San Francisco	Seattle
S_{MS}	[g]	2.43	0.99	1.22	1.50	1.37
S_{M1}	[g]	1.11	0.58	0.63	0.83	0.69
T_L	sec.	8	16	8	12	6

independently of design and analysis. Additionally, the intended behavior of the AVF bearing is to achieve a bi-linear hysteretic response. For both of these reasons, a bi-linear model was used for all NLTHA.

3.2.3 Ground Motions

Selection

A total of 60 pairs of ground motions were chosen for the study presented in this thesis. Ten unique pairs of far-field ground motions were selected from the PEER-NGA West 2 database to match the MCE demands of Los Angeles, Portland, San Diego, San Francisco, and Seattle. A set of pulse ground motions for San Francisco was also considered. All ground motions correspond to soil type C, or very dense soil and soft rock. Table 3.3 denotes the maximum spectral acceleration at short period (S_{MS}), the maximum spectral acceleration at one second (S_{M1}), and the long period (T_L) corresponding to a 5% damping as defined by ASCE 7-10 [ASCE 7-10, 2010].

Scaling

Once suitable ground motions for each city were selected, each component of the pair was scaled to match both DBE and MCE ASCE 7-10 design spectrums (i.e. 120 ground motions scaled for both DBE and MCE). When obtaining the ground motions from the PEER database, a scale factor is generated which matches the ground motion to an ASCE-defined

acceleration response spectrum. Since the ground motions for each event are given in trios (two orthogonal in horizontal directions and one in the vertical direction), PEER's scaling factor minimizes the error between all three directional response spectrums and the target spectrum. The numerical model used in this study is one dimensional, so a separate and more accurate scaling factor for each of the horizontal ground motion directions was found.

To find this scaling factor, a period range of two to five seconds was selected for matching the target and ground motion acceleration spectrum; between the periods of two to five seconds; this range was chosen to best reflect the typical period range of base isolation systems. For the length of the period range, the log of the difference between the design and scaled ground motion spectrum was calculated using square root of the sum of the squares, or SRSS. Using a log-based approach gives a better estimate of scale factor in this case since it more-closely reflects the shape of the acceleration spectrum at larger periods. The SRSS value was calculated for each increasing ground motion scale factor. The minimum SRSS value corresponded to the assigned scale factor.

The characteristics of the 60 pairs of ground motions and MCE scale factors used can be found in Table 3.3. Note that additional scale factors are applied to the ground motions later in the study as a means of varying intensity; this scale factor is used in addition to the scale factors in Table 3.3. The scaled displacement and acceleration spectrum for each city can be found in Figures 3.7 and 3.8. For all cities, it can be seen that the average spectra fits the design spectra well in the two to five second period range.

Table 3.3: Ground motion parameters

City	SN	RSN	Earthquake Name	Year	Magnitude	R_{rup} [km]	Directions	MCE Scaling
Los Angeles	1	322	$Coalinga-01$	1983	6.36	24.02	270, 360	5.11, 6.48
	2	549	$ChalfantValley-02$	1986	6.19	17.17	180, 270	5.37, 7.36
	3	880	$Landers$	1992	7.28	26.96	0, 90	10.0, 5.54
	4	3750	$CapeMendocino$	1992	7.01	25.91	270, 360	2.30, 5.56
	5	3954	$TottoriJapan$	2000	6.61	15.59	NS,EW	5.59, 10.0
	6	4855	$Chuetsu-okiJapan$	2007	6.8	27.15	NS,EW	7.73, 4.52
	7	5818	$IwateJapan$	2008	6.9	12.85	NS,EW	3.97, 2.06
	8	5829	$ElMayor-Mexico$	2010	7.2	13.71	0,90	2.75, 4.59
	9	6896	$DarfieldNZ$	2010	7	32.91	W, E	8.85, 8.70
	10	8102	$ChristchurchNZ$	2011	6.2	18.48	E, W	5.19, 9.67
Portland	11	13	$KernCounty$	1952	7.36	125.59	180, 270	10.0, 6.86
	12	20	$NorthernCalif-03$	1954	6.5	27.02	44, 314	1.78, 4.02
	13	28	$Parkfield$	1966	6.19	17.64	50, 320	7.59, 6.98
	14	36	$BorregoMtn$	1968	6.63	45.66	180,270	2.74, 3.14
	15	68	$SanFernando$	1971	6.61	22.77	90,180	1.91, 3.40
	16	138	$TabasIran$	1978	7.35	28.79	L1,T1	4.09, 3.21
	17	165	$ImperialValley-06$	1979	6.53	7.29	12,282	3.47, 2.63
	18	231	$MammothLakes-01$	1980	6.06	15.46	0,90	4.55, 6.90
	19	266	$VictoriaMexico$	1980	6.33	18.96	102,192	2.43, 1.85
	20	289	$IrpiniaItaly-01$	1980	6.9	17.64	0,270	5.98, 5.41
San Diego	21	6	$ImperialValley-02$	1940	6.95	6.09	180,270	2.85, 2.25
	22	15	$KernCounty$	1952	7.36	38.89	21,111	4.92, 4.72
	23	88	$SanFernando$	1971	6.61	24.87	172,262	4.35, 8.05
	24	175	$ImperialValley-06$	1979	6.53	17.94	140,230	2.62, 3.11
	25	176	$ImperialValley-06$	1979	6.53	21.98	140,230	4.06, 4.23
	26	289	$IrpiniaItaly-01$	1980	6.9	17.64	0,270	6.45, 5.83
	27	574	$TaiwanSMART1(45)$	1986	7.3	55.82	EW,NS	2.06, 2.08
	28	725	$SuperstitionHills-02$	1987	6.54	11.16	270,360	2.55, 2.17
	29	730	$SpitakArmenia$	1988	6.77	23.99	0,90	3.72, 7.47
	30	731	$LomaPrieta$	1989	6.93	41.88	1,90	3.49, 4.01
San Francisco	31	827	$CapeMendocino$	1992	7.01	19.95	0,90	2.33, 2.68
	32	850	$Landers$	1992	7.28	21.78	0,90	2.90, 5.37
	33	1155	$KocaeliTurkey$	1999	7.51	60.43	0,90	3.28, 3.15
	34	1194	$Chi-ChiTaiwan$	1999	7.62	19.07	E,N	1.74, 2.07
	35	1211	$Chi-ChiTaiwan$	1999	7.62	39.02	N,W	2.71, 2.82
	36	1762	$HectorMine$	1999	7.13	43.05	90,360	4.30, 3.89
	37	3758	$Landers$	1992	7.28	36.93	45,135	1.38, 1.38
	38	5985	$ElMayor-Mexico$	2010	7.2	23.42	360,90	1.90, 1.50
	39	6923	$DarfieldNZ$	2010	7	30.53	N15E,S75E	1.70, 1.45
	40	6953	$DarfieldNewZealand$	2010	7	24.55	W,S	2.48, 4.98
San Francisco (pulse)	41	838	$Landers$	1992	7.28	34.86	0,90	4.82, 3.57
	42	1148	$KocaeliTurkey$	1999	7.51	13.49	0,90	7.59, 3.13
	43	1486	$Chi-ChiTaiwan$	1999	7.62	16.74	E,N	3.18, 2.67
	44	1602	$DuzceTurkey$	1999	7.14	12.04	0,90	2.04, 3.25
	45	3746	$CapeMendocino$	1992	7.01	18.31	270,360	2.57, 2.29
	46	3965	$TottoriJapan$	2000	6.61	6.88	NS,EW	2.29, 4.52
	47	4228	$NiigataJapan$	2004	6.63	8.93	NS,EW	3.98, 4.07
	48	4847	$Chuetsu-okiJapan$	2007	6.8	11.94	NS,EW	2.01, 1.88
	49	6942	$DarfieldNZ$	2010	7	26.76	E,W	1.52, 2.52
	50	8161	$ElMayorMexico$	2010	7.2	11.26	360,90	1.63, 2.03
Seattle	51	12	$KernCounty$	1952	7.36	117.75	90,180	4.88, 9.28
	52	93	$SanFernando$	1971	6.61	39.45	143,233	5.91, 5.62
	53	122	$FriuliItaly-01$	1976	6.5	33.4	0,270	9.84, 10.0
	54	125	$FriuliItaly-01$	1976	6.5	15.82	0,270	8.27, 7.13
	55	162	$ImperialValley-06$	1979	6.53	10.45	225,315	5.05, 4.40
	56	163	$ImperialValley-06$	1979	6.53	24.6	225,315	4.38, 4.79
	57	164	$ImperialValley-06$	1979	6.53	15.19	147,237	6.09, 4.27
	58	167	$ImperialValley-06$	1979	6.53	15.3	15,285	8.03, 8.99
	59	286	$IrpiniaItaly-01$	1980	6.9	21.26	0,270	2.71, 4.65
	60	313	$CorinthGreece$	1981	6.6	10.27	L,T	4.41, 5.03

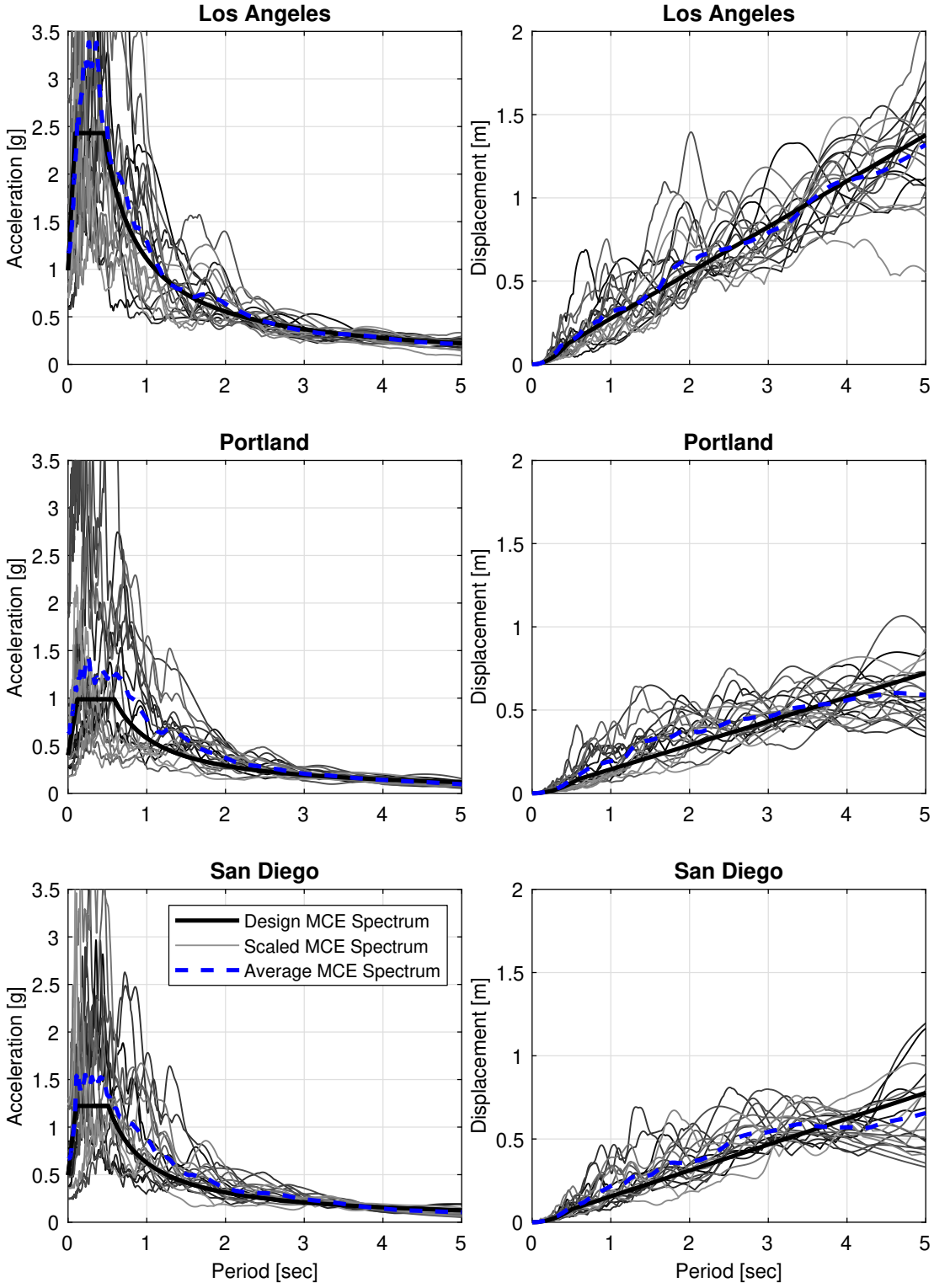

Figure 3.7: MCE Spectral Acceleration and Displacement Part 1

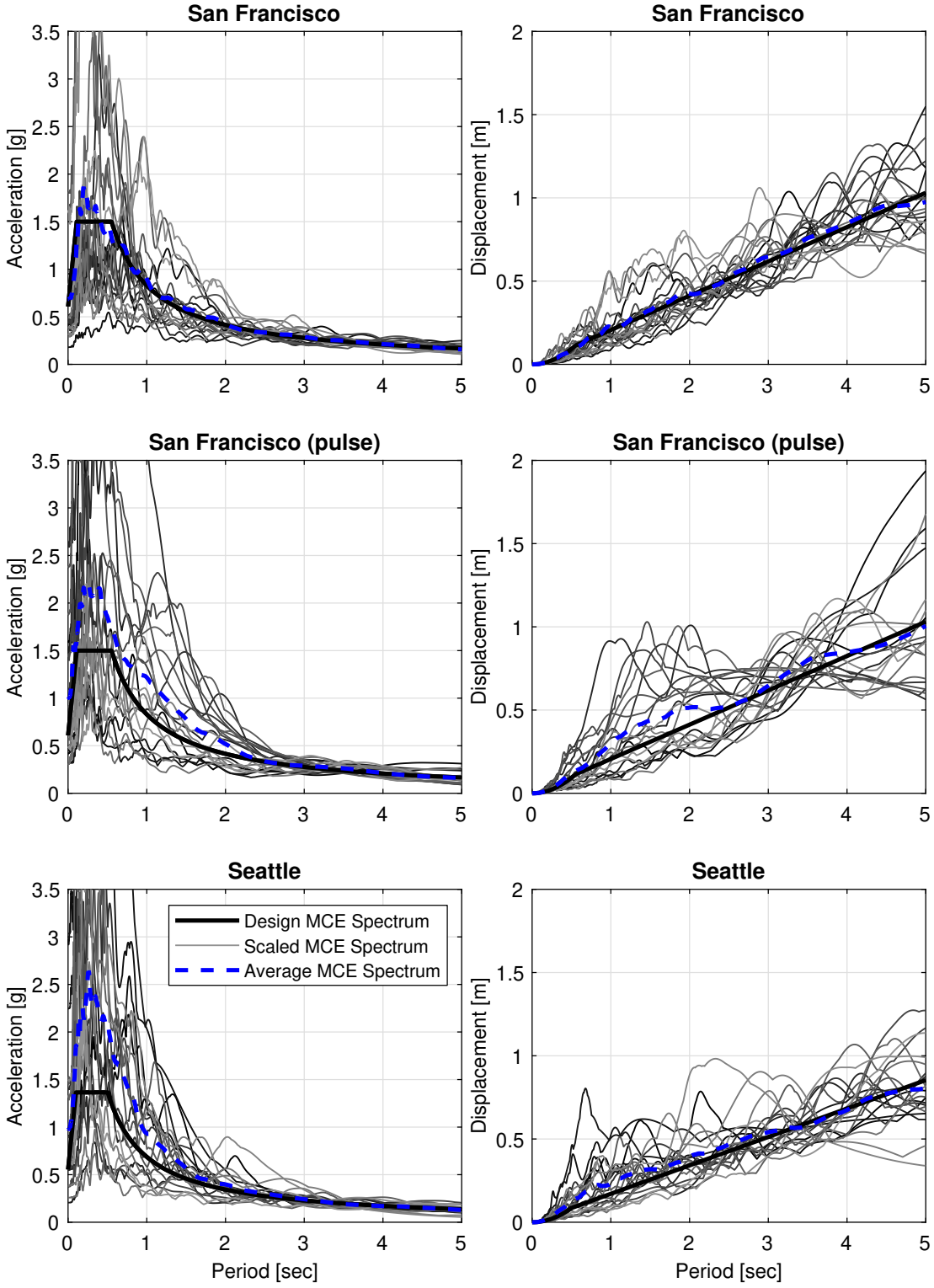

Figure 3.8: MCE Spectral Acceleration and Displacement Part 2

Chapter 4

CHARACTERIZING BEHAVIOR OF THE ADAPTIVE VARIABLE FRICTION DEVICE

4.1 Overview

Now that the mechanics of the device are defined, it is appropriate to characterize it's behavior. This chapter explores the behavior of an Adaptive VFS isolating a rigid single degree of freedom structure, focusing on characterizing the behavior of the device itself. A parametric study is conducted by performing many NLTH analyses on numerous AVF devices in order to explore the device's behavior. Through studying how the AVF bearing performs, a designer can have a more informed decision on how to pick device parameters. The parameters of interest, namely maximum displacement, maximum force, and residual displacement, are discussed and compared between different AVF devices as well as with a Friction Pendulum, leading to suggestions for optimal parameters.

4.2 Assumptions and AVF Devices Studied

In order to thoroughly characterize device behavior, all combinations of the parameters shown in Table 4.1 were used for analysis, resulting in 840 devices studied. These devices were similar to those used in the damping validation and reflect parameter ranges of what is currently manufactured. The vertical load applied to the isolator was normalized to be 1, since the weight is a nearly linear-proportional property in the analysis (this means that the y-intercept on the hysteresis can be taken as μ_1). Since a bi-linear numerical model is being used, the diameter of the slider has no effect on the numerical model, and is therefore not specified.

Table 4.1: Isolator parameters considered in SDOF parametric study (Low:Step:High)

R [m]	β_2	Δ_1 [m]	μ_1 [%]	Scale Factor
1.5:0.5:5	1:1:5, 7, 9	0.1:0.1:0.5	3, 5, 8	0.5:0.5:2.5

4.2.1 Selection of β_2 vs. μ_2

Many combinations of parameters can be used to define an AVF bearing. It was decided to select the parameter β_2 to define the bearing in this analysis instead of μ_2. Calculating μ_2 is dependent on the size of the slider, which as previously mentioned can be changed independently of design and analysis. Additionally, the second post-elastic stiffness is more easily controlled by scaling it with β_2 than finding combinations of μ_2 and the slider diameter that will give an equivalent slope. Since the goal of this study was to look at as many hysteresis combinations as possible in order to widely characterize behavior, ease of changing the hysteretic response was preferred and therefore β_2 was varied explicitly. Lastly, β_2 is unitless.

4.2.2 Effect of Structural Properties on Isolator Properties

This chapter aims to study the behavior of the isolator alone; interaction of the structure with the isolator will be studied in Part II of the thesis. Because of this, the structure on top of the isolator in this study was modeled as rigid with a damping value of 0%. It is possible to study just the isolator behavior since the rigid SDOF structure selected for this parametric study has little effect on the device behavior. This was based on the conclusions of [Timsina and Calvi, 2018], who in a smiliar parametric study was able to show that the performance of the base isolators was not affected by the dynamic properties of the supported structure. However, it is important to note that the performance of the overall (e.g. nonstructural, superstructure drifts) system would be affected by the supported structure's properties.

4.3 NLTHA Damping Estimation and Procedure

Damping in NLTH analyses was estimated by matching the maximum displacement of a nonlinear system with an equivalent linear system using the secant stiffness. The maximum force and displacement from the nonlinear analysis are recorded and used to calculate the nonlinear system's secant stiffness, which is then assigned as the linear system's stiffness. The linear system then undergoes repeated linear time history analyses where damping is incrementally increased until the maximum displacements of the original and linear system are equal. The damping value where the two systems have equal maximum displacement is the damping value assigned to the nonlinear system.

The analyses were performed using the customized MATLAB script discussed in Chapter 3.2.2. The ten pairs of non-pulse ground motions corresponding to San Francisco's MCE design spectrum were used for the analyses, which are outlined in Chapter 3.2.3. The five scale factors denoted in Table 4.1 were applied in addition to the ground motion scale factors used to match the design spectrum. The twenty ground motions, five scale factors, and 840 devices resulted in over 80,000 NLTH analyses in the parametric study.

4.4 Parametric Study Results

Presenting five AVF bearing variables (R, Δ_1, μ_1, β_2, and the ground motion scale factor) alongside the response parameters of interest requires five different independent variable axes and n different dependent axes for displaying the data from the study; the presentation of these variables can be seen in Figures 4.1 - 4.3. Each individual subplot shows the parameter of interest vs. radius of curvature, R. The lines on each subplot represent the average of the parameter of interest from the 20 ground motions for different β_2 values. The global x-axis varies with Δ_1, and the global y-axis varies with the ground motion scale factor. This matrix of graphs was repeated three times, one for each μ_1 value. The results are insensitive to μ_1, so only $\mu_1 = 5\%$ is presented.

The maximum isolator force for the different AVF devices, ground motions, and scale

factors can be seen in Figure 4.1. Note that the force in the SDOF structure is the same as the force in the isolator since the SDOF system is rigid; therefore, the maximum acceleration will follow the same trend as the maximum force and is not presented. The maximum force increases with increasing β_2 and decreases with increasing R. When the scale factor is low, the device does not reach the second post activation stiffness, which means the device behaves as a Friction Pendulum. When this happens, changing β_2 has little effect on the behavior, which can be seen when SF = 0.5. There is little difference between the Friction Pendulum ($\beta_2 = 1$) and the first considered adaptive device ($\beta_2 = 2$) for all parameter combinations considered.

The residual displacement is a measurement of of how well the device re-centers at the end of the ground motion. The results from the NLTH analyses of the systems studied can be seen in Figure 4.2. Overall, the residual displacement does not change greatly with increasing radius of curvature. The larger the scale factor and β_2, however, the higher the residual displacement. Even for high scale factors, the Friction Pendulum ($\beta_2 = 1$) and the first adaptive device studied ($\beta_2 = 2$) have the same residual displacement. This means that some AVF devices have the same re-centering properties regardless of the ground motion intensity.

The maximum displacement experienced by the isolator can be seen in Figure 4.3. The maximum displacement increases linearly a nominal amount with increasing R, Δ_2, and scale factor. Overall, the highest β_2 values produce the lowest maximum displacement, with a largest difference between $\beta_2 = 1$ and 2. When the ground motion is most intense, there is a large difference in maximum displacement between a Friction Pendulum and an adaptive device. This difference shows that an adaptive device could be beneficial in very intense ground motions if a designer is constrained by displacement.

4.4.1 Trade-Offs and Parameter Suggestions

From the SDOF parametric study, it is clear that there are trade-offs when the parameters of interest are considered. When choosing device parameters, a designer should consider

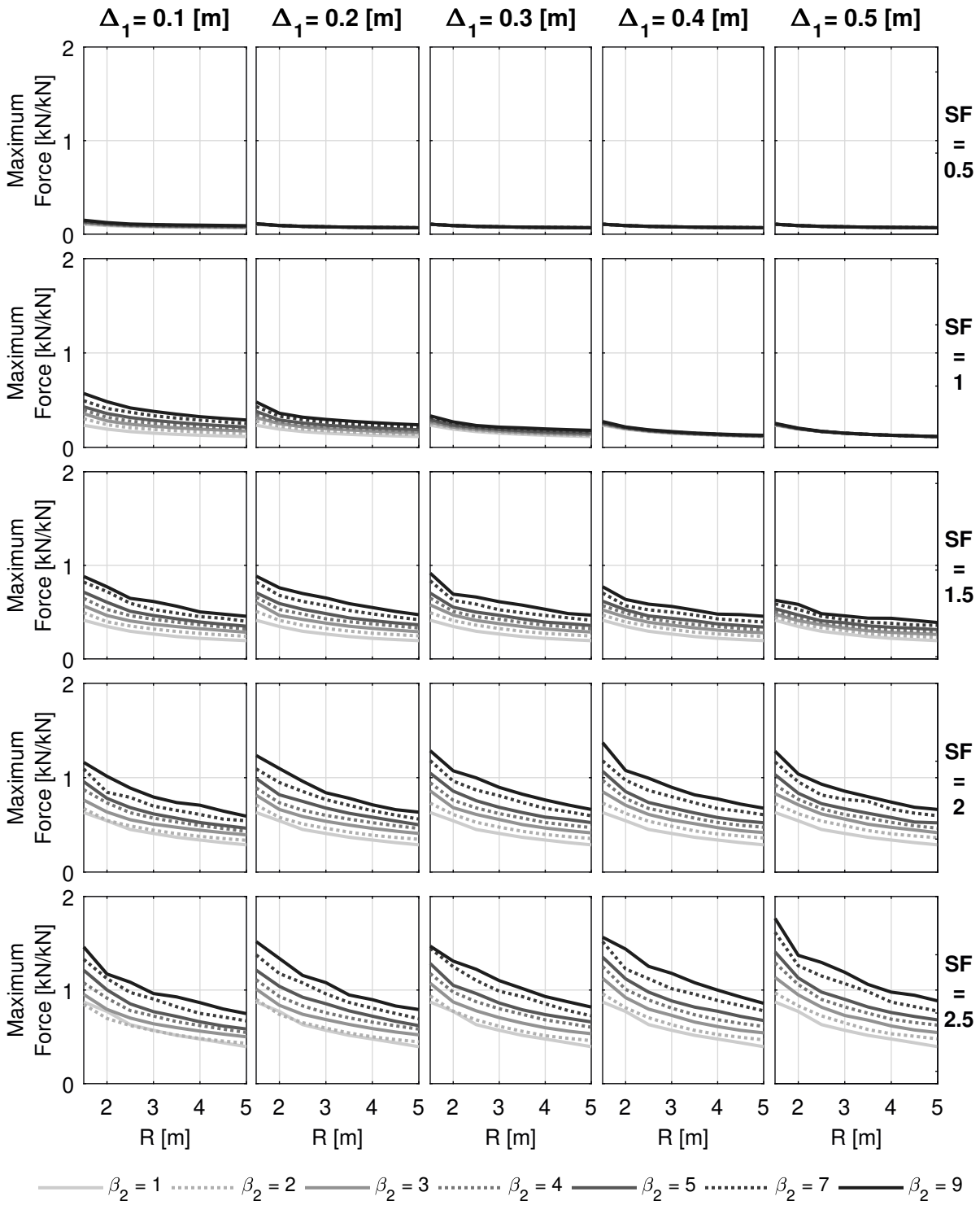

Figure 4.1: Maximum isolator force for $\mu_2 = 5\%$.

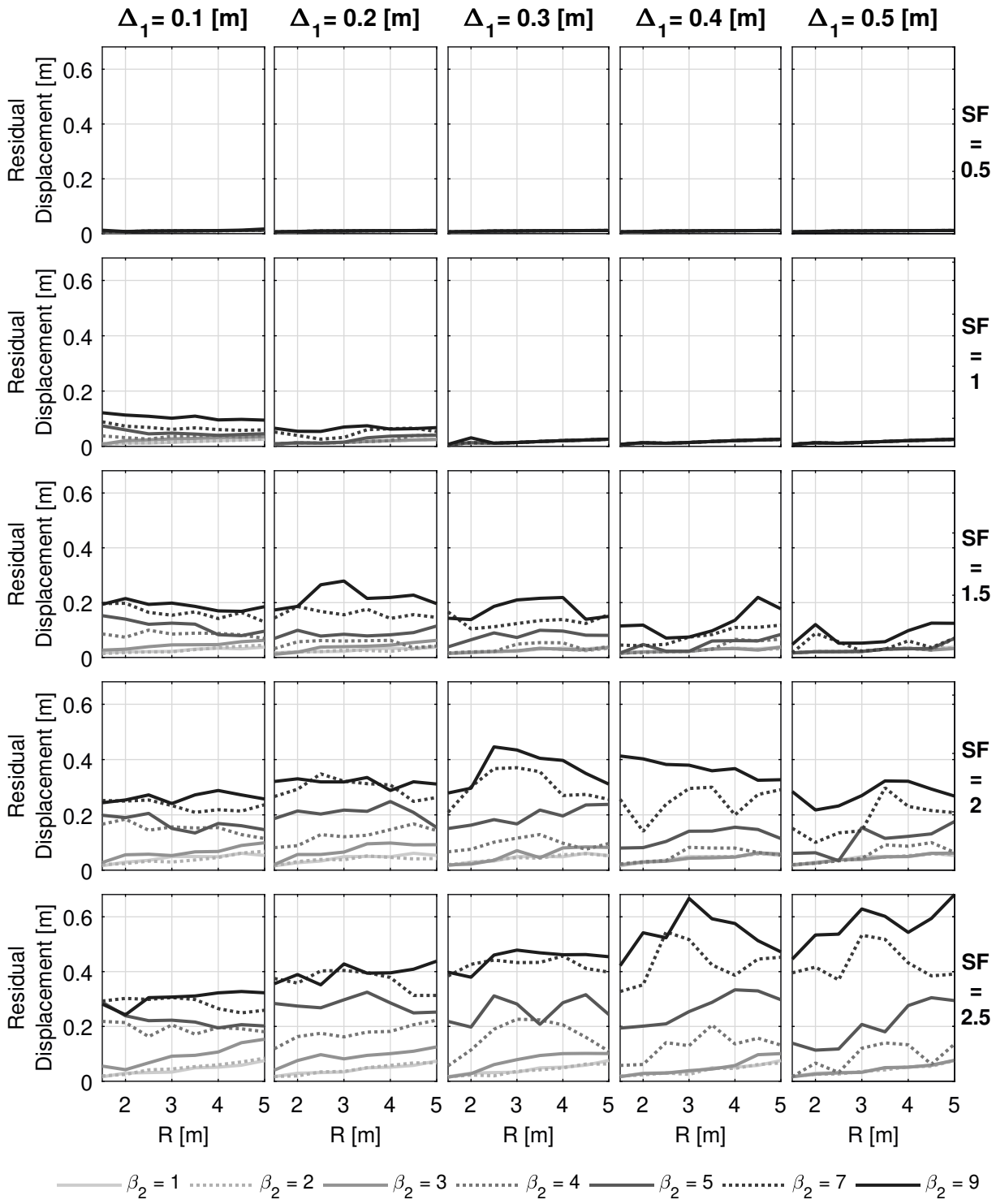

Figure 4.2: Maximum isolator residual displacement for $\mu_2 = 5\%$.

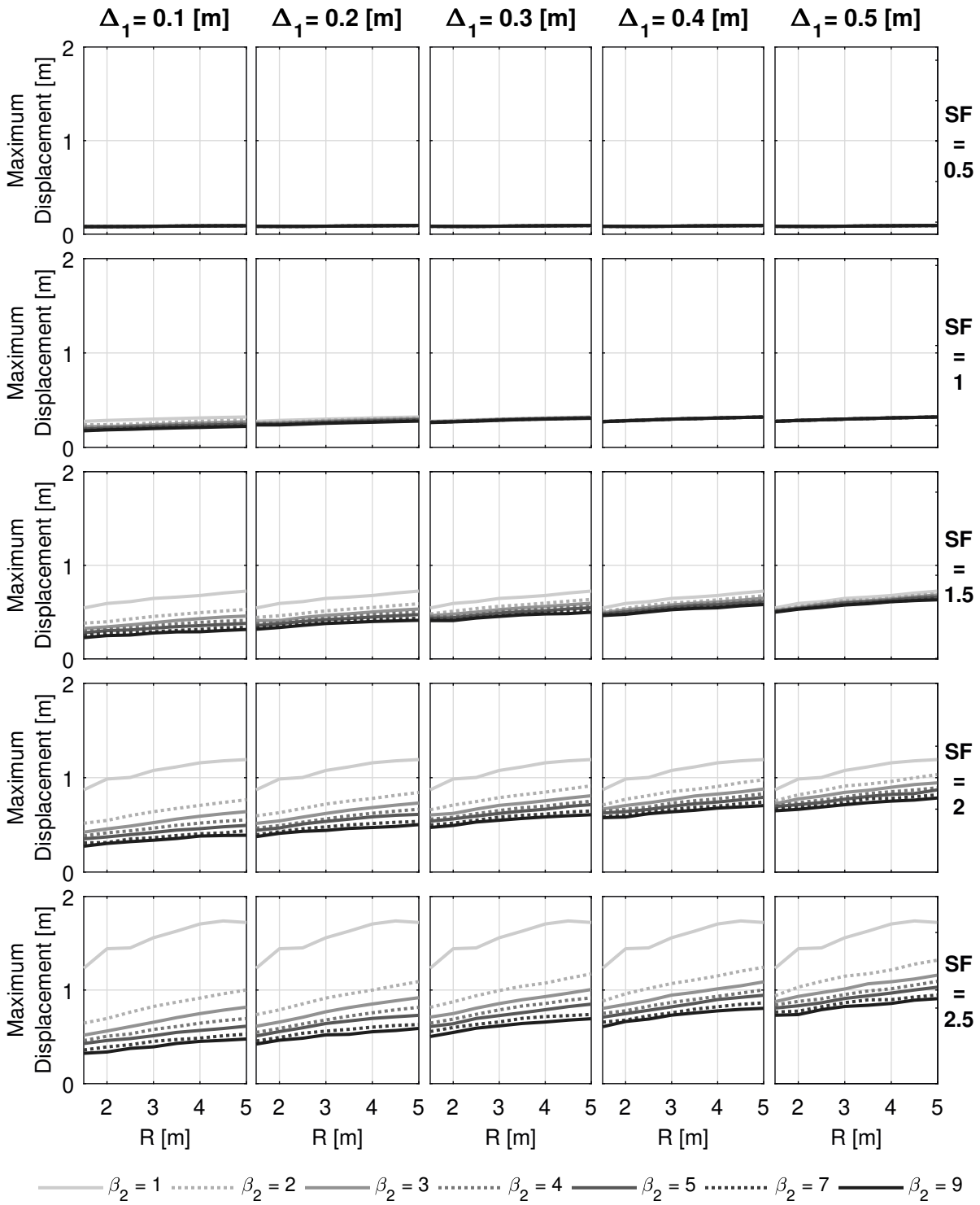

Figure 4.3: Maximum isolator displacement for $\mu_2 = 5\%$.

which aspects are most important and what restrictions they have. For example, if there is a displacement restriction, then a higher β_2 value will allow the device to be effective in a higher intensity earthquake while experiencing a smaller displacement. However, increasing β_2 decreases the device's re-centering capability.

The parametric study showed which parameters are most important to consider when designing. The radius of curvature proved to not make a large difference in the parameters of interest; however, it is important to keep the radius large enough to avoid unwanted vertical accelerations. The parameter Δ_1 is closely related to the ground motion scale factor, and may be chosen depending on the displacement restrictions of the designer; choosing Δ_1 will be discussed further in Chapter 7.1.1. Additionally, μ_1 did not greatly change the trends seen in Figures 4.1 through 4.3. Choosing β_2 has been shown to be the most important parameter in determining the behavior of an AVF device.

Given that β_2 especially influences the device's behavior, recommendations are offered for which to choose. A β_2 value of 2 is recommended for the overall best AVF bearing behavior. This β_2 value allows for adaptive behavior, which means that multiple intensity ground motion levels can be considered. For a similar maximum force, the AVF device has a much lower maximum displacement at large ground motion intensities, giving an AVF device an advantage when used for rare events. Lastly, the AVF device also has the same excellent re-centering properties as a Friction Pendulum. When α_1 is greater than 2, the device will never have a large residual displacement no matter how intense the ground motion due to the flat slope of the second re-centering stiffness. To emphasize this point, a scale factor of 10 was used in analysis for devices with $\beta_2 = 2$, 2.5 and 3. The residual displacement was recorded and is shown in Figure 4.4. One can see that all of the residual displacements for $\beta_2 > 2$ can be quite large; conversely, the residual displacements for $\beta_2 = 2$ are small despite the large ground motion.

An interesting phenomenon can be observed in Figure 4.4. This figure shows a gap in residual displacement around 0.2 and 0.5 m , which is due to a section of instability caused by the shape of the hysteresis loop, as demonstrated in Figure 4.5.

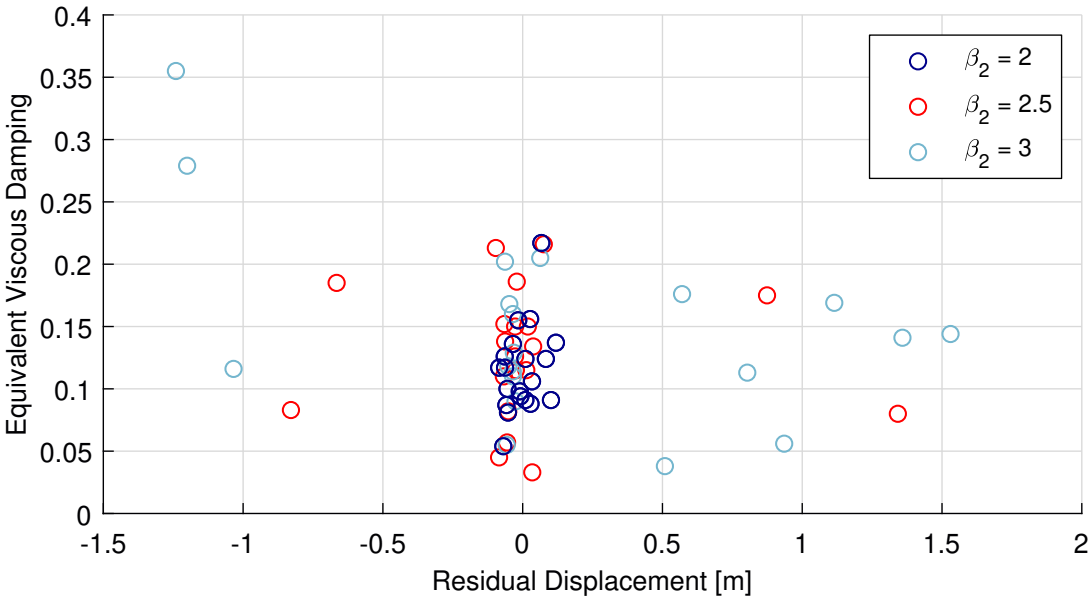

Figure 4.4: Equivalent viscous damping vs. residual displacement for various β_2 values

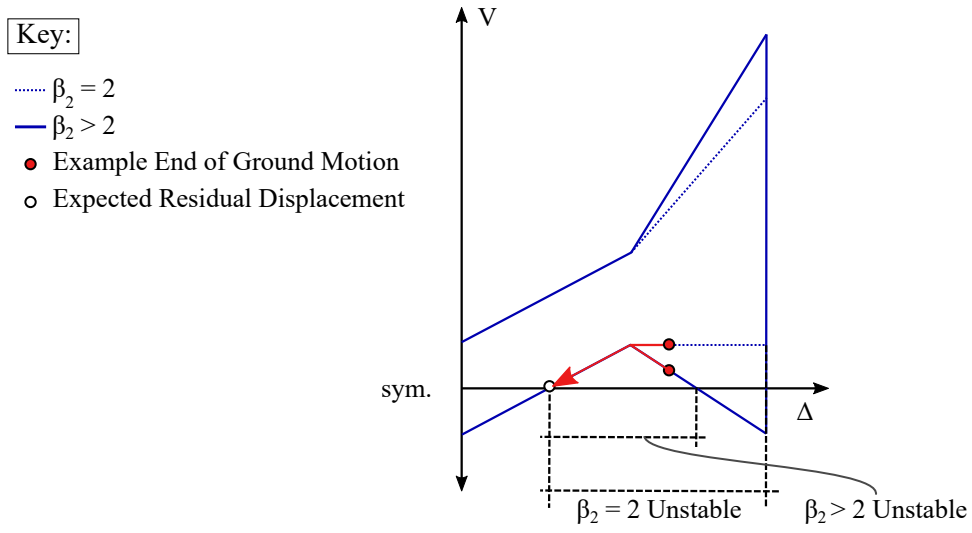

Figure 4.5: Example of unstable behavior in AVF bearing

4.5 Conclusions

The maximum displacement, force, and residual displacement of 840 Adaptive Variable Friction devices supporting a rigid single degree of freedom system were studied in this chapter. The results showed that β_2 had a large effect on the device behavior, and that R and μ_1 had less of an effect. Δ_1 and ground motion intensity were related, and therefore, Δ_1 should be chosen based on desired displacement and force demands for that intensity level. The study also showed it would be beneficial to use an AVF device with a low β_2 value when re-centering is important and maximum force are design constraints. Finally, it was suggested that a β_2 value of 2 be used for optimal AVF bearing behavior. This β_2 value has advantages over the Friction Pendulum in rare events due to it achieving a much lower maximum displacement for a similar residual displacement and maximum force.

Part II

DESIGN OF ADAPTIVE VARIABLE FRICTION BASE ISOLATED SYSTEMS

Chapter 5
DESIGN LITERATURE REVIEW

The design of base isolated structures is relatively new compared to other types of design. It has been codified to varying degrees in different international codes, making it easier for designers to use this technology. A review of current codes is presented in this chapter, serving as an introduction for what is currently available to base isolation designers.

The code, of course, serves as a design minimum, and performance goals of a structure often exceed these requirements. Recently, a design method called Direct Displacement-Based Design (DDBD) has been introduced [Priestley et al., 2007a]. This method has advantages over traditional force based design methods, as discussed in the chapter. The basics of DDBD system are discussed alongside existing design methods for single friction and variable friction pendulum devices. The DDBD and Friction Pendulum design methods presented will be used as a basis for AVF device design.

5.1 Overview of Base Isolation Design Methods

There are three prominent international codes that include base isolation system design, namely the Japanese, European, and American codes. A brief overview of codified design methods currently available is presented in this section alongside an introduction into DDBD.

5.1.1 Review of International Design Codes

Japanese Code

The Japanese design code is defined by the Building Standard Law and associated Enforcement Order [Pietra et al., 2015]. It allows for three different routes of design: 1) No structural calculations, 2) Equivalent Lateral Force Method (ELFM), and 3) NLTHA. Route 2 is used

in about 10% of isolated structures in Japan, and Route 3 accounts for the rest since Route 1 is not used in practice. The ELFM in Route 2 is similar to the method denoted in the American code (ASCE 7) in that it distributes forces based on both height and seismic weight [Marino et al., 2005]. The NLTHA for Route 3 is simplified; the story stiffness is obtained from a non-linear static pushover analysis and is assigned to a column connected to the equivalent seismic masses to create a simple MDOF column model. The isolator is modeled through both bi-linear shear and linear rocking springs [Higashino and Okamoto, 2015]. Though there are shear strain requirements and a maximum displacement the isolator must not exceed, there are no recommendations for how to design the isolator.

Two demand levels are considered in Japanese design: serviceability and life safety, corresponding to 50 and 500 year return periods, respectively. To obtain demands, it is common practice to consider six ground motions which are scaled between one and five seconds. The average spectrum must be no more than 2% off from a target spectrum with 5% damping. In order to account for damping provided by the isolators, the average spectrum is reduced by F_h, calculated as:

$$0.4 \leq \eta = \frac{1.5}{1 + 10(\xi_\nu + 0.8\xi_{eff,d})} \leq 1.0, \tag{5.1}$$

where ξ_ν and $\xi_{eff,d}$ are two codified damping coefficients representing pure viscous-type behavior (isolator only) and area-based equivalent damping (isolator and structure).

European Code

The three design methods allowed in EC8 include ELFM, response spectrum analysis (RSA), or NLTHA [EC8, 1998]. The ELFM in EC8 differs from the one in ASCE 7-10 in that it is proportional only to the story mass, not the height. A full 3D model must be used for both RSA and NLTHA. The isolator is represented using equivalent properties for stiffness and damping, and must not exceed the code-defined displacement maximum.

The only demand level considered in EC8 corresponds to a 500 year return period. To design for an average, a minimum of seven pairs of ground motions must be considered. They

are to be scaled between $0.2T_1$ and $2.0T_1$, where T_1 is the effective period of the base isolated system. For ground motion scaling, each ground motion spectra must be greater than 90% of the target value within this period range.

There are two ways presented in different versions of EC8 for reducing the spectral demand. The spectral reduction in the previous version of EC8 is defined as:

$$\eta = \sqrt{\frac{7}{2+\xi}} \tag{5.2}$$

where ξ is the equivalent damping of the system. For base isolated devices, [Priestley et al., 2007b] recommends using the older EC8 damping reduction expression (Equation (5.2)) due to it better predicting inelastic displacements in their studies. For this reason, [Calvi et al., 2016] recommended the use of Equation (5.2) for estimating demand in VF devices. It should be noted, however, that there are a number of valid methods that can be used to get the reduced demand on the system and that a designer should choose the most appropriate method.

American Code

Codified base isolation design in the U.S. has a brief history which began with the Structural Engineers Association of Northern California (SEAONC). They created a group in 1980 to begin developing guidelines for isolated buildings. After that, the Seismology Committee of the Structural Engineers Association of California published the Recommended Lateral Design Requirements and Commentary, commonly known as the Blue Book [SEAOC, 1985]. This book served as the basis for the Unified Building Code (UBC) [ICBO, 1991], which is what current ASCE seismic design code is based on. The SEAONC code focused more on static analysis, resulting commonly in regular structures with braced frames. The UBC code had more of an emphasis on dynamic analyses, making them required in more situations [Kelly, 1994].

The current American code, ASCE 7-16, is similar to EC8 in that the system can be

designed using ELFM, RSA, and NLTHA. However, the ELFM in ASCE is dependent on both height and seismic weight and includes force distribution factors that take into account higher mode effects on base isolated devices [Ryan et al., 2019]. The isolator is modeled using the secant stiffness, which must be obtained from bearing prototype testing. ASCE does not have specifics on actual bearing design; however, design guidelines for common devices (such as the lead rubber bearing and the friction pendulum) that use ASCE force-based design approaches are outlined in [Naeim and Kelly, 1999].

The demand levels considered in ASCE correspond to a 475 year and 2475 year return period, which correspond to the demand levels chosen for this study. The resultant of seven pairs of ground motions must be scaled so that the average is not less than the design spectrum over a period range of $0.2T_1$ to $1.25T_1$, where T_1 is the effective period of the base isolated system. The spectrum is reduced based on a table of reduction factors, which can be interpolated depending on the effective damping ratio.

5.1.2 Direct Displacement Based Design vs. Force Based Design

As can be seen in the code overview, the most prevalent type of codified design is force-based. This historically has been used because the relationship between loads and forces has been well understood. However, there are many fundamental problems with this type of design. For example, force-based design depends heavily on the ductility of a system, yet there is little consensus on how to estimate this. As an example, a steel moment-resisting frame has a force reduction factor of 8 in the U.S., 2-4 in Japan, and 6.3 in Europe [Priestley et al., 2007a]. Another problem lies in the dependency of stiffness and strength which is not addressed in force-based design. The force experienced by a member will continue to change until the member stiffness is final, yet the new force distribution is rarely calculated. Additional problems with force-based design can be found in [Priestley et al., 2007a].

Since damage is often correlated with displacement (i.e. story drift), not a particular force, it makes sense to design based on the controlling damage state. Additionally, recent studies have shown DDBD to be effective at predicting system responses for both fixed-base

[Priestley et al., 2007b] and isolated structures [Timsina and Calvi, 2018; Cardone et al., 2009]. For these reasons, DDBD was chosen as the basis for AVF system design.

5.2 Direct Displacement Based Design for Base Isolated Structures

5.2.1 Overall System Design

The basic procedure for DDBD is summarized in Figure 5.1. The first step in DDBD is to idealize the structure into an equivalent SDOF system, which takes into account both the isolator and structure, as shown in Figure 5.1(a). The displaced shape of the structure can be estimated based off of the yield displacement and the type of type of structure being modeled (e.g. shear type or frame type); suggested equations can be found in [Priestley et al., 2007a]. Note that the displacement of the structure at each floor should include the displacement from the isolator. Once the displacement profile of the structure is calculated, the design displacement of the equivalent SDOF system can be found:

$$\Delta_{e,sys} = \frac{\sum_{i=1}^{n}(m_i\Delta_i^2)}{\sum_{i=1}^{n}(m_i\Delta_i)}, \tag{5.3}$$

where m_i and Δ_i are the mass and displacement at each level i, respectively. The displacement of the effective structure can be calculated by subtracting the isolator displacement from the system displacement:

$$\Delta_{e,str} = \Delta_{e,sys} - \Delta_{iso}. \tag{5.4}$$

The effective height, corresponding to the first mode effective height, can be calculated as:

$$H_e = \frac{\sum_{i=1}^{n}(m_i \Delta_i H_i)}{\sum_{i=1}^{n}(m_i \Delta_i)}. \tag{5.5}$$

The effective mass of the SDOF system can be found similarly to H_e:

$$m_e = \frac{\sum_{i=1}^{n}(m_i \Delta_i)}{\Delta_{e,sys}}. \tag{5.6}$$

The second step, shown in part (b) of Figure 5.1, is to calculate the damping of the system, which can be found by combining the damping of the structure and the isolator:

$$\xi_{sys} = \frac{\xi_{str}\Delta_{e,str} + \xi_{iso}\Delta_{iso}}{\Delta_{e,sys}}. \tag{5.7}$$

With the damping known, the spectrum can be reduced to find the demand (Figure 5.1(c)). Using the displacement demand of the system, $\Delta_{e,sys}$, the reduced displacement spectrum is entered and the effective period of the system $T_{e,sys}$ is read. Using the effective period, the effective secant stiffness of the system, $K_{e,sys}$, can be found as:

$$K_{e,sys} = \frac{4\pi^2 m_e}{T_{e,sys}^2}. \tag{5.8}$$

The base shear at the selected design demand can be calculated using the effective stiffness (Figure 5.1(d)):

$$V_{sys} = K_{e,sys}\Delta_{e,sys}. \tag{5.9}$$

Finally, the base shear can be distributed according to:

$$F_i = V_{sys} \frac{\Delta_i m_i}{\sum_{i=1}^{n} m_i \Delta_i}. \tag{5.10}$$

This force distribution can be modified depending on a designer's needs. For example, in order to account for higher modes, the New Zealand code recommends adding a force equal to 10% of the base shear to the top of the structure [Priestley et al., 2007a].

5.2.2 Variable Friction System Design

The DDBD method presented gives the designer a way to design the overall system, but does not detail specific isolator design. Relevant friction bearings such as the FP, BowTie, and BowC bearings have suggested design methods outlined in literature and are discussed in this section.

The BowTie and BowC are variable friction devices characterized by β_1 (post-activation re-centering stiffness/post-activation stiffness) and have been extensively studied by [Timsina, 2017]. The BowTie device is flat, which corresponds to a β_1 value of -1; the BowC is defined by a radius of curvature, which corresponds to a β_1 value of 0. Both devices have many concentric rings with different frictional properties, whereas a friction pendulum only has one ring and coefficient of friction and an AVF device has two. The force-displacement curve describing these devices can be seen in Chapter 2.3.2. To design, either the ring diameters or the coefficients are chosen; the other is solved for. These parameters are chosen in a way that a linear post-activation stiffness can be assumed. More details about the design process can be found in [Calvi and Ruggiero, 2016]. Note, this process can be adapted for friction pendulum design by having $\beta_1 = 1$ and a constant μ, and will be discussed in detail in Chapter 7.1.1.

The design of the Adaptive Variable Friction device varies from previously explored VFS in that the amount of rings and friction coefficients are limited to 2. Additionally, there are

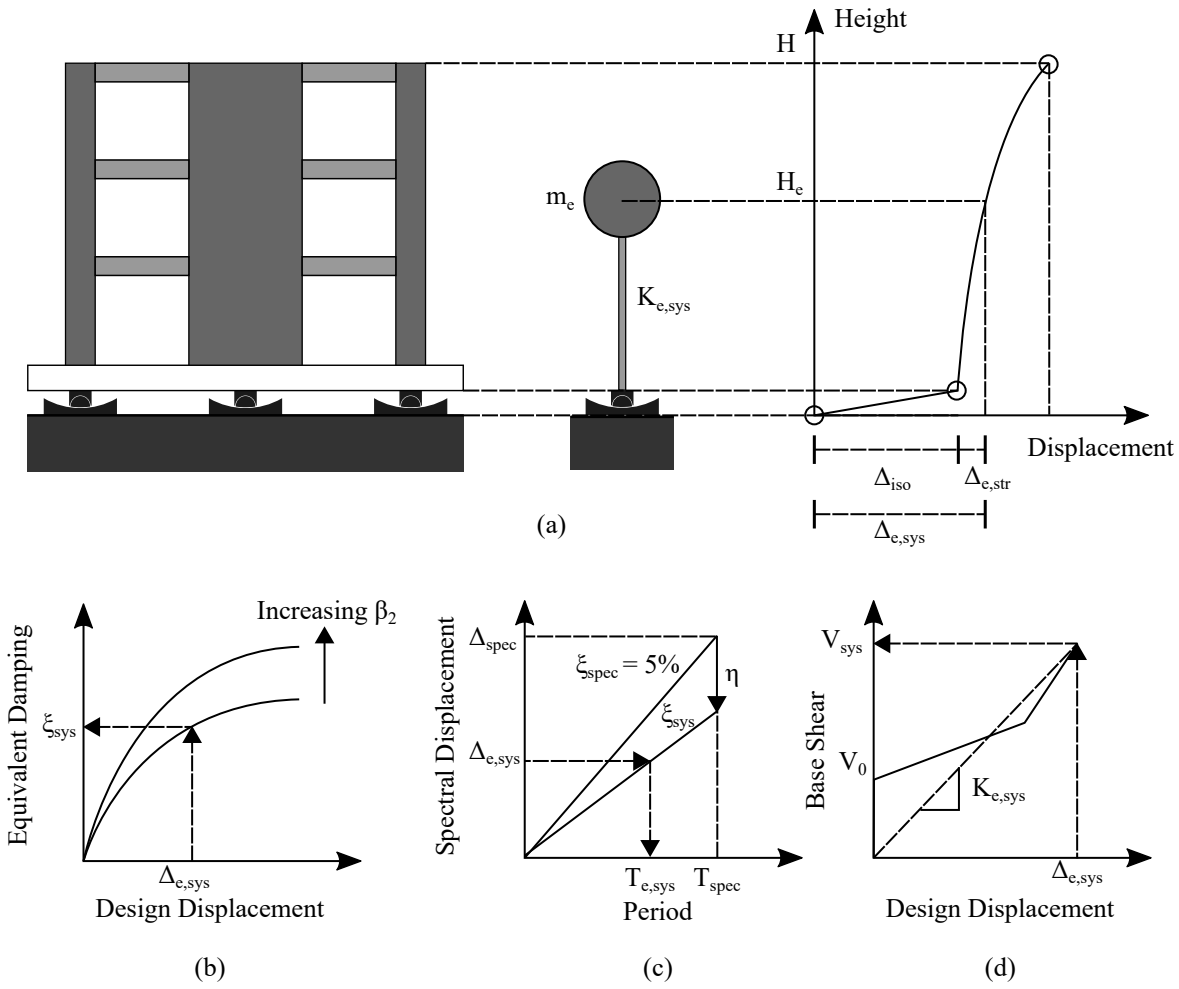

Figure 5.1: Concepts of DDBD for isolated structures adapted from [Calvi and Ruggiero, 2016]. (a) Equivalent SDOF system and displaced shape; (b) calculation of equivalent viscous damping; (c) calculation of system period; (d) calculation of design shear force

two distinct stiffness values, not one. The design method for the AVF device will build off of the variable friction and DDBD methods presented, and will be discussed in the following chapters.

Estimating Isolator Damping

In order to design a device, it is useful to estimate the damping property of the isolator. One of the most common estimations of damping is the a classic Jacobsen approach, which is based on the idea that the energy dissipated by the structure over one vibration cycle can be equated to that of an equivalent viscous system [Jacobsen, 1960]. This definition of damping has been used to model damping for other base isolation systems, including variable friction. It has been shown that the damping of a variable friction system can be expressed as:

$$\xi_{hys} = \frac{E_d}{4\pi E_{so}} = \frac{A_{hys}}{2\pi V_{max}\Delta_{max}}, \tag{5.11}$$

where A_{hys} is the area under the force-displacement curve, V_{max} is the maximum isolator shear force, and Δ_{max} is the corresponding maximum isolator displacement, pictured in Figure 5.2 [Calvi et al., 2016]. For the BowTie and BowC variable friction systems, Equation (5.11) was used to derive each device's respective equivalent viscous damping (EVD) based on the hysteretic area. The damping properties of those devices were validated through an extensive numerical study [Timsina, 2017]. Due to the success of using the Jacobsen model for variable friction systems, this method was used to express the damping of the Adaptive VFS.

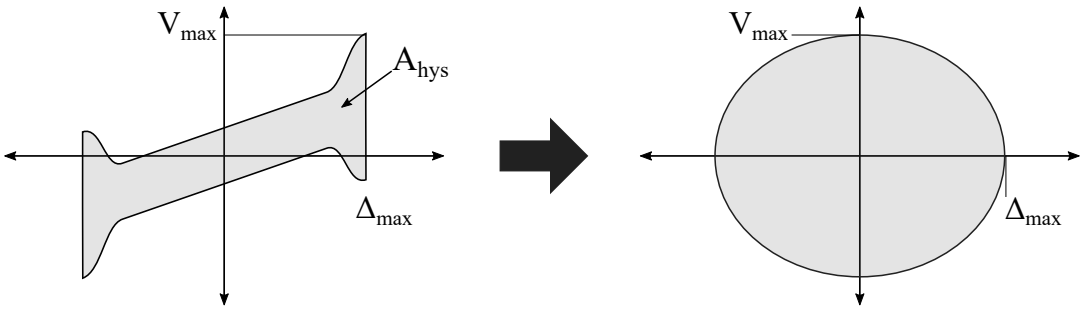

Figure 5.2: Application of Jacobsen method to AVF bearing equivalent viscous damping

Chapter 6

DERIVATION AND VERIFICATION OF AVF DEVICE DAMPING PROPERTIES

6.1 Overview

This chapter explores the energy dissipation properties of the AVF bearing. Having a closed-form expression for damping is a tremendous tool, especially for designers. A linear expression helps to keep design simple, allowing for maximum demands to be estimated without the need for NLTHA. This chapter goes through the derivation of the equivalent viscous damping of an Adaptive VFS and then validates the expression by comparing the results against over 600,000 NLTHA. Once validated, the expression can be used in the design procedure for SDOF and MDOF systems.

6.2 Theoretical Formulation of Equivalent Viscous Damping

Referencing Equation (5.11), both the adaptive device's area under the force-displacement curve along with the maximum force and displacement must be expressed in order to develop an equation for EVD. Three of the parameters defined in Chapter 3 (α_1, α_2, and γ) were used to define the area enclosed by the hysteresis loop as well as the maximum force and displacement. The derivation is based on the assumption that the hysteretic response of the system is symmetric, which has been shown to be valid if the system is self-centering [Timsina, 2017].

The overall area enclosed can be divided into three unique segments: A_1, A_2, and A_3 as seen in Figure 6.1.

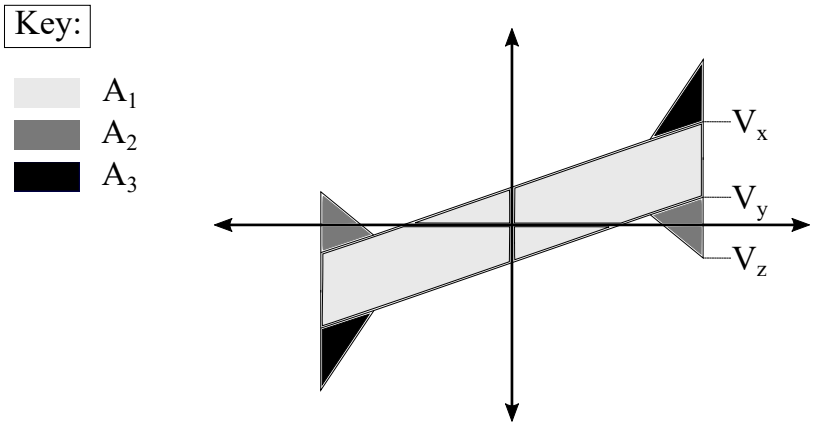

Figure 6.1: Area subdivisions

The area under the curve can be written as:

$$A_{hys} = A_1 + 2A_2 + 2A_3, \tag{6.1}$$

where:

$$A_1 = 4\Delta_2 V_0, \tag{6.2}$$

$$A_2 = (\Delta_2 - \Delta_1)(V_2 - V_x), \tag{6.3}$$

$$A_3 = (\Delta_2 - \Delta_1)(V_y - V_z). \tag{6.4}$$

The intermediate forces V_x, V_y, and V_z, can be written as:

$$V_x = V_0 + K_1\Delta_2, \tag{6.5}$$

$$V_y = -V_0 + \beta_1 K_1 \Delta_2, \tag{6.6}$$

$$V_z = -V_0 + \beta_1 K_1 \Delta_1 + (2 - \beta_2)(\Delta_2 - \Delta_1). \tag{6.7}$$

The area segments and intermediate forces can be combined to give:

$$A_{hys} = 4\Delta_2 V_0 + 2(\Delta_2 - \Delta_1)^2 \left[\frac{V_2 - V_1}{\Delta_2 - \Delta_1} - \frac{\Delta_1 - \Delta_0}{\Delta_1} \right]. \tag{6.8}$$

With simplification and applying the parameters α_1, α_2, γ, the area can be re-written as:

$$A_{hys} = 2\Delta_1 V_0 \left[2\gamma + (\gamma - 1)(\alpha_2 - \alpha_1) - (\alpha_1 - 1)(\gamma - 1)^2 \right]. \tag{6.9}$$

The denominator of Equation (5.11) can be defined as:

$$\xi_{Adaptive_{denom}} = 2\pi \Delta_1 V_0 \alpha_2 \gamma. \tag{6.10}$$

Finally, Equations (6.9) and can be combined with Equation (6.10) to create the adaptive EVD equation:

$$\xi_{Adaptive} = \frac{2\gamma + (\alpha_2 - \alpha_1)(\gamma - 1) - (\alpha_1 - 1)(\gamma - 1)^2}{\pi \alpha_2 \gamma}. \tag{6.11}$$

6.3 Damping Verification Procedure

This section discusses a numerical method for the calculation of EVD, against which the theoretical equation can be compared. In order to verify the EVD equation for Adaptive VF systems, the ten pairs of San Francisco (non-pulse) ground motions detailed in Chapter 3.2.3 were used in the nonlinear analyses. Note, the ground motion scaling used in the EVD study was slightly different from the ones denoted in Chapter 3. Since this chapter is focused on behavior and not matching analysis to design values, the scaling of the ground motions should have no effect the trends presented.

Several AVF devices with varying R, Δ_1, μ_1, and β_2 were considered. The intensity of

the ground motion was varied using a scale factor applied in addition to the scale factor needed to match the ground motion spectrum to the MCE design spectrum. Overall, the EVD validation included the study of over 675 devices for 46 scale factors and 20 ground motions, which resulted in over 600,000 NLTH analyses. A summary of the devices studied are included in Table 6.1.

Table 6.1: Isolator parameters considered in EVD validation (Low:Step:High)

R [m]	β_2	Δ_1 [m]	μ_1 [%]	Scale Factor
2:1:6	1:0.5:5	0.1:0.1:0.5	3, 5, 8	0.5:0.1:5

6.3.1 Numerical Modeling

The assumptions and numerical modeling expressions used in this chapter are explained in detail in Chapter 3, and the method for estimating damping in the NLTHA is described in Chapter 4.3. For this study, only rigid structures were studied based on the conclusion of previous research on VF systems [Timsina and Calvi, 2018]. The study conducted by [Timsina and Calvi, 2018] included three structures with different stiffness and a damping ratio of 2%. The EVD trend showed little variation when taking into account the varying structure stiffness; therefore, only rigid SDOF structures will be considered in the EVD validation for Adaptive Variable Friction Systems.

6.4 Damping Verification Results

6.4.1 Algebraic Verification

When $\beta_2 = 1$, the AVF device hysteresis is the same as a Friction Pendulum system since $\beta_2 = 1$ implies no change in the coefficient of friction when moving from the first to the second ring. This also implies that α_2 for an AVF device is the same as α for an FP. Equation (6.12)

shows the the Friction Pendulum EVD expression, which is derived in [Timsina and Calvi, 2018]:

$$\xi_{FP} = \frac{2}{\pi\alpha} \tag{6.12}$$

An AVF bearing with $\beta_2 = 1$ can be shown equal to a FP algebraically using each device's EVD equations and valid combinations of α_2 and γ. For example, if $\gamma = 1$, then α_1 must equal α_2 since there is no difference in the two levels of design displacement. Plugging these values into Equation (6.11) simplifies down to the EVD equation for a Friction Pendulum system.

6.4.2 NLTHA Damping Results

Exploration of Parameter Sensitivity

Since the adaptive system is defined by many parameters, it is important to justify which parameters to isolate when plotting the NLTHA data. Therefore, Δ_1, μ_1, R, and β_2 were plotted separately to observe how they affect the damping trends from the nonlinear analyses. These plots only include data from devices that have a maximum displacement larger than Δ_1, i.e. they have reached the second post-elastic stiffness. All parameters are plotted against the ratio between the maximum force and the activation force, or α_2.

Figure 6.2 shows the averaged results of the NLTHA grouped by μ_1 and R. The full data set can be found in Appendix A. The average for each parameter was calculated by sectioning the data into bins as a function of α_2 and calculating the mean. There is little variation in the average EVD for μ_1 and R, and neither are defined in the adaptive EVD equation, so it is expected that these parameters would not greatly affect the damping behavior of the device. To quantify the spread of this grouped data for comparison, the coefficient of variation (COV) was calculated for many values of α_2 and can also be seen in Figure 6.2. There is a slight increase in the COV for increasing μ_1 and decreasing R, but the COV for both parameters largely follow the same increasing (nominally) linear trend for increasing α_2.

This data further emphasizes the conclusion that the damping trends are largely unaffected by changes in μ_1 and R, so they will be plotted together in all plots moving forward.

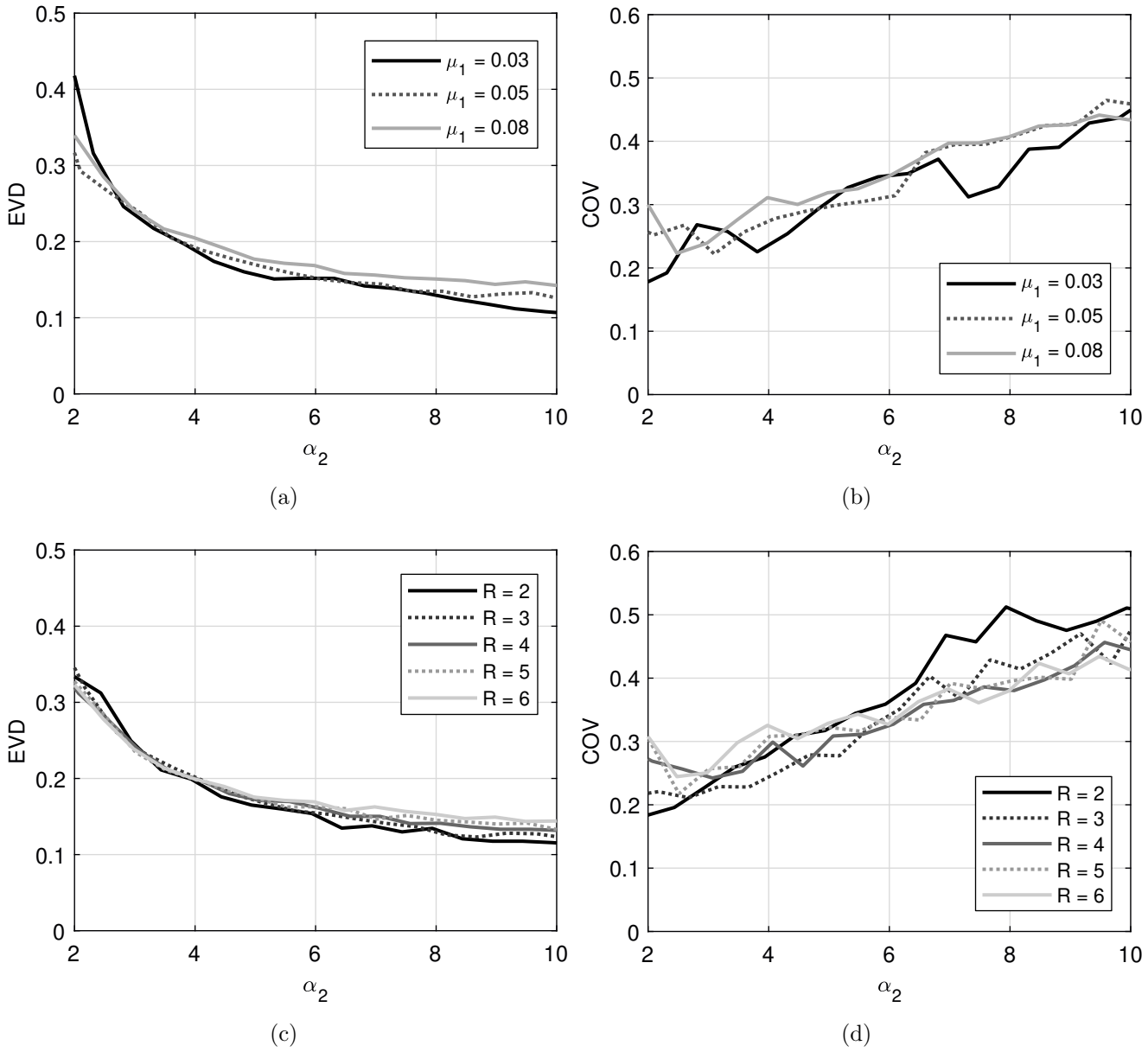

Figure 6.2: Mean and Coefficient of Variation of the EVD from NLTHA grouped by (a),(b) μ_1 and (c),(d) R

Table 6.2: Variation data for EVD vs. α_2 grouped by Δ_1

Δ_1	0.1	0.2	0.3	0.4	0.5
Mean	0.22	0.19	0.17	0.16	0.15
Std. Dev.	0.08	0.07	0.06	0.06	0.06
COV	0.35	0.36	0.37	0.37	0.36

NLTHA Results Grouped by Δ_1

A summary of the averages from the NLTHA and the COV grouped by Δ_1 can be seen in Figure 6.3. Parts (a) and (b) of this figure show a clear trend in decreasing EVD as Δ_1 increases, which agrees with the theoretical prediction. As the area under the hysteresis curve increases, the ratio between the hysteresis and the equivalent ellipse decreases, which decreases the equivalent viscous damping. Additionally, it is expected that Δ_1 would change the EVD trend because it is indirectly a factor in the derived equation for ξ through the γ term.

The COV for Δ_1, shown in Figure 6.3(c), is very similar to that of μ_1 and R in that it linearly increases for increasing α_2 and is insensitive to Δ_1. To further describe the data, the average of the mean, standard deviation, and COV for each Δ_1 with α_2 <10 was taken and is shown in Table 6.2. The overall mean and standard deviation decreases for increasing Δ_1's, and the COV is largely the same between the variables, which was the case for both μ_1 and R. This signifies that even though the average EVD decreases for increasing Δ_1, the spread of the data remains similar within different Δ_1's.

Figure 6.3(c) shows the COV for $\Delta_1 = 0.5$ m starting past $\alpha_2 = 2$. Given the studied parameter set, the minimum α_2 for $\Delta_1 = 0.5$ m is larger than 2, which is why the COV line for that Δ_1 starts at a higher α_2 compared to the others.

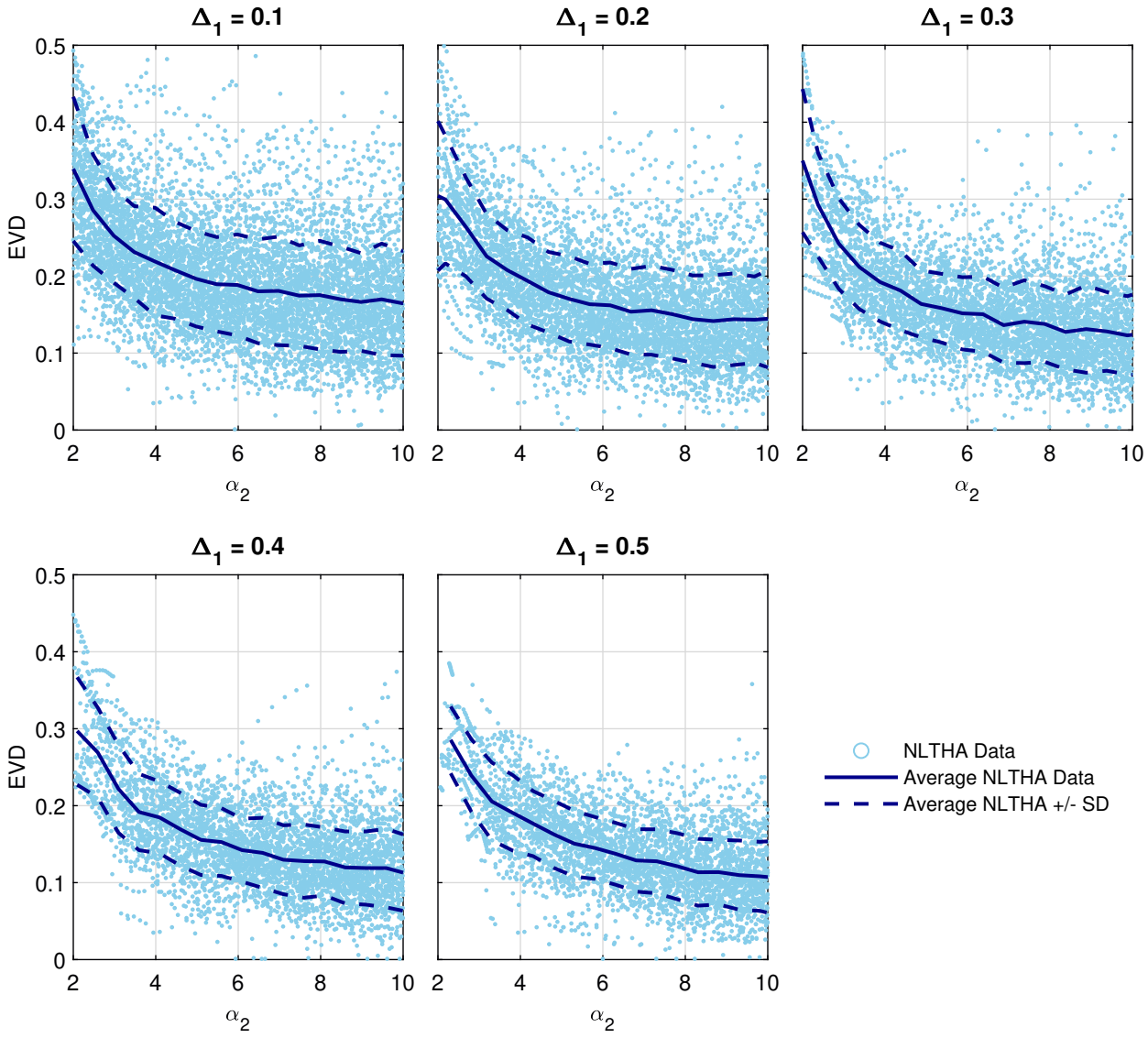

(a)

Figure 6.3: (a) EVD from NLTHA grouped by Δ_1, (b) EVD from NLTHA averages, (c) COV from NLTHA

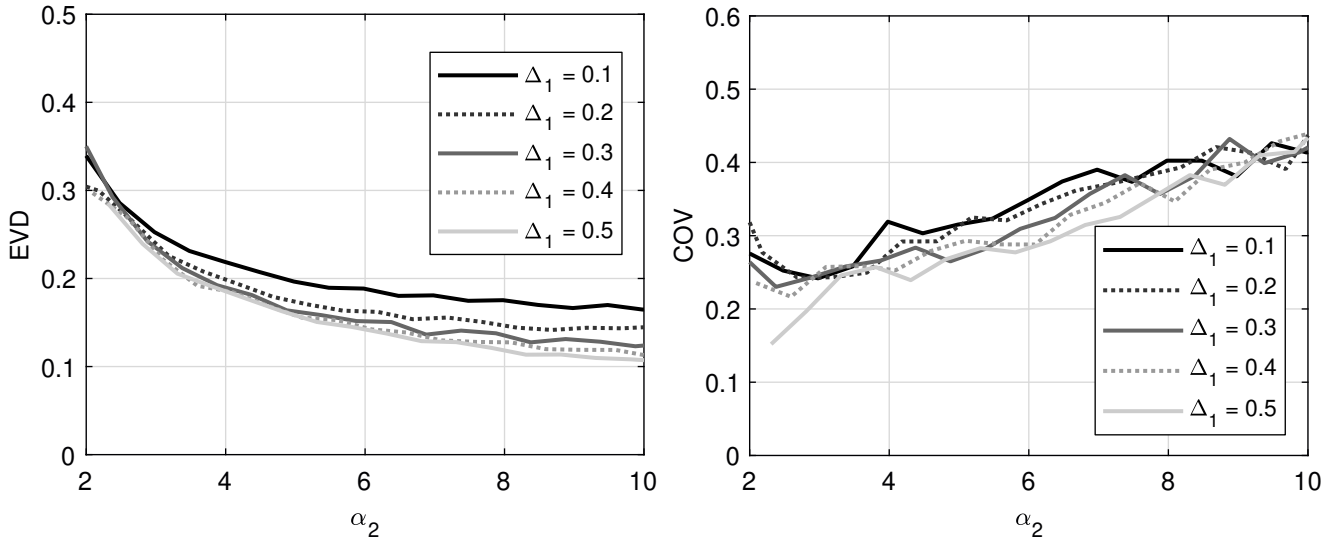

(b) (c)

Figure 6.3: (a) EVD from NLTHA grouped by Δ_1, (b) EVD from NLTHA averages, (c) COV from NLTHA

NLTHA Results Grouped by β_2

The results of the NLTHA grouped by β_2 can be seen in Figure 6.4. From the summary of averages, it is clear that the damping average does not change for β_2 >2. This is further shown in Table 6.3, which shows that the average EVD for each β_2 remains at a constant average of about 20% after $\beta_2 = 2$. When $\beta_2 = 1$, the damping diverges from the other β_2 values around $\alpha_2 = 4$ and continues to diverge for larger α_2's. The change in behavior of $\beta_2 = 1$ makes sense since it is not actually an adaptive device, just a FP defined using adaptive notation as discussed previously. Even though the damping mean does not vary greatly between β_2, the COV changes more than for any of the other parameters. The data spread when $\beta_2 = 1$ does not depend on α_2 since a Friction Pendulum is not a function of α_2. The spread in EVD increases with increasing α_2 and β_2. From these NLTHA results, it can be concluded that Δ_1 helps to determine the trend of the average EVD, where β_2 helps to determine the spread of the data.

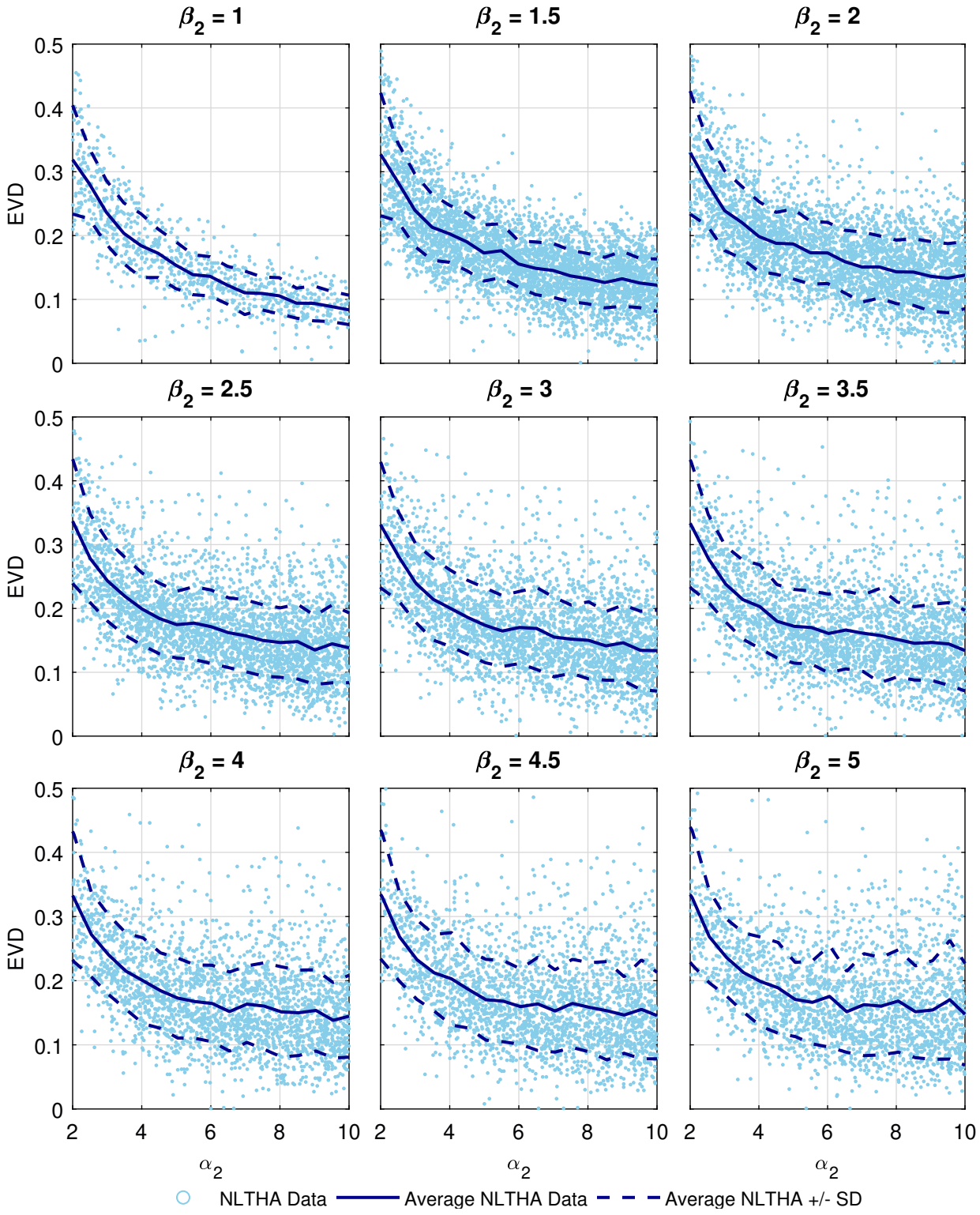

(a)

Figure 6.4: (a) EVD from NLTHA grouped by β_2, (b) EVD from NLTHA averages, (c) COV from NLTHA

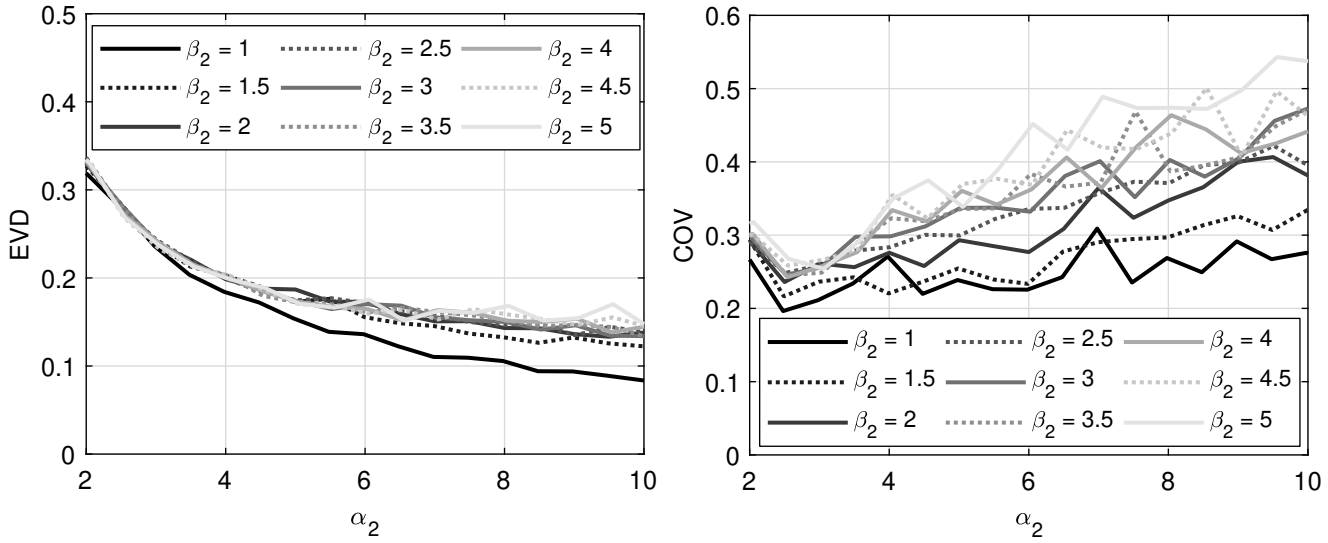

(b) (c)

Figure 6.4: (a) EVD from NLTHA grouped by β_2, (b) EVD from NLTHA averages, (c) COV from NLTHA

Table 6.3: Variation data for EVD vs α_2 grouped by β_2

β_2	1	1.5	2	2.5	3	3.5	4	4.5	5
Mean	0.17	0.19	0.20	0.20	0.20	0.20	0.20	0.20	0.20
Std. Dev.	0.04	0.05	0.06	0.06	0.06	0.07	0.07	0.07	0.07
COV	0.24	0.28	0.31	0.34	0.35	0.36	0.37	0.38	0.39

6.4.3 Comparison with Derived EVD Equation

Overall Comparison

The results from the NLTHA were compared to the derived EVD equation for an Adaptive VFS. For each nonlinear analysis, the maximum forces and displacements were used to calculate a counterpart damping value using the derived equation. Figure 6.5 shows the results from all the NLTHA and corresponding equation EVD values. The averages match very well up to $\alpha_2 = 4$, and then the equation average slightly diverges to become a non-conservative estimate of damping.

The average agreement does not tell how close each respective NLTHA damping is to its paired equation value. Therefore, the error between the NLTHA value and the equation value was calculated for every data point. Note, the error is calculated as:

$$\xi_{error} = \frac{|\xi_{equation} - \xi_{NLTHA}|}{\xi_{equation}}. \tag{6.13}$$

The error data was again split into bins and the average of each bin was taken, which can be seen in Figure 6.5(b). The average error between the results mostly increases linearly with increasing α_2, following a similar trend to the COV for μ_1, R, and Δ_1. The standard deviation also increases with increasing α_2.

Comparison Grouped by Δ_1

When the equation results are grouped by Δ_1, the trends of the EVD equation and NLTHA averages agree with the trends seen in Figure 6.5, namely that the averages match and then diverge at an α_2 value less than 6. As Δ_1 increases, the α_2 range where the analysis and equation values match also increases. Separating out Δ_1 shows how the EVD equation follows the trend of the NLTHA data, in that the equation decreases with each increase in Δ_1. When the error is grouped by Δ_1, there is little difference within the EVD parameter as can be seen in Figure 6.6.

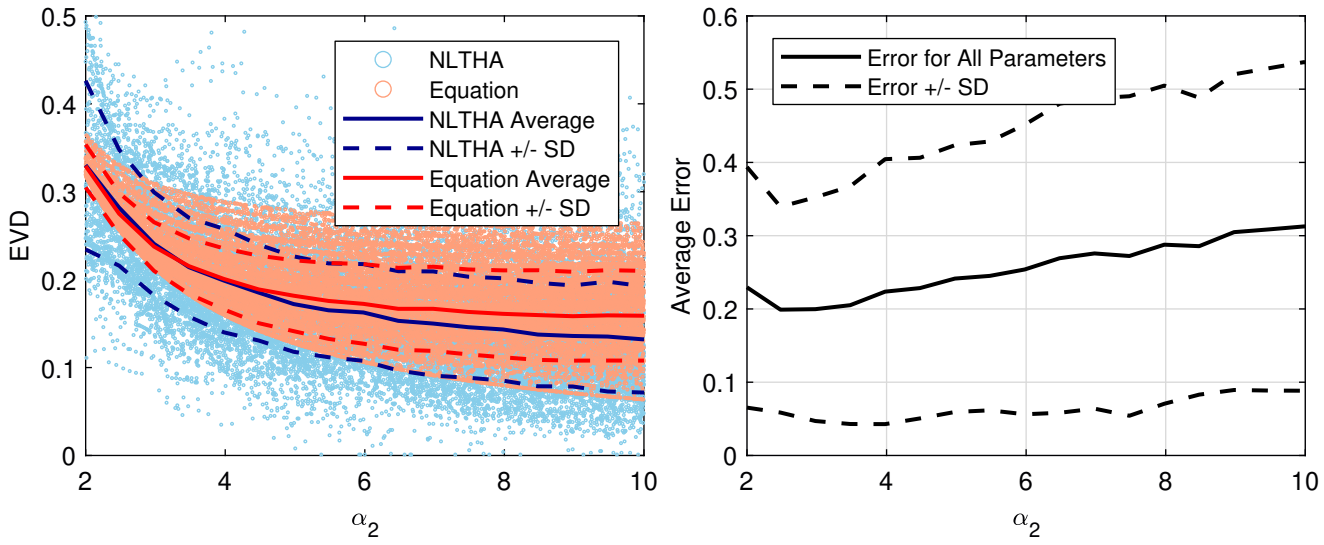

(a) (b)

Figure 6.5: (a) All NLTHA and equation damping values and (b) error between each damping pair

Comparison Grouped by β_2

When separating the data by β_2, the difference between the Friction Pendulum and Adaptive VFS can be seen in Figure 6.7(a). When $\beta_2 = 1$, the equation condenses to a single line, which is the same behavior as the damping for a FP. As β_2 increases, the equation prediction spreads similarly to the data, illustrating that the equation adapts depending on β_2. The average of the equation and NLTHA best matches for $\beta_2 = 1.5$, and then deviates for larger values. This is confirmed when looking at COV, shown in part (b) of Figure 6.7. This shows the error for $\beta_2 = 1.5$ is lowest, staying, on average, around 20% for α_2 values less than 10. The error increases until $\beta_2 = 3$, where afterwards it remains relatively the same for larger β's. These results suggest that the EVD equation best describes the damping of devices with β_2's ranging from 1.5 to 3. Surprisingly, the error is on average largest for the FP, where $\beta_2 = 1$. An explanation for this phenomena is that the AVF isolator damping equation cannot spread to fit the data better as it does for systems with higher β_2 values. The adaptive EVD

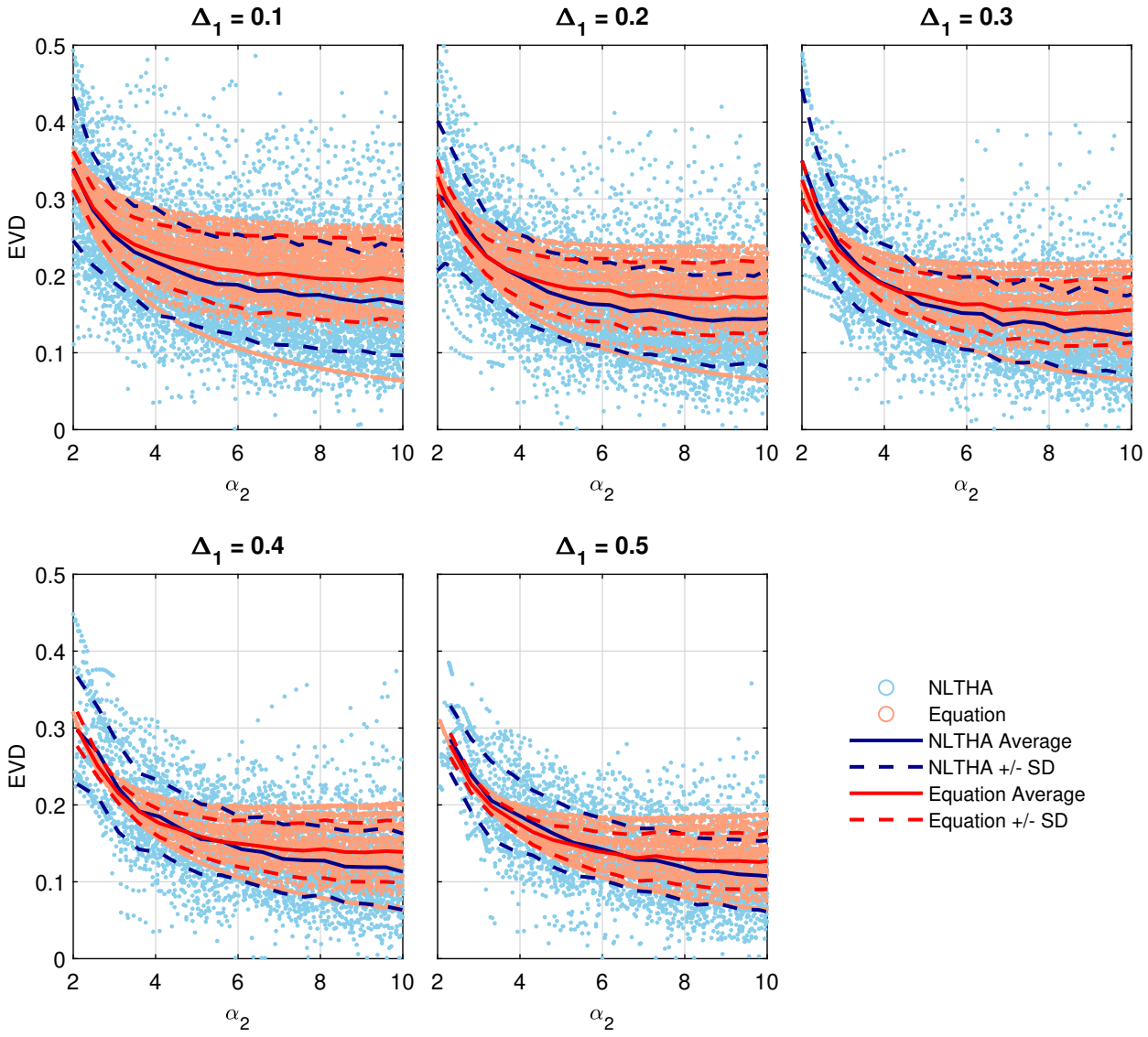

(a)

Figure 6.6: (a) All NLTHA and Equation Damping Values grouped by Δ_1 and (b) Error between each damping pair

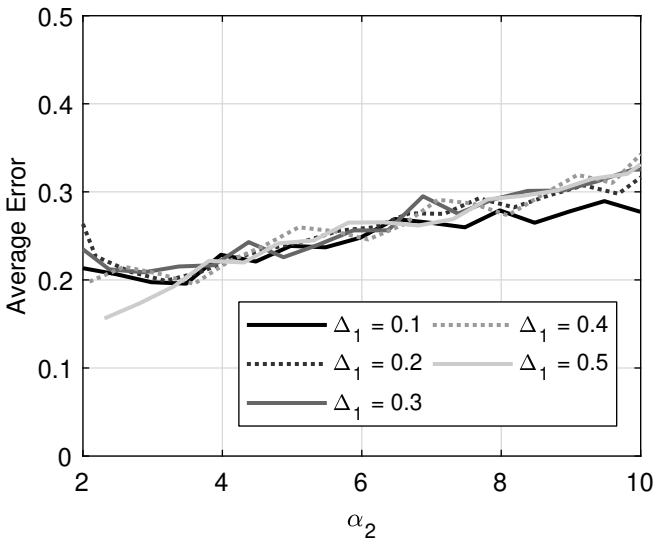

(b)

Figure 6.6: (a) All NLTHA and equation damping values grouped by Δ_1 and (b) error between each damping pair

equation condenses down to a Friction Pendulum EVD equation when $\beta_2 = 1$, making it only dependent on α.

Error Sources

Errors are inherent when approximating a nonlinear system with a linear one. The damping can be both under and over-predicted based on how the EVD equation was derived as well as how damping is estimated in the NLTHA. For example, the derivation of the EVD expression is based on a symmetric hysteretic response, and it has been shown previously that this can cause error in a VFS equation's damping estimation when response is asymmetric [Timsina and Calvi, 2018]. The symmetry of the force-displacement curve largely depends on the input ground motion and re-centering capabilities of the device. Since the AVF devices presented have re-centering capabilities thanks to the restoring force of gravity, an asymmetric response is assumed to be a small source of error. However, further research is needed to prove this assumption and develop a more finely-tuned EVD expression.

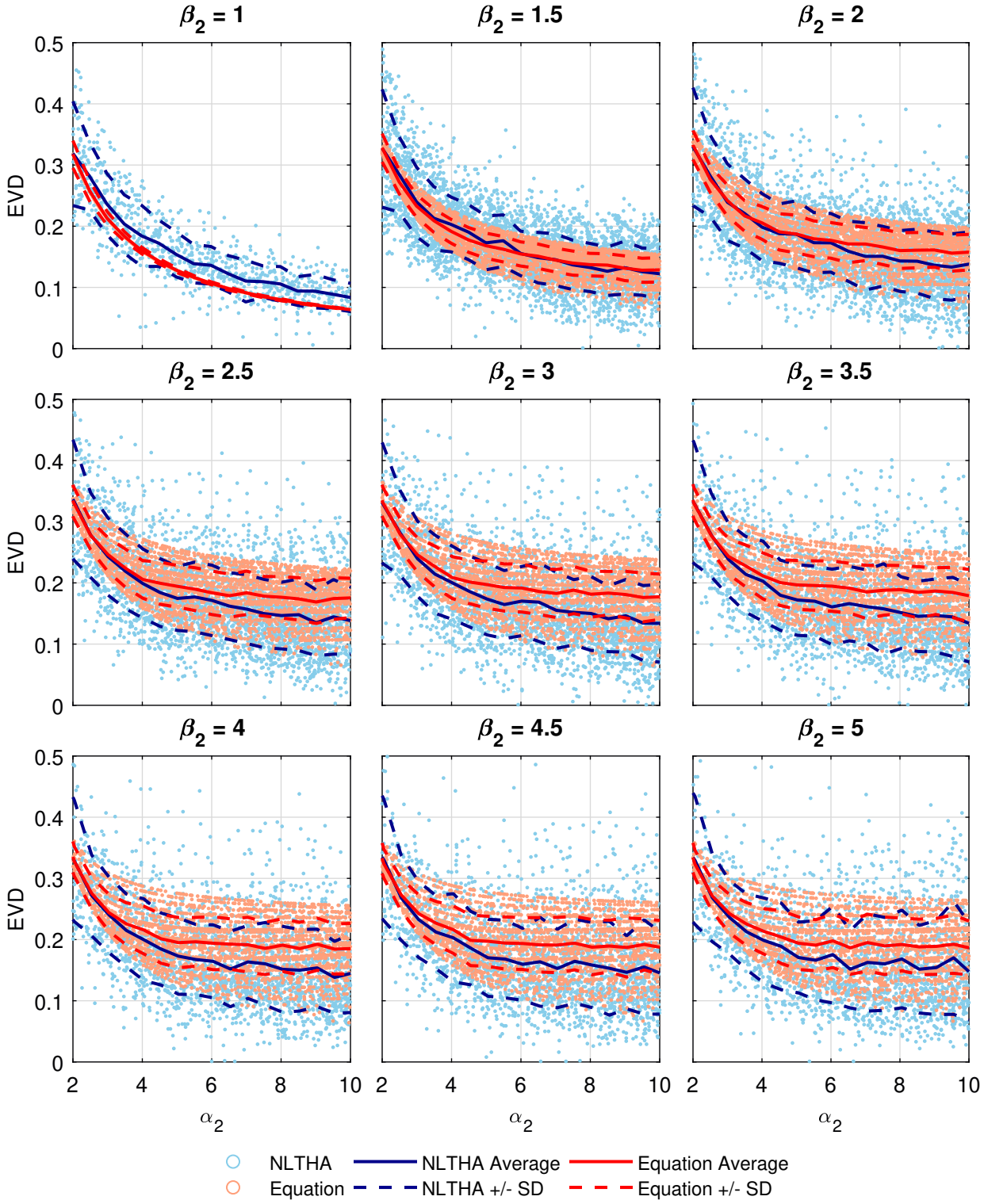

Figure 6.7: (a) All NLTHA and equation damping values grouped by β_2 and (b) error between each damping pair

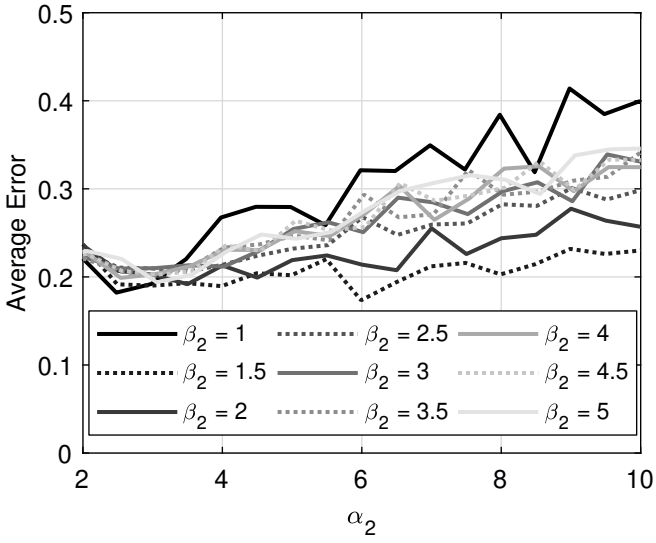

Figure 6.7: (a) All NLTHA and equation damping values grouped by β_2 and (b) error between each damping pair

The NLTHA under-predicts the EVD with how the damping is assigned to an equivalent linear system. If α_2 is large, then a large portion of the hysteretic stiffness will be comprised of the second post-elastic stiffness, which is stiffer than the equivalent secant stiffness used when finding the EVD of a linear system. Assigning a damping value using a lower equivalent stiffness causes the damping to be under-predicted, since it will reach the same maximum displacement as the nonlinear system using less force.

In addition to under-prediction due to the equivalent stiffness, the NLTHA can under-predict damping due to the device getting "stuck", with a qualitative example depicted in Figure 6.8. A device can get "stuck" when it is pushed to a large displacement past $\Delta_{critical}$ and never gets pushed back during the ground motion. This causes the device to stay on second ring have large displacements since it cannot re-center easily. If the equivalent linear system cannot reach that maximum displacement when EVD = 0%, then a damping value of 0 is assigned to the system. Realistic devices would be designed to not get "stuck", so this should not be a problem in actual systems. This study looked at all combinations of devices, including ones that experience demand greater than what they would realistically be

designed for. Additionally, devices can never get stuck when $\beta_2 = 2$ or less because $\Delta_{critical} = \infty$. Both large α_2's and devices getting "stuck" are reasons why the EVD assigned in the NTLHA tends to be less than the derived damping equation.

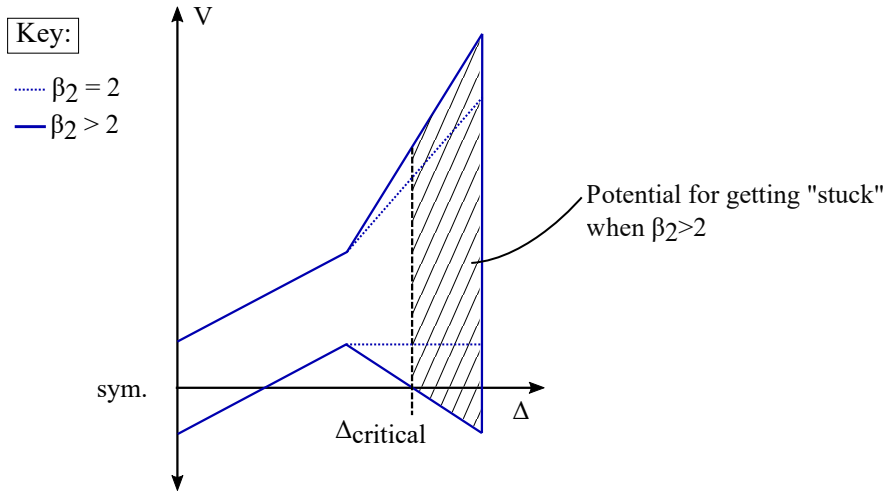

Figure 6.8: $\Delta_{critical}$ example

6.5 Conclusions

This chapter has shown the derivation of the equivalent viscous damping expression for an Adaptive VFS and presented the analyses of an extensive numerical study. The damping equation was derived based on a classic Jacobsen approach and was compared to the results of NLTH analyses in order to validate the expression. These results were plotted against α_2, grouped by the parameter of interest in order to analyze the findings. Particularly of interest in the numerical study were the parameters Δ_1, β_2, and α_2 as they greatly affect AVF bearing behavior. It was seen that the derived equation follows the trend of the NLTHA for increasing Δ_1 and β_2. It was also seen that increasing Δ_1 decreases the average damping, and increasing β_2 increases the spread of the data.

The error between the derived equation to every data point from the analysis was calculated, grouped by the parameters of interest. β_2 showed interesting trends in error: the

FP had the most error out of all β_2's studied, whereas $\beta_2 = 1.5$ had the lowest overall error. Overall, the damping equation derived follows the trend of the NLTH analyses and provides a reasonable means of approximating damping of AVF bearings in design, but further research could be performed to tune the equation for β_2 and Δ_2.

Chapter 7

DESIGN PROCEDURE, VERIFICATION, AND PERFORMANCE COMPARISON OF AVF BASE ISOLATED SDOF SYSTEMS

Chapter 4 showed that the AVF device exhibits favorable behavior in terms of reducing displacement capacity while maintaining re-centering capabilities. This chapter will define a design procedure and perform NLTH analyses to ensure the procedure's accuracy and effectiveness for SDOF systems. Additionally, this chapter will continue to characterize the behavior of AVF isolated SDOF systems by including the behavior of flexible structures, and the behavior of these systems will be compared with that of equivalent Friction Pendulum systems.

The design approach follows the recommendations of [Calvi and Ruggiero, 2016; Calvi et al., 2016; Timsina and Calvi, 2018] that the direct displacement-based design method developed by [Priestley et al., 2007b] be implemented for the design of Variable Friction systems. The DDBD method has already been adapted for various VF systems such as the BowTie and BowC [Calvi and Ruggiero, 2016] and is adapted further for AVF systems herein. The design process for the AVF bearing gives the designer control over isolator and structural behavior at two demand levels, allowing for multiple performance objectives to be met simultaneously.

In order to test the validity of the proposed design procedure, both rigid and flexible SDOF systems designed for the DBE and MCE level ground motions. The devices were designed for different effective periods at the second demand level ($T_{2,e}$) in order to capture a range of different behaviors. Note, the design demand levels will be referred to as 1 and 2, as the designer can choose any design demand desired. The results of the NLTHA are then

compared, and the effectiveness of the design method is discussed.

7.1 Design Procedure for AVF Base Isolated SDOF Systems

A flexible SDOF system isolated by an AVF bearing is designed by adding, in series, the hysteretic shapes of the structure and isolator to get the system response, as pictured in Figure 7.1. To adapt the design process for a rigid SDOF system, the structure's damping is set to zero and a proportionally large structural stiffness is used.

Some of the notation conventions used in Chapter 5.2.1 are changed in the design process for brevity and clarity. First, the demand level for each parameter is denoted with a '1' or '2'. Second, the SDOF system properties will be denoted with the subscript 'sys', the structure with 'str', and the isolator with 'iso'. In most cases, the parameter will combine the two notations (i.e. '1,iso' for isolator at the first demand level). The displacements of the equivalent SDOF system and structure are no longer denoted with the subscript 'e'; the 'e' subscript is now only used for describing the effective stiffness and period of the system. Lastly, since the force is the same in the system, structure, and isolator in the SDOF system, the force will only be denoted with a subscript corresponding to demand level.

It is assumed in this design formulation that all masses are lumped together (i.e. no mass is associated with isolator); this means that the force in the isolator will be the same as the force in the structure. Mass associated with the isolator will be thoroughly studied in Chapter 8. Additionally, the assumption of V_0 occurring at zero displacement was acceptable for the isolator due to the large activation stiffness; however, when a flexible structure is considered, this assumption is no longer valid. Therefore, the activation force V_0 is modeled to occur at the displacement V_0/K_{str}.

The design process is outlined in Figure 7.2; to adapt for a rigid system, as previously mentioned, the structure's damping should be set to zero, and a stiffness that is proportionally large to the post-activation stiffness should be used for the structural stiffness. The proposed design procedure consists of two parts: Part 1) designing the first friction ring for the first demand level (denoted in blue in Figure 7.2), and Part 2) designing the outer ring

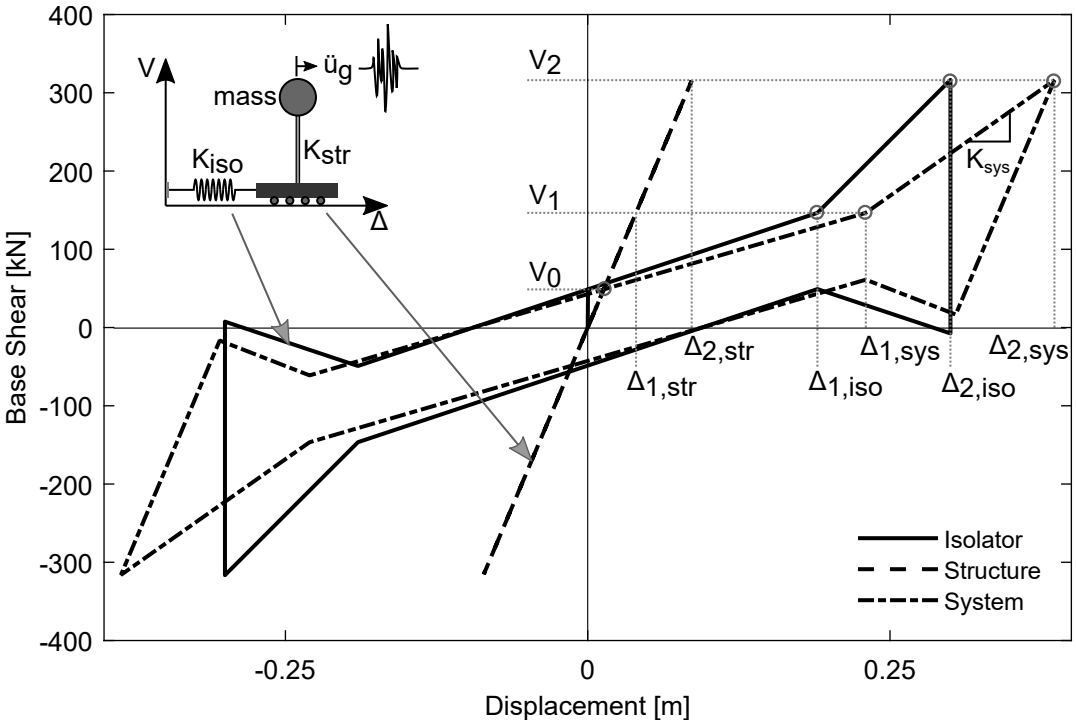

Figure 7.1: Hysteresis for the SDOF structure, isolator, and system

for the second demand level (denoted in red in Figure 7.2). Other design objectives could be envisioned, e.g. the demand levels not corresponding to rings one and two; however, the ring transitions present national controls for different performance objectives, and is therefore used as a division in this design process. This division allows the device to behave as a Friction Pendulum at DBE demands, and have adaptive behavior at an MCE demand, achieving two different design objectives with the same device.

7.1.1 Part 1: First Demand Level

In Part 1 of the process, the designer chooses the ratio between the first design shear and isolator activation shear (α_1) and the SDOF structure and isolator displacement at the first demand level ($\Delta_{1,str}$ and $\Delta_{1,iso}$, respectively). The value of α_1 is recommended to be between 2 and 5, as these are the limits on currently manufactured devices [FIPIndustriale, 2016]. A structure's damage level is usually correlated to a drift value, which is decided by the building owner and designer. For an SDOF system, the structural displacement at the first demand level ($\Delta_{1,str}$) is associated with the chosen drift (θ_1) and can be calculated by multiplying the chosen drift level with the height of the structure. Similarly, the first displacement of the isolator ($\Delta_{1,iso}$) is chosen based on the displacement restraints of the designer, such as preventing pounding of close structures in an earthquake. The displacement capacity of a pendulum is theoretically only limited by manufacturing capabilities, and can be as small as $\pm$ 0.1 meters. Recommendations for picking displacement values for Friction Pendulum systems can be found in [Cardone et al., 2009]; however, this is an area that requires further research. Lastly, the structure's elastic damping, ξ_{str}, is also assigned at this point; damping ratio values and modeling considerations are is discussed in Section 7.1.1.

Next, the system displacement at the first demand level ($\Delta_{1,sys}$) can be calculated using Equation (5.4). The isolator damping ($\xi_{1,iso}$) and system damping ($\xi_{1,sys}$) at this level can also be calculated using Equations (6.12) and (5.7), respectively. The displacement spectrum corresponding to the first demand level is then reduced, which can be done using a variety of methods. As previously discussed, [Timsina and Calvi, 2018] used the Eurocode reduction

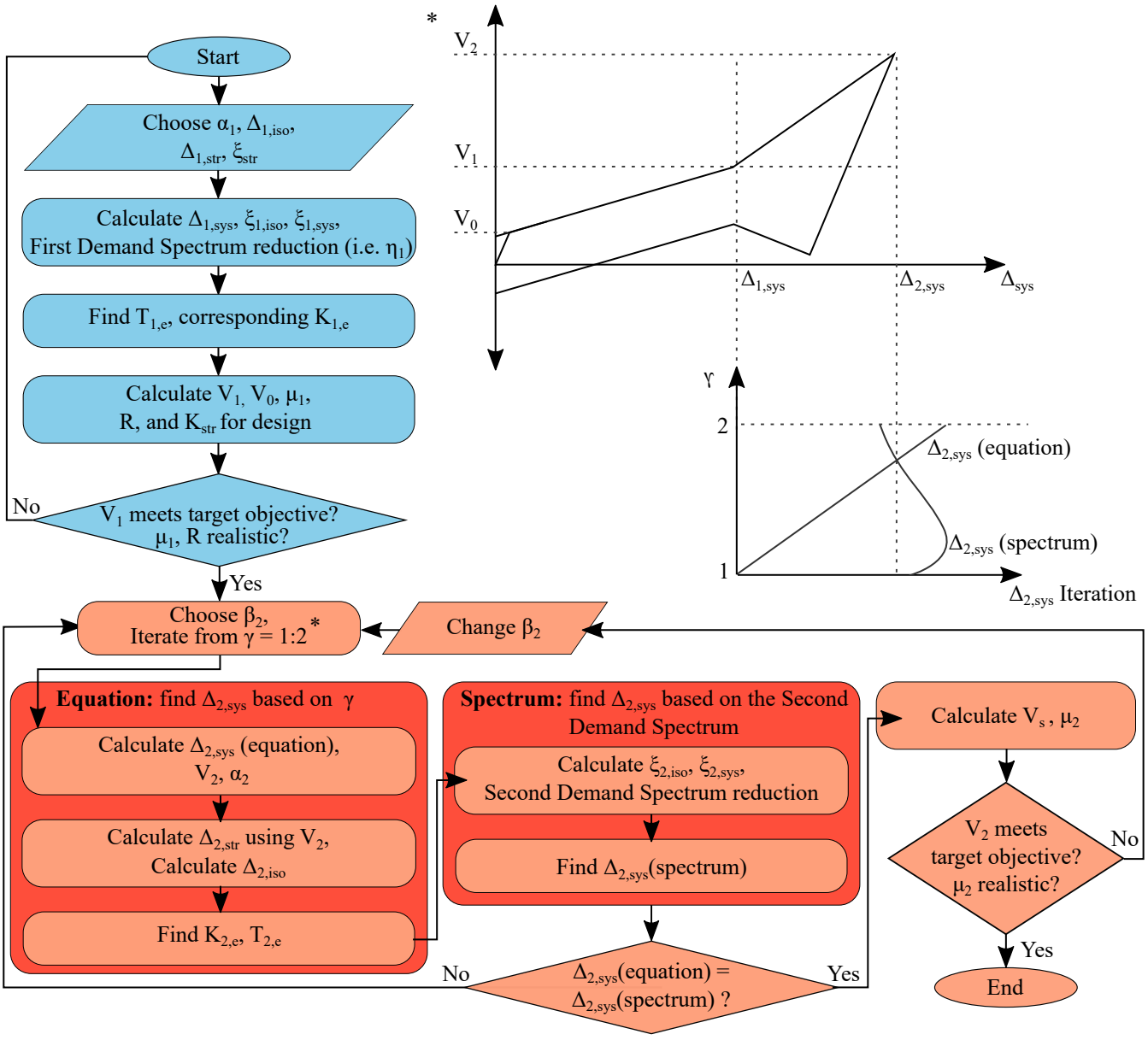

Figure 7.2: Design procedure for AVF base isolated SDOF systems

factor (Equation (5.2)) to reduce the spectrum for BowTie and BowC design. In this study, the spectrum will be reduced by creating a response spectrum for each ground motion with the given damping in order to eliminate any possible sources of error when evaluating the design method (a designer can use any plausible method to reduce the spectrum). An effective system period at the first demand level ($T_{1,e}$) is then found from the reduced spectrum. When using the Eurocode reduction factor, the system period can be found as:

$$T_e = \frac{T_{spec}\Delta_{sys}}{\eta\Delta_{spec}} \tag{7.1}$$

where T_{spec} and Δ_{spec} define the limits of the displacement spectrum and η is the reduction factor. T_{spec} and Δ_{spec} change to reflect different demand levels, but the equation format does not change. The corresponding effective stiffness K_e is calculated by inverting Equation (5.8).

The shear corresponding to the first demand level (V_1) is calculated by multiplying the effective stiffness $K_{1,e}$ with the system displacement $\Delta_{1,sys}$ (Equation (5.9)). The isolator activation shear V_0 can be calculated by dividing V_1 by α_1, a previously selected parameter. μ_1 can then be calculated using Equation (7.2):

$$\mu_1 = \frac{V_1}{\alpha_1 W}, \tag{7.2}$$

where W is the weight of the system. The radius of curvature R can be calculated using the isolator displacement and post-elastic slope of the isolator:

$$R = \frac{W\Delta_{1,iso}}{(V_1 - V_0)}. \tag{7.3}$$

Finally, the structural stiffness required to meet the first demand level is calculated as:

$$K_{str} = \frac{V_1}{\Delta_{1,str}}. \tag{7.4}$$

The designer can move on to Part 2 if V_1 meets their target objective and μ_1 and R can be manufactured.

Numerical Modeling of Structural Damping in SDOF Systems

It has been common practice to use initial-stiffness based viscous damping for NLTHA, in part due to the lack of consensus in how equivalent viscous damping of base isolated structures should be modeled [Pant et al., 2013; Petrini et al., 2008]. This method of modeling damping has been shown by [Petrini et al., 2008] to yield damping forces that are unrealistically high, which can lead to unconservative results. Per the recommendations of [Pant et al., 2013] and [Petrini et al., 2008], a tangent stiffness proportional damping was used to estimate the damping force of the SDOF system. This damping is calculated every time-step and is based on effective stiffness of the system. Additionally, it was shown by [Pant et al., 2013] that using a damping ratio of 1% is more appropriate for simulating a response than 5%; therefore, a 1% damping ratio will be used for the structure. Damping for MDOF systems will be considered in Chapter 8.2.2.

7.1.2 Part 2: Second Demand Level

Part 2 of the design process begins with choosing the second post-elastic isolator stiffness via β_2; other equivalent approaches could be used as well, such as choosing μ_2. As previously discussed, β_2 has a large effect on maximum displacement, force, and residual displacement; therefore, control over the slope is given so that the designer can balance the trade-off between higher force resistance and higher residual displacement.

Once the second post-activation slope is chosen, there is only one force and displacement pair at the second demand level that is compatible with the design spectrum. To find the compatible pair, $\Delta_{2,sys}$ is calculated using both γ and the second level demand spectrum, referred to as $\Delta_{2,sys}$(equation) and $\Delta_{2,sys}$(spectrum), respectively. When $\Delta_{2,sys}$(equation) and $\Delta_{2,sys}$(spectrum) are equal, the designer has found the maximum system displacement compatible with the second post-activation slope chosen and the response spectrum.

Different values of γ are used to find the compatible force and displacement. It is recommended that the γ iteration begin at 1 (i.e. starting at $\Delta_{1,sys}$) and go until equilibrium is reached (this will usually be less than 2). For each iteration, $\Delta_{2,sys}$(equation) is calculated using Equation (3.9). Once $\Delta_{2,sys}$(equation) is known, the shear at the second demand level, V_2, can be calculated using the system stiffness:

$$V_2 = V_1 + \frac{1}{\frac{1}{K_{str}} + \frac{1}{\beta_2 \frac{W}{R}}}(\Delta_{2,sys}(\text{equation}) - \Delta_{1,sys}) \tag{7.5}$$

The ratio between the second shear and isolator activation shear (α_2) can then be found given V_2 (Equation (3.8)). Since the force in the isolator is the same as the force in the structure, the structure's displacement at the second demand level, $\Delta_{2,str}$, can be found by dividing the second shear by the structure's stiffness. The isolator displacement at the second demand level ($\Delta_{2,iso}$) can then be found using Equation (5.4). The damping of the AVF isolator, $\xi_{2,iso}$, is estimated using Equation (6.11), which was previously derived in Chapter 6. If the building is designed to stay linear elastic, the structure damping ξ_{str} remains unchanged; otherwise, the designer must assign a damping value appropriate with the damage state.

The effective system stiffness, $K_{2,e}$, and period, $T_{2,e}$, corresponding to the second demand level can be calculated using Equations (5.9) and (5.8). Using the displacements and damping values associated with the second demand level, the system damping is found using Equation (5.7). Similar to Part 1, the system damping at the second demand level is used to reduce the second demand displacement spectrum using Equation (5.2). Using the reduced spectrum and effective period of the system, $\Delta_{2,sys}$(spectrum) can be calculated by solving Equation (7.1) for Δ_{sys} and plugging in the calculated η.

With both $\Delta_{2,sys}$(spectrum) and $\Delta_{2,sys}$(equation) calculated, the designer can compare the two values. If they are equal, the designer can move on and calculate the second coefficient of friction, μ_2 (Equations (3.12) and (3.13)). If they are not equal, the designer must increase γ and repeat Part 2. The design is complete if the second shear force and second structure and

isolator displacements meet the desired performance objectives, and the second coefficient of friction can be manufactured. If any of these performance objectives are not met, the designer can adjust the β_2 value and begin Part 2 again.

Iteration vs. Closed Form Solution

The iterative process above can also be replaced with a closed form solution. The second system design displacement can be written as:

$$\Delta_{2,sys} = \sqrt{\frac{7}{2+\xi_{2,sys}}}\frac{\Delta_{spec}}{T_{spec}}T_{2,e}, \tag{7.6}$$

which can be expanded to:

$$\Delta_{2,sys} = \sqrt{\frac{7}{2+\left[\frac{\xi_{str}\Delta_{2,str}+\xi_{2,iso}\Delta_{2,iso}}{\Delta_{2,sys}}\right]}}\frac{\Delta_{spec}}{T_{spec}}2\pi\sqrt{\frac{m\Delta_{1,sys}\gamma}{V_1+\frac{\Delta_{2,sys}-\Delta_{1,sys}}{1/K_{str}+1/(\beta_2 W/R)}}}. \tag{7.7}$$

Quickly, one can see that solving for $\Delta_{2,sys}$ is not straightforward given that $\xi_{2,iso}$, $\xi_{2,iso}$, γ on the right hand side of the equation also depend on $\Delta_{2,sys}$. The closed form solution yields an expression that would itself require numerical methods (e.g. Newton-Rhapson) to solve and was therefore not used as the design method.

7.2 Design Validation for Adaptive Variable Friction Base Isolated SDOF Systems

7.2.1 SDOF Case Study Systems

Demands

In order to test the ability of the AVF system design process to predict behavior, a series of rigid and flexible SDOF systems isolated with both AVF bearings and Friction Pendulums were designed. The devices were designed for far-field ground motions scaled to the demand of five different U.S. cities, including a set of pulse ground motions; these ground motions

and spectra are defined in Chapter 3.2.3. These different demands were chosen in order to demonstrate that the design process can accurately represent the real response regardless of input. In order to find the response at two demand levels, each analysis was run twice: once with ground motions scaled to the first demand level, and once at the second demand level.

During the design validation process, it was found that the reduction factor, η, did not represent the actual reduction of the spectrum well in all cases, especially with pulse ground motions, introducing additional error into the design process. Because of this, and the fact that the reduction factor is not an intrinsic part of the design process, the actual demand from the reduced spectrum was used in lieu of the Eurocode reduction factor. It is necessary that the reduction method used in design be accurate for the ground motions considered.

Rigid and Flexible Structures

A set of rigid and flexible structures were considered for the validation of the isolator design method. Both structures had a height of 4 m and a seismic mass of 160 tons, which yields a pressure 50 MPa on a 0.2 m diameter bearing. Note, the slider diameter was increased for the San Francisco pulse devices to match the distance the isolator slides onto the second ring (i.e. $\Delta_{2,iso}$ - $\Delta_{2,iso}$) in order to maintain bi-linear hysteretic behavior. This adjustment results in a slightly lower pressure on the slider. The flexible structure had a story drift at the first demand level of 1%. Though this drift would most likely cause yielding in the superstructure, it was chosen in order to see the effects of a flexible structure on the accuracy of the design predictions. As discussed in Section 7.1.1, a damping of 1% was assigned to the flexible structure. For the rigid structure, a structure damping and design structure displacement ($\Delta_{1,str}$ and $\Delta_{1,str}$) of 0% and 0 m, respectively was assigned.

Isolators

A summary of the devices studied can be found in Table 7.1. A set of four isolators were designed for each of the six demand spectra considered. Each of the four isolators were paired with the rigid and flexible structure, yielding 24 rigid and 24 flexible systems studied. The

rigid systems are odd numbers between 1 and 47, and the flexible systems are even numbers between 2 and 48.

In order to compare the response of the isolation devices between the rigid and flexible structures, the same input design parameters $\Delta_{1,iso}$, α_1, and β_2 were used in both the rigid and flexible isolator designs. A range of input design parameters were chosen to reflect the range of values a designer may use when applying the AVF device to a project. Three of the devices for each city demand were designed as AVF bearings ($\beta_2 > 1$). The fourth isolator designed for each city demand was a Friction Pendulum ($\beta_2 = 1$), which allowed for a behavior comparison between FP and AVF bearings in a design setting. The FP device was designed to be equivalent to the AVF bearing at the first demand level (i.e. the devices have the same input $\Delta_{1,iso}$ and α_1, and therefore the same R and μ_1).

Note, most of the friction and radii of curvature values denoted in the design are currently manufactured, but some of the values are not currently produced commercially. The goal of this chapter is to show the accuracy of the design process in a variety of cases not necessarily bounded by current manufacturing technology.

Table 7.1: Isolators considered in SDOF design validation

Parameter	#	α_1	β_2	$\Delta_{1,iso}$	$\Delta_{2,iso}$		R		μ_1		μ_2		$T_{2,e}$	
Rigid, Flexible	R,F	R/F	R/F	R/F	R	F	R	F	R	F	R	F	R	F
Los Angeles	1, 2	2.0	1	0.25	0.57	0.54	4.6	4.6	5.4	5.5	5.4	5.5	3.60	3.76
	3, 4	2.0	5	0.25	0.41	0.38	4.6	4.6	5.4	5.5	22.6	22.9	2.44	2.74
	5, 6	2.0	5	0.31	0.47	0.47	7.0	7.0	4.5	4.4	16.0	15.9	3.04	3.34
	7, 8	2.5	5	0.38	0.55	0.56	7.1	7.3	3.6	3.5	14.8	14.5	3.24	3.53
Portland	9, 10	2.0	1	0.12	0.24	0.23	2.2	2.6	5.4	4.7	5.4	4.7	2.45	2.93
	11, 12	2.0	2	0.12	0.22	0.22	2.2	2.6	5.4	4.7	14.4	12.4	2.12	2.63
	13, 14	2.5	2	0.16	0.29	0.28	3.2	3.8	3.4	2.8	9.6	8.1	2.66	3.27
	15, 16	2.0	2	0.16	0.29	0.29	5.4	6.4	3.0	2.5	6.7	5.6	3.29	4.01
San Diego	17, 18	3.0	1	0.20	0.40	0.38	3.1	3.5	3.2	2.8	3.2	2.8	3.16	3.62
	19, 20	3.0	4	0.20	0.30	0.30	3.1	3.5	3.2	2.8	22.5	19.8	2.32	2.82
	21, 22	2.5	4	0.20	0.32	0.33	4.4	6.3	3.0	2.1	16.7	11.7	2.63	3.57
	23, 24	2.0	4	0.19	0.33	0.32	6.5	9.1	2.9	2.1	12.2	8.7	3.03	4.12
San Francisco	25, 26	3.0	1	0.20	0.44	0.41	2.6	2.6	3.9	3.9	3.9	3.9	2.91	3.12
	27, 28	3.0	2	0.20	0.33	0.33	2.6	2.6	3.9	3.9	11.6	11.7	2.47	2.73
	29, 30	2.5	2	0.24	0.43	0.43	4.7	4.7	3.4	3.4	7.7	7.7	3.22	3.51
	31, 32	2.5	2	0.27	0.49	0.48	6.0	5.8	3.0	3.1	6.7	6.7	3.63	3.88
San Francisco (pulse)	33, 34	2.5	1	0.31	0.60	0.59	5.0	5.3	4.1	3.9	4.1	3.9	3.89	4.18
	35, 36	2.5	2	0.31	0.52	0.52	5.0	5.3	4.1	3.9	8.1	7.9	3.35	3.68
	37, 38	2.5	2	0.34	0.58	0.58	6.3	6.9	3.6	3.3	7.4	6.7	3.76	4.16
	39, 40	2.5	2	0.38	0.65	0.64	8.5	8.7	3.0	2.9	6.1	5.9	4.34	4.66
Seattle	41, 42	3.0	1	0.17	0.35	0.33	2.1	2.2	4.0	3.8	4.0	3.8	2.61	2.93
	43, 44	3.0	3	0.17	0.27	0.26	2.1	2.2	4.0	3.8	23.1	21.6	2.03	2.43
	45, 46	3.0	3	0.19	0.29	0.30	2.7	3.1	3.5	3.1	18.2	16.2	2.32	2.78
	47, 48	3.5	3	0.24	0.37	0.36	3.8	4.1	2.5	2.4	12.9	12.2	2.81	3.23

7.2.2 SDOF Design Results

This section compares the results of the NLTH analyses with the design values. The comparison between design an analysis is done for both maximum shears and displacements at the DBE and MCE demand levels, all of which show satisfactory agreement. The behavior comparison between the FP and AVF devices at the second demand level gives an example of how a designer may compare behavior when choosing a device.

The results from all devices normalized by their respective design values can be seen in Figure 7.3. Each boxplot represents the results from the 20 NLTH analyses (10 pairs of ground motions) performed for the system at one demand level. Demand level one is denoted in blue, and level two is denoted in red. The thick black line in each box plot represents the average of the NLTH analyses performed for that system, and the closer the average is to one, the better the agreement between the design and analysis. Lastly, whiskers represent maximum and minimum values, and the dots represent outliers. The rows of the figure show the results organized by system flexibility, and the columns separates the data by design base shear and isolator displacement.

For the rigid systems, both the first and second demand levels had analysis averages around one for base shear (V_1 and V_2). For isolator displacements, $\Delta_{1,iso}$ was overall more conservative than $\Delta_{2,iso}$. The flexible system base shear had a slightly less conservative design at the first demand level, but the second demand level was on average in agreement with the analysis. The isolator displacement design was on average conservative for both demand levels. Overall, both the rigid and flexible systems show good agreement between design and analysis for both base shear and isolator displacement at the two demand levels for all spectra, including the pulse ground motions. This means that the design process is robust and able to predict system behavior relatively well for a broad range of devices and a broad range of spectra.

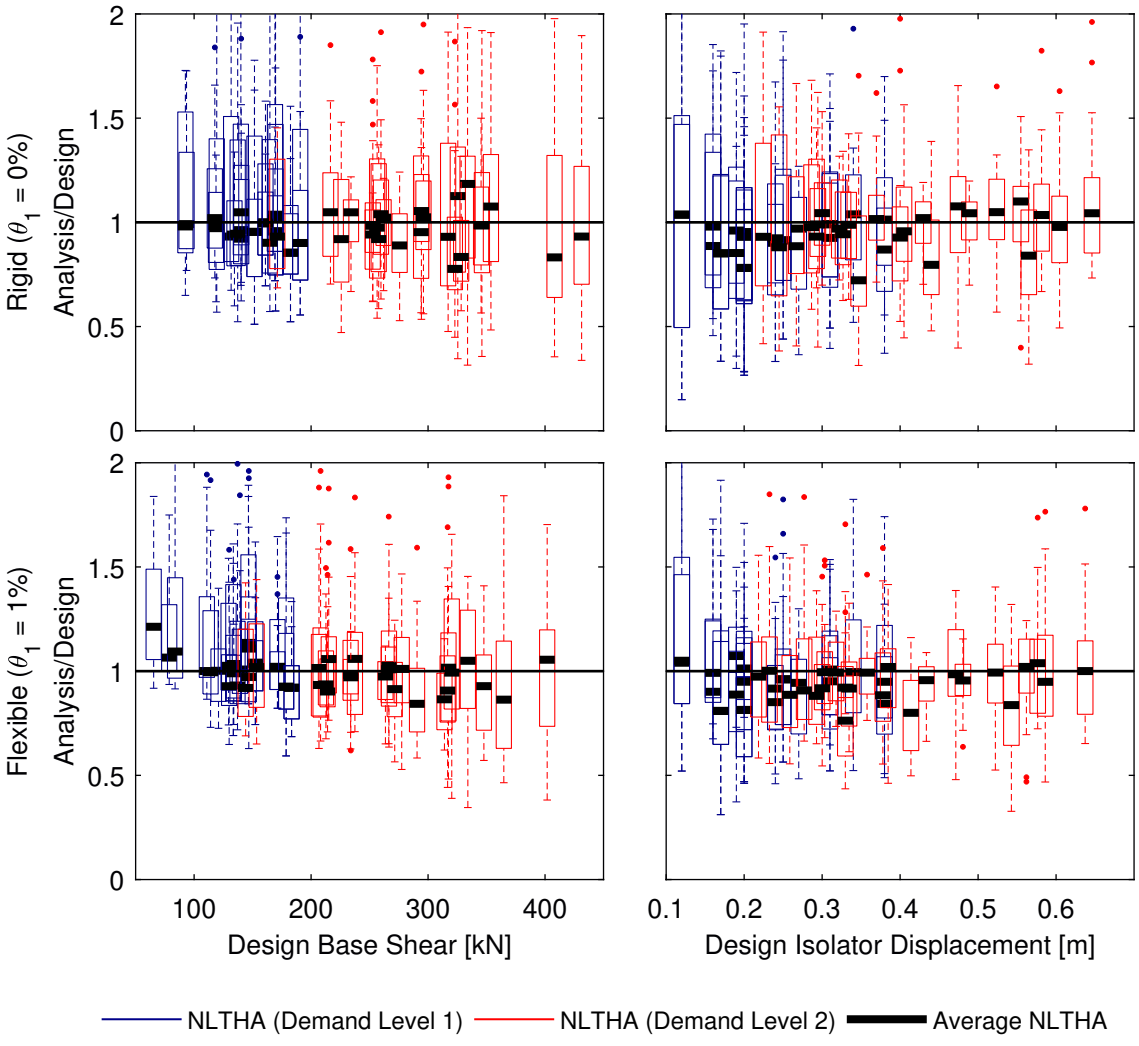

Figure 7.3: Comparison of design and analysis for demand levels 1 and 2

Table 7.2: Isolators considered in SDOF behavior comparison (organized by increasing β_2)

City	β_2	# (R,F)
Portland (PDX)	1	9, 10
	2	11, 12
Seattle (SEA)	1	41, 42
	3	43, 44
San Diego (SAN)	1	17, 18
	4	19, 20
Los Angeles (LAX)	1	1, 2
	5	3, 4

7.3 Preliminary SDOF System Characterization

Twelve Friction Pendulums (6 with rigid, 6 with flexible structures) were designed to match twelve AVF devices at the first demand level. Eight of these FP/AVF design pairs were used for behavior comparison and are denoted in Table 7.2 in increasing order of AVF β_2.

The SDOF behavior comparison is shown in Figure 7.4. Only the second demand level is shown since the devices were designed to have (and did have) the same behavior at the first demand level. The figure shows the response parameters (i.e. maximum force, displacement, and residual displacement) in each row, and the columns separate the data by structure type. Each FP and equivalent AVF pair (denoted in Table 7.2) are ordered by increasing AVF β_2 value.

Overall, similar trends can be seen when comparing the rigid and flexible SDOF systems. The trends for the rigid systems are more pronounced and will therefore be discussed. As expected, the maximum force for the AVF devices is larger than the equivalent FP. The FP also has less variation in maximum force than the AVF bearing does. Conversely, the FP has a higher average displacement and a higher variation than the AVF bearing, especially

for higher β_2 values. This behavior implies that if a designer is designing in an area that has a high seismic demand (i.e. high S_{MS} or S_{M1}) and a large maximum displacement limit, an AVF device may work well since it can achieve a higher force at a lower maximum displacement than a Friction Pendulum. The residual displacement for all β_2 values are low; in some cases the AVF device had a slightly higher residual displacement, but overall the values are nearly equal. This means all devices have excellent re-centering capabilities at this demand level, which is a desirable isolator behavior.

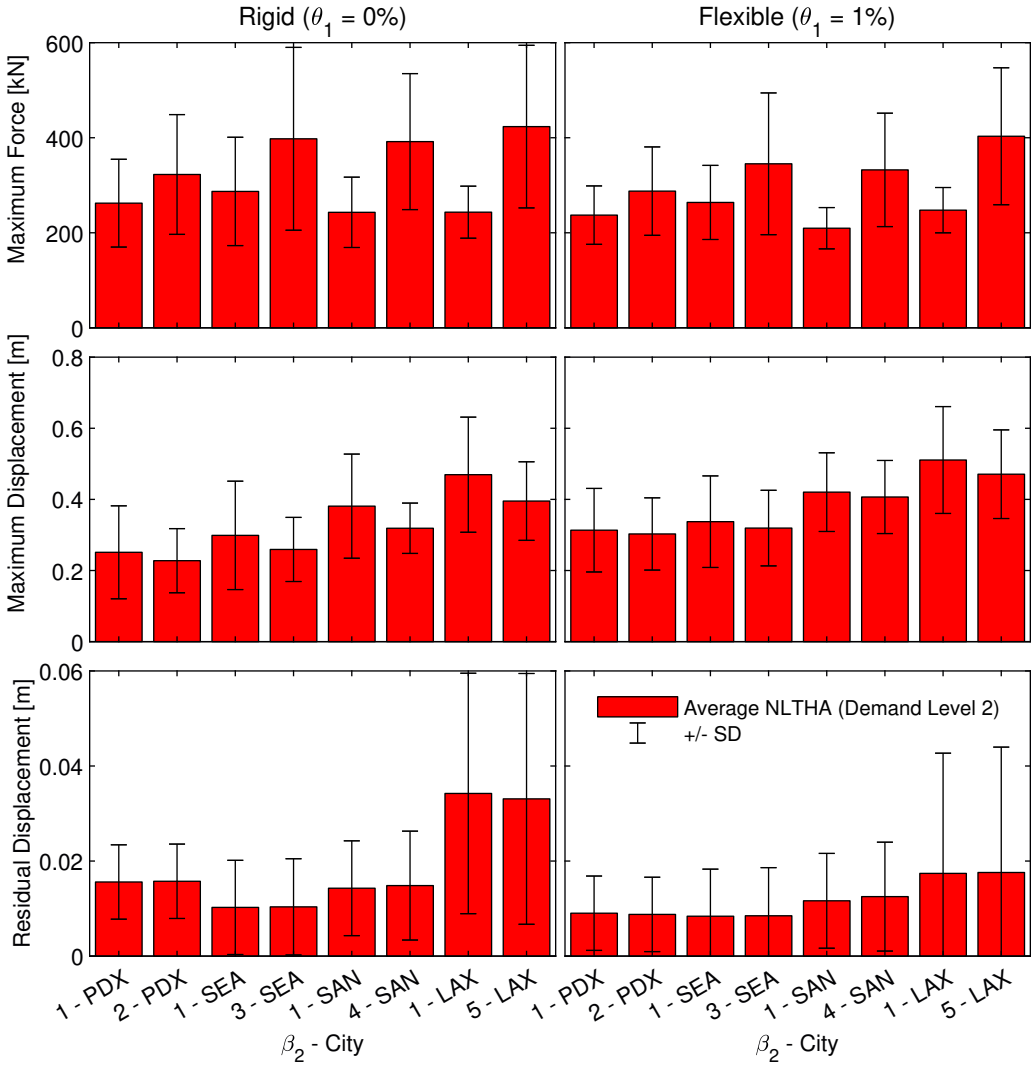

Figure 7.4: Behavior comparison between FP and AVF base isolated SDOF systems

7.4 Conclusions

A design process for an Adaptive Variable Friction device isolating both a rigid and flexible SDOF structure is presented in this chapter. When the designs were compared to the average from 20 NLTH analyses at two demand levels, the agreement was overall excellent for both rigid and flexible structures. This showed that the design procedure is robust and can handle variation when SDOF systems are considered.

The behavior of equivalent FP and AVF devices was presented. The devices followed trends similar to the the parametric study presented in Chapter 4. The AVF devices had a higher maximum force, but a lower maximum displacement when compared to the FP, and all devices exhibited excellent re-centering capabilities. It is up to a designer if force transferred to the structure or displacement is more important. The AVF devices give the designer the ability to control the system response at two demand levels and handle a more-severe earthquake with a smaller displacement capacity.

Chapter 8

DESIGN PROCEDURE AND PERFORMANCE COMPARISON OF AVF BASE ISOLATED MDOF SYSTEMS

When evaluating SDOF systems, the design procedure for AVF systems showed satisfactory accuracy in predicting maximum force and displacement values at two different demand levels. The aim of this chapter is to evaluate and accordingly adjust the design procedure to accommodate a more complicated MDOF structure. Many design alternatives are presented, but are not vigorously tested in a variety of settings like the SDOF systems in Chapter 7, leaving the design of AVFS isolated MDOF systems an area for continued research. While the focus is on exploring the accuracy of design procedures, this chapter also includes a brief study of the difference in behavior between FP and AVF isolated MDOF systems.

8.1 Method 1: MDOF Design Procedure

The design method presented in this section is based on typical direct displacement-based design procedures, and serves as the basis for design methods 2-4, discussed in Sections 8.3.1-8.3.3. The MDOF design adaptation follows the method outlined in Chapter 5.2.1, but this section outlines a more in depth discussion of the adaptation to MDOF design.

The first step for calculating the equivalent SDOF system is to choose the displaced shape of the structure. The displaced shape depends on the type of structural system and the yield displacement of the material, and should be considered on a case-by-case basis. Examples of how to assign a displaced shape for a shear wall and moment-resisting frame system can be found in [Priestley et al., 2007a]. In this research, drift ratios at the first demand level (θ_1) where chosen to be both 0.2 % and 0.4% along the height of the structure. Both θ_1 values resulted in θ_2 values of less than 1%, which is the maximum drift limit to satisfy the

Immediate Occupancy category for concrete frames according to [ASCE, 2000]. Material yielding was not modeled and should be included in more advanced analyses.

Next, the effective system displacement, height, and mass are calculated using Equations (5.3),(5.5), and (5.6). With the equivalent SDOF system calculated, the design process from Chapter 7 is performed. The resulting base shear is distributed up the height of the original structure according to Equation (5.10), and is then used to calculate the story shears. The stiffness of each story is calculated by relating the story shears and displacement. Although having a unique story stiffness each floor may be unrealistic, this method can be used as a first iteration, after which the designer can change the stiffness and iterate for the resulting displacements. It is also recognized that assigning the stiffness to the structure using this method may not pass all design checks (i.e. flexure checks, shear checks, etc.) and therefore again, should be used as a first iteration in a design process for getting a final building stiffness.

Since the story stiffnesses were assigned according to the forces at the second demand level, the displacements at the first demand level were re-solved using the calculated structural stiffnesses. Because of this, the isolator and structure displacements at the first demand level will be slightly different than the values originally chosen. Finally, the resulting design story acceleration is estimated by dividing the story force by the story mass, but in reality, the acceleration will be slightly different due to the damping term in the equation of motion.

8.2 Preliminary Comparison of Method 1 Design and Analysis

8.2.1 MDOF Case Study Structures and Isolators

The case study structures and isolators used for both the design and behavior comparisons are summarized in this section and are loosely based on the well-studied SAC structures [Gupta and Krawinkler, 1999]. Design decisions and properties of the structure are detailed below:

- Six structures were studied: 4, 8, and 12 stories, combined with 0.2% and 0.4% target

Table 8.1: Story stiffness of MDOF case study structures

Stories	θ_1	Story Stiffness [kN/m] 1	2	3	4	5	6	7	8	9	10	11	12
4	0.2%	681,706	517,599	349,279	176,746								
	0.4%	344,369	264,288	180,200	92,103								
8	0.2%	1,341,558	1,187,877	1,030,192	868,504	702,811	533,114	359,413	181,709				
	0.4%	677,712	605,810	530,249	451,026	368,142	281,598	191,393	97,527				
12	0.2%	2,002,890	1,857,019	1,707,323	1,553,802	1,396,456	1,235,286	1,070,291	901,471	728,826	552,357	372,063	187,944
	0.4%	995,023	930,347	862,355	791,045	716,419	638,476	557,216	472,639	384,745	293,534	199,006	101,162

drifts at the first demand level. The story stiffnesses for each structure can be found in Table 8.1. This range was chosen to represent the range of heights for buildings that might realistically benefit from base isolation.

- The mass of each floor was 1,000 tonnes, computed roughly from a 96 psf dead load (4.6 kPa), 20 psf live load (0.96 kPa), and a 42 by 42 m floor size. The mass on each floor, including the isolator level and the roof, were assumed to be the same.

- The demand corresponds to the San Francisco spectrum (non-pulse ground motions) denoted in Chapter 3.2.3.

- A damping ratio of 0% was assigned to the superstructures; this decision is discussed in detail in Section 8.2.2.

The design properties of the isolators used in this chapter are as follows:

- Only one isolator was designed for each case study structure (i.e. six in total). The details for the isolators are included in Table 8.2. Note that additional isolators will be considered in the MDOF behavior comparison.

- The target pressure on the bearing was 50 MPa.

- There were a total of 20 bearings used to isolate each structure.

Table 8.2: Isolator devices considered in MDOF design investigation

Stories	θ_1	α_1	β_2	$\Delta_{1,iso}$	$\Delta_{2,iso}$	R	μ_1	μ_2	$T_{2,e}$
4	0.2%	3	2	0.25	0.42	3.76	3.3%	10.0%	3.06
	0.4%	3	2	0.25	0.41	3.76	3.3%	10.0%	3.14
8	0.2%	3	2	0.25	0.42	3.76	3.3%	12.2%	3.14
	0.4%	3	2	0.25	0.42	3.76	3.3%	12.3%	3.29
12	0.2%	3	2	0.25	0.42	3.76	3.3%	14.1%	3.22
	0.4%	3	2	0.25	0.43	3.81	3.3%	13.9%	3.46

- The resulting bearing radii were 0.12 m, 0.17 m, and 0.2 m for the 4, 8, and 12 story structures, respectively.

8.2.2 Structural Damping Study

There is little consensus as to how structural damping should be modeled, especially in base-isolated systems [Pant et al., 2013]. A small study was conducted for various combinations of damping in the design and analysis, which can be found in Table 8.3. A Rayleigh damping model was used since it has previously been used to study VFS [Timsina, 2017]. The damping model was based on the tangent stiffness of the system and continuously updated, per the recommendations of [Pant et al., 2013]. The damping ratios were assigned to modes 1 and (n-1), where n is the number of stories, since it has been found that Rayleigh damping can produce unrealistically high damping in lower modes [Petrini et al., 2008].

Almost all of the damping combinations evaluated underpredicted the NLTHA displacements, which is similar to the findings of [Ryan and Polanco, 2008]. Future research may try to model damping as stiffness proportional with 1% damping, following the recommendations of [Pant et al., 2013; Ryan and Polanco, 2008], but determining the correct damping model for a base isolated structure is outside of the scope of this research. Since the main purpose of this chapter is to determine the accuracy of the proposed design process through a comparison with NLTHA, a source of error was eliminated by using 0% structural damping

Table 8.3: MDOF Damping Study

#	Analysis Damping	Design Damping	Modes
1	2%	0%	1, (n-1)
2	5%	0%	1, (n-1)
3	0%	2%	1, (n-1)
4	0%	5%	1, (n-1)
5	1%	5%	1, (n-1)
6	5%	5%	1, (n-1)

for both the design and analysis.

8.2.3 Numerical Modeling for MDOF Systems

The MDOF system was modeled in a manner similar to the nonlinear analysis denoted in the Japanese Code [Marino et al., 2005]. The structure is idealized using a column model, as pictured in Figure 8.1. The mass is lumped at each story, connected by springs calibrated to the story stiffness, and only allowed to translate in the x-direction. The isolator was again represented with a nonlinear spring with the appropriate force-displacement relationship assigned.

The numerical modeling program denoted in Chapter 3.2.2 was adapted for MDOF systems and used for the analyses in this chapter. This program was based on the Matlab program used by [Calvi and Ruggiero, 2016] and [Timsina, 2017], which was validated for MDOF systems in a small comparison with results from Ruaumoko 2-D, a dynamic analysis software [Timsina, 2017]. To further validate the program for this research, the results of a response spectrum analysis for a fixed base, four story case study structure were compared with the NLTHA program results. The force, displacement, and acceleration results from a ground motion matched the program's values well, so the adapted program was used for the MDOF analyses presented in this chapter.

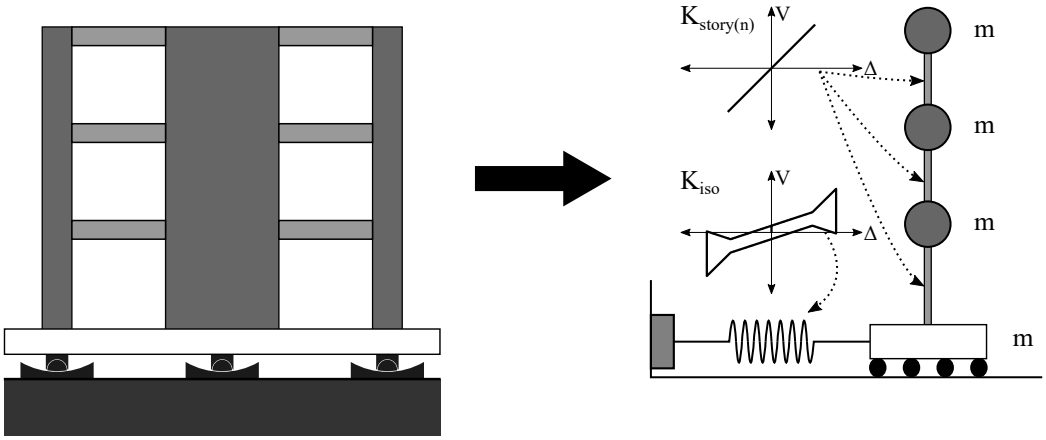

Figure 8.1: Schematic of structural model considered by NLTHA program for MDOF systems

Discussion on Errors in Numerical Modeling

When producing the analysis results for Method 1, it was discovered that the story accelerations were occasionally artificially high. Upon closer examination, it was discovered that there were periodic force spikes at the isolator level, leading to acceleration spikes, which can be seen in Figure 8.2. This figure shows force and absolute acceleration at the isolator level of the first case study structure, subjected to ground motion 32 (direction "0") at the second demand level. This phenomenon has been experienced by other researchers [Wiebe and Christopoulos, 2010], who have concluded that these spikes increase the force and acceleration of a structure, but do not largely affect the displacement and drift. Therefore, the drift and displacements from all previous analyses were assumed to be unaffected by this phenomenon.

Some researchers attributed the acceleration spikes to modeling choices, namely to spurious accelerations caused by piecewise definitions of restoring force [Wiebe and Christopoulos, 2010]. To investigate the effects of different modeling decisions, a small study was conducted to see how the absolute acceleration at the isolator is changed by modeling decisions, and the results from the study are shown in Table 8.4. All of the scenarios listed had a maximum number of iterations of 10,000 for the Newton-Rhapson algorithm, and a corresponding error

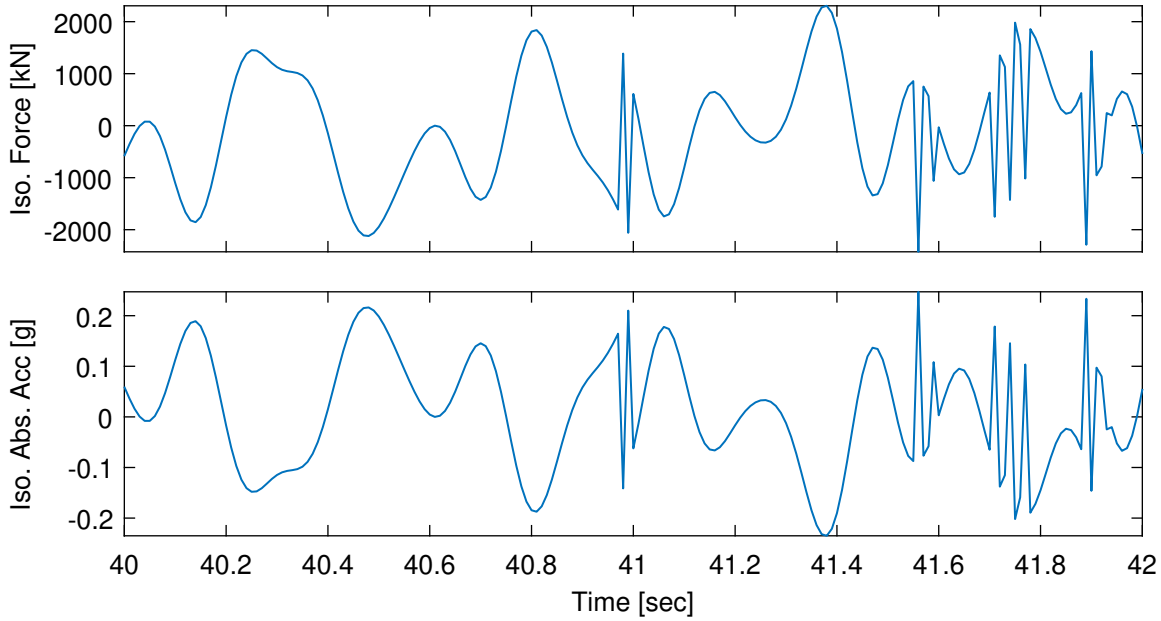

Figure 8.2: Example of displacement and acceleration spikes in isolator NLTH data (Initial Stiffness Multipler: 100,000; Error Tolerance: 1e-5; # of Times Interpolated: 2)

tolerance. The interpolation value represents the number of times the input ground motion was dissected. The values in the table are ordered by increasing interpolation value.

From the small study, it can be seen that a higher number of interpolation results in a more accurate absolute acceleration value at the isolator level. Additionally, large acceleration spikes are more common in systems with higher initial stiffnesses, regardless of the number of interpolations. Finally, the system with 1% damping in the analysis was more affected by modeling decisions than the system with 0% damping in the analysis. This further confirmed the decision to use 0% structural damping for the design verification and MDOF behavior study.

Acceleration spikes may be eliminated depending on modeling decisions, but these decisions are not the same for each ground motion, scale factor, structure, and isolator. Additionally, the higher the number of iterations, the greater the computational cost. Therefore, it was decided to minimize the effects of the acceleration spikes by calculating the acceler-

Table 8.4: Resulting absolute acceleration at isolator level for variations modeling decisions

Initial Stiffness Multipler		100,000	100,000	100,000	100,000	1,000,000	100,000	100,000
Error Tolerance [kN]		1.00e-05	1.00e-06	1.00e-06	1.00e-07	1.00e-07	1.00e-07	1.00e-07
# of Times Interpolated		2	2	5	10	10	20	40
Isolator Absolute Acceleration [g]	0% damping	0.629	0.623	0.674	0.631	0.629	0.616	0.614
	1% damping	2.287	2.183	1.371	0.721	4.769	0.771	0.732

ation similarly to the design method, or the story force divided by the story mass. This calculation serves as a satisfactory estimate of acceleration, especially for structures with a 0% damping ratio. Further, it was decided that the typical modeling decisions would be a number of interpolations of 20, error tolerance of 1e-7 when measuring force in kN, and initial stiffness multiplier of 100,000 since these parameters resulted in the most converged acceleration values for the lowest computational time.

The artificially high acceleration can be addressed in future research in two ways: integrate Bézier curves into the isolator force-displacement numerical model, or use the concurrently developed 3D VFS OpenSees model [Yang et al., 2019a]. The use of Bézier curves was proposed by [Wiebe and Christopoulos, 2010], who concluded that the peaks in acceleration were largely attributed to a sudden change from low stiffness to high stiffness at high velocities. The Bézier curves would smooth the transition from the initial stiffness to the post activation stiffness, theoretically eliminating the issue. This approach, however, continues to model the isolator in 1D. It is therefore recommended that future research use [Yang et al., 2019a]'s more realistic and complex 3D algorithm to better characterize the behavior of VF systems. For this study, the force and acceleration values presented should be treated with skepticism, but the displacements are more trustworthy.

8.2.4 Results for Method 1

The parameters of interest in MDOF systems, namely maximum displacement, story drift, story shear, and absolute acceleration are summarized in Figures 8.3-8.5 for the six described case study systems. The maximum displacement design and analysis results for all six

structures at both demand levels were almost identical, further confirming that DDBD is effective at predicting displacements for base-isolated systems [Pettinga and Priestley, 2005]. The interstory drifts shown in Figure 8.4, however, did not follow the predictions. The drift was best predicted at the first story, but the design value loses accuracy with increased height. This is largely due to the effects of higher modes and will be addressed in subsequent design methods.

The story shear can be seen in Figure 8.5. For all systems and demand levels, the design process adequately predicts the force at the isolator level, which further confirms the accuracy of the design process at the isolator level. The design process does not reflect the increase in force on the second level that most scenarios experience. Similarly, the accelerations shown in Figure 8.6 do not reflect the NLTHA data, but this result should be treated with skepticism as discussed in Section 8.2.3. From this small case study, it can be seen that the displacements are well-predicted, but interstory drift, story shear, and acceleration need an improved method of prediction.

8.3 Design Method Alternatives for Considering Higher Modes

The analysis results for displacement matched Method 1 predictions well, but improvements are needed for drift and force predictions. Higher modes are important to consider in taller structures, and are even more important in base isolated structures, as they have been found to be more prominent [Lee and Mediand, 1978]. This is due to the fact that the higher mode periods of the structure, which are generally small to start, are only slightly increased by isolation, generally moving them into regions of dominate earthquake frequencies. Three additional design procedures trying to address the effects of higher modes were explored and are detailed in this section, and the methods are then compared in Section 8.4.

8.3.1 Method 2: 10% Force Amplification

The first proposed design alternative mirrors concepts found in the New Zealand code for dealing with higher modes [NZS, 2004] and was utilized in the study conducted by [Pettinga

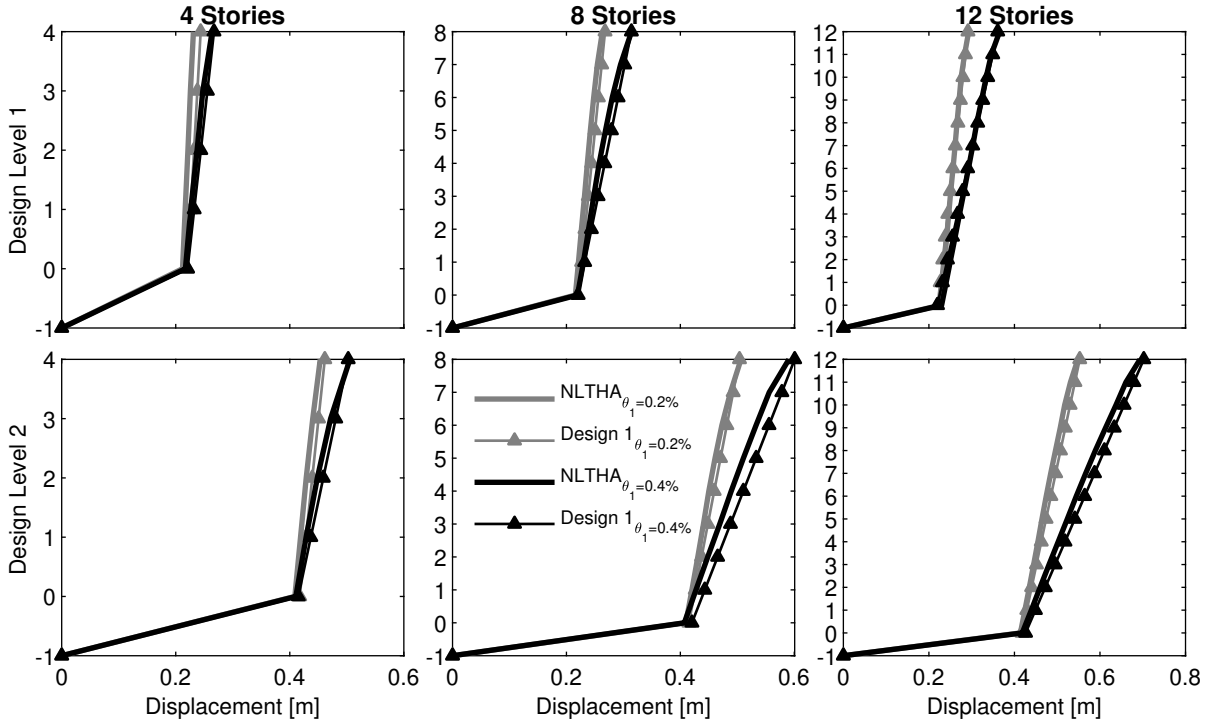

Figure 8.3: Comparison of design Method 1 and analysis for maximum displacement at demand levels 1 and 2

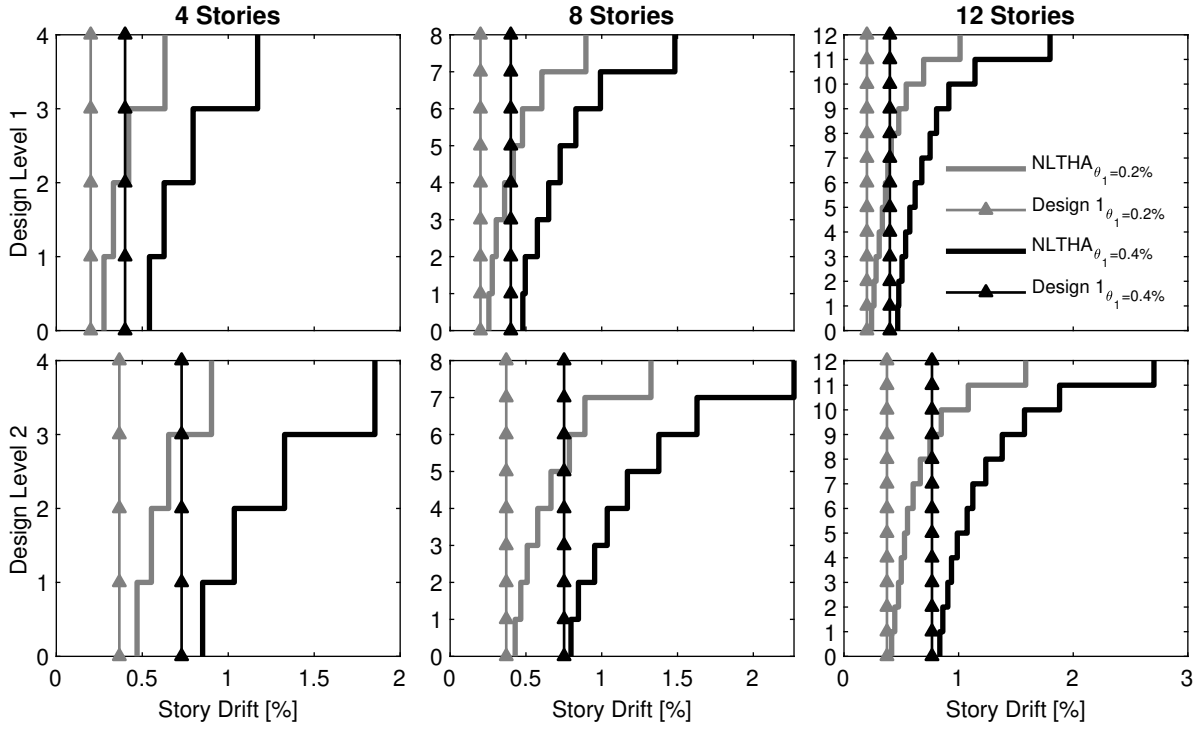

Figure 8.4: Comparison of design Method 1 and analysis for maximum story drift at demand levels 1 and 2

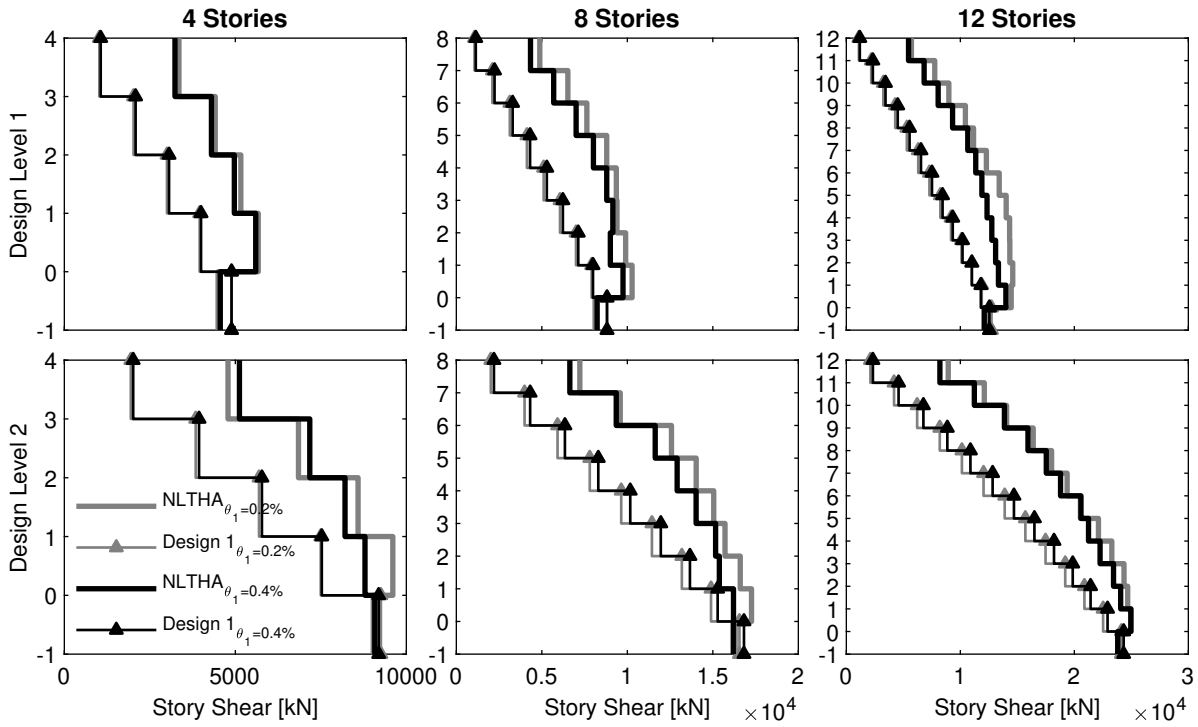

Figure 8.5: Comparison of design Method 1 and analysis for maximum story shear at demand levels 1 and 2

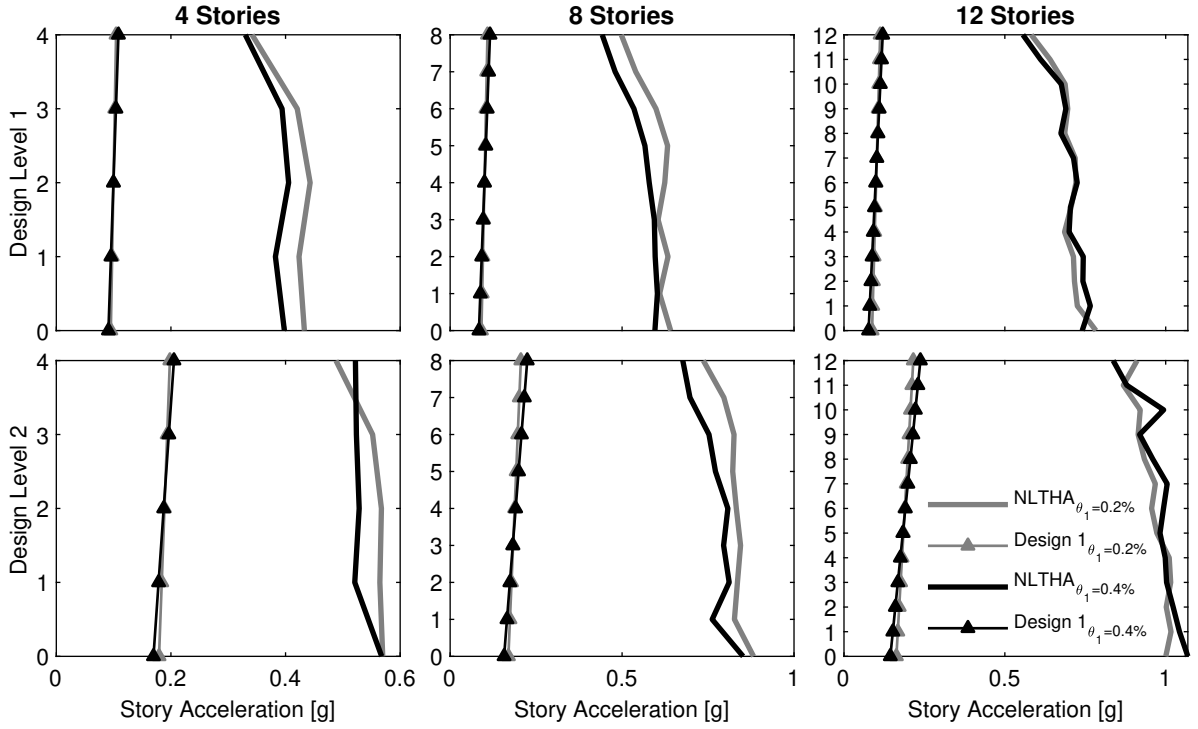

Figure 8.6: Comparison of design Method 1 and analysis for maximum absolute acceleration at demand levels 1 and 2.

and Priestley, 2005]. This approach re-distributes 10% of the base shear V_b to the top of the structure to help control drifts associated with higher modes using the following expression:

$$F_i = F_t + 0.9V_b \frac{(m_i \Delta_i)}{\sum_{i=1}^{n} (m_i \Delta_i)}, \tag{8.1}$$

where $F_t = 0.1V_b$ at the roof level, and $F_t = 0$ at all other levels [Priestley et al., 2007a]. It is recommended that this approach be applied to structures with more than 10 stories [Pettinga and Priestley, 2005], but the method was applied to all the case study structures for the sake of consistency. This makes sense based on the NLTHA results in Figure 8.4.

8.3.2 Method 3: 2 Mode Design

3a: Combine Modes using SRSS

Another method for including the effects of higher modes includes performing a modal analysis on an equivalent fixed-base structure and determining the elastic demands from the second mode. The two modes can then be combined with the first and second level demands by using square-root-sum-of-the-squares, or SRSS, similar to the design modification recommendation of [Pettinga and Priestley, 2005]. The addition of the second mode response in their study greatly increased the accuracy of the design predictions for shear.

3b: Combine Modes using Absolute Value

This method follows the methodology of 3a, but the original demands and elastic second mode demands are added using absolute value instead of SRSS, per the recommendation of [Lee and Mediand, 1978]. The maximum force and displacements for each mode can occur at the same time or different times; adding them with the absolute value assumes that the phase differences are the 'worst' (i.e. maximum) scenario, giving an upper bound for the drift and forces in the system.

8.3.3 Method 4: n Mode Design

As an extension of Method 3a, Method 4 combines elastic modes 2 through n using SRSS to get the overall response of the structure. This method was included to see if the higher modes could be completely predicted by including all modes. Clearly, this method computationally expensive if a computer program is not utilized and therefore may not be practical in all design applications.

8.4 Design Method Comparison

Each of the design methods outlined in Sections 8.1 and 8.3 were used to obtain design displacement, drift, story shear, and absolute acceleration for the case study structures in Table 8.1. The designs were compared with the NLTHA results from Section 8.2.4 and are presented in Figures 8.7 through 8.14.

Each design method did a satisfactory job predicting displacements for all case study systems at both demand levels, shown in Figures 8.7 and 8.8. The most conservative method was 3b, whereas the other methods all had about the same accuracy. The displacement accuracy is about the same for the 0.2% and the 0.4% case study structures, and was the best for the 12 story structures, especially at demand level 1.

The maximum drift was calculated at each time step, not from the maximum displacement as has been observed in other research [Cardone et al., 2009]. Because of this, the NLTHA drift values are more affected by higher modes at taller heights than they would be if calculated from maximum displacement. The drift values are depicted in Figures 8.11 and 8.12. For prediction, the drifts vary greatly between design methods. In the stiffer case study structures (i.e. $\theta_1 = 0.2\%$), Method 3b was the closest to the NLTHA results. For the more flexible case study structures (i.e. $\theta_1 = 0.4\%$), Method 3b often was overly conservative for the 8 and 12 story structures, but was the best prediction for the 4 story structure. The 8 and 12 story structures for $\theta_1 = 0.4\%$ were best predicted by Method 4, but Method 3a was close. This shows that Method 4 has a slight prediction advantage over Method 3a, but

may not be worth the computational expense. The predicted drift at the highest story is quite a bit higher than the other stories, which shows that more model development may be needed.

Figures 8.11 and 8.12 show the story shear predictions and analysis for all case study structures. Method 3b was the most accurate prediction for the stiffer structures as well as the 4 story structure with $\theta_2 = 0.4\%$. From the limited structures studied, this suggests that Method 3b is more accurate for predicting force in structures with lower periods (i.e. lower story drift values). In contrast, it should be noted that all of the other methods are more accurate than Method 3b for predicting the shear at the isolator level. For the more flexible structures, Method 3b is conservative, especially at the mid levels. In these cases, Methods 3b and 4 more closely follow the NLTH results.

None of the design methods were able to predict the distribution of the acceleration along the building height for any of the case study structures, as shown in Figures 8.13 and 8.14. The closest prediction occurred at the top story for Method 3b, but this method was off by roughly a factor of 2.5 at the base for the 8 story, $\theta_2 = 0.2\%$ structure. Again, it should be noted that the shear and acceleration values from the NLTHA should be treated with skepticism due to the acceleration spikes found in the modeling.

Overall, Method 3b was best for predicting drift and shear of less flexible structures ($\theta_1 = 0.2\%$), but not displacements. All of the other design methods provided accurate displacement predictions for all cases studied. Methods 1 and 2 were the overall least accurate design methods since they did not predict the trends of the analysis interstory drift and were very conservative in story shear and acceleration. Methods 3a and 4 gave very similar results in most cases, and were most differentiated for taller, more flexible structures, particularly in drift; those methods were between Methods 1,2 and Method 3b in terms of accuracy. None of the design methods were able to predict the story accelerations. It is recommended that the original design method (Method 1) be used for predicting the displacement of the system, and Method 3b be used for drift and shear predictions, noting that Method 3b will be conservative for more flexible structures.

The improvement of structural performance is beyond the scope of this research, but should be addressed in order to reduce the drift at the top stories. In order to obtain a more desirable structural stiffness and better control drifts due to higher modes, the proposed design process could be iterated. The design methods presented in this section have been explored through a brief study, and a more extensive study should be conducted before use of this design method. However, without further research, these design methods can serve as a basis for preliminary design.

8.5 Preliminary MDOF System Characterization

The behavior of the AVF bearings at this point has been studied in a parametric study (Chapter 4.4) and a design setting (Chapter 7.3) for both rigid and flexible SDOF systems. It is important to evaluate the behavior of AVF isolated systems for simple cases, such as the ones studied, in order to identify general patterns of behavior. However, only evaluating the behavior with SDOF models misses key phenomena that are present in real-world structures, such as the effects of higher modes on the structure. Therefore, the behavior of the AVF systems is evaluated again for the MDOF case study structures in order to give the most realistic representation of AVF bearing behavior.

The behavior comparison uses the case study systems outlined in Section 8.2.1, which were designed for a scale factor of 1, which corresponds to the MCE demand level. In addition to the isolators previously outlined, isolators with β_2 values ranging from 1 to 5 were also considered in the study. Each isolator had the same behavior at the first demand level (meaning the same α_1, $\Delta_{1,iso}$, R, and μ_1 as Table 8.2), but had a $\Delta_{2,iso}$, μ_2, and $T_{2,sys}$ which corresponded with the appropriate β_2 value. An example set of force-displacement curves for the AVF devices with varying β_2 can be seen in Figure 8.15.

The six case study structures defined in Section 8.2.1 were used for each of the isolators (i.e. $\beta_2 = 1 - 5$) because it was found that the structural design was seldom affected by changing β_2. The six case study structures, 5 different isolators ($\beta_2 = 1 - 5$), 3 scale factors, and 20 San Francisco ground motions resulted in 1,800 NLTHA. The parameters considered

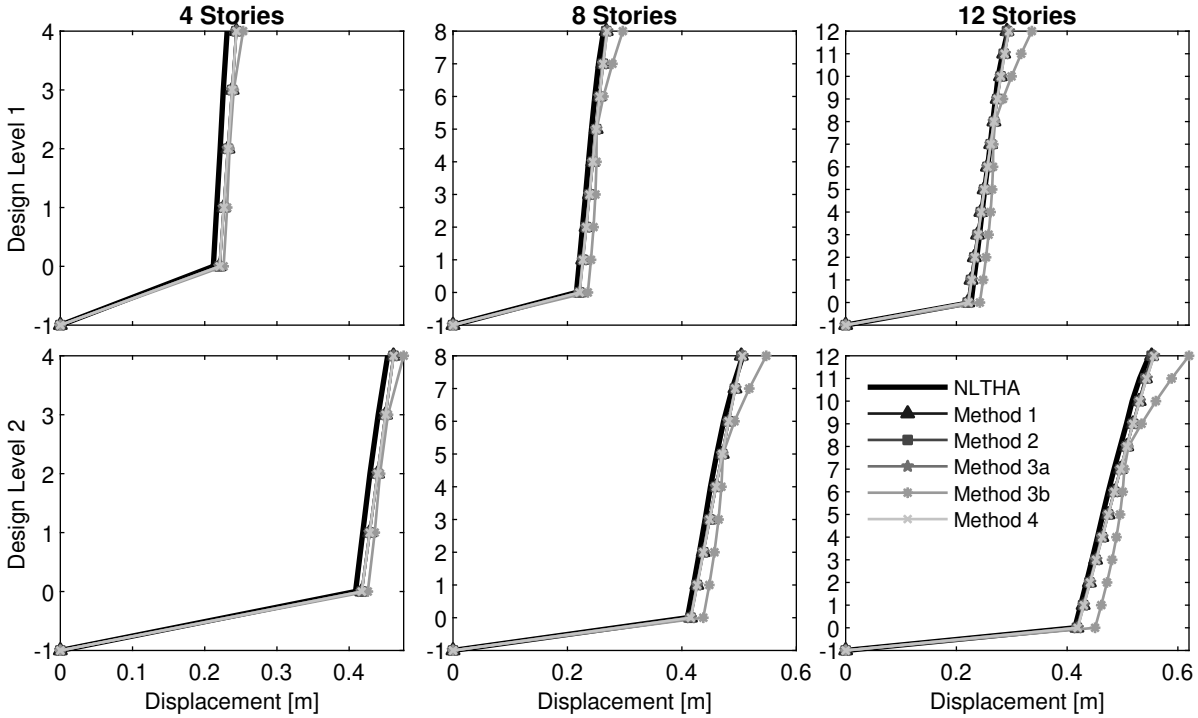

Figure 8.7: Comparison of design Methods 1-4 and analysis for maximum displacement at demand levels 1 and 2 ($\theta_1 = 0.2\%$).

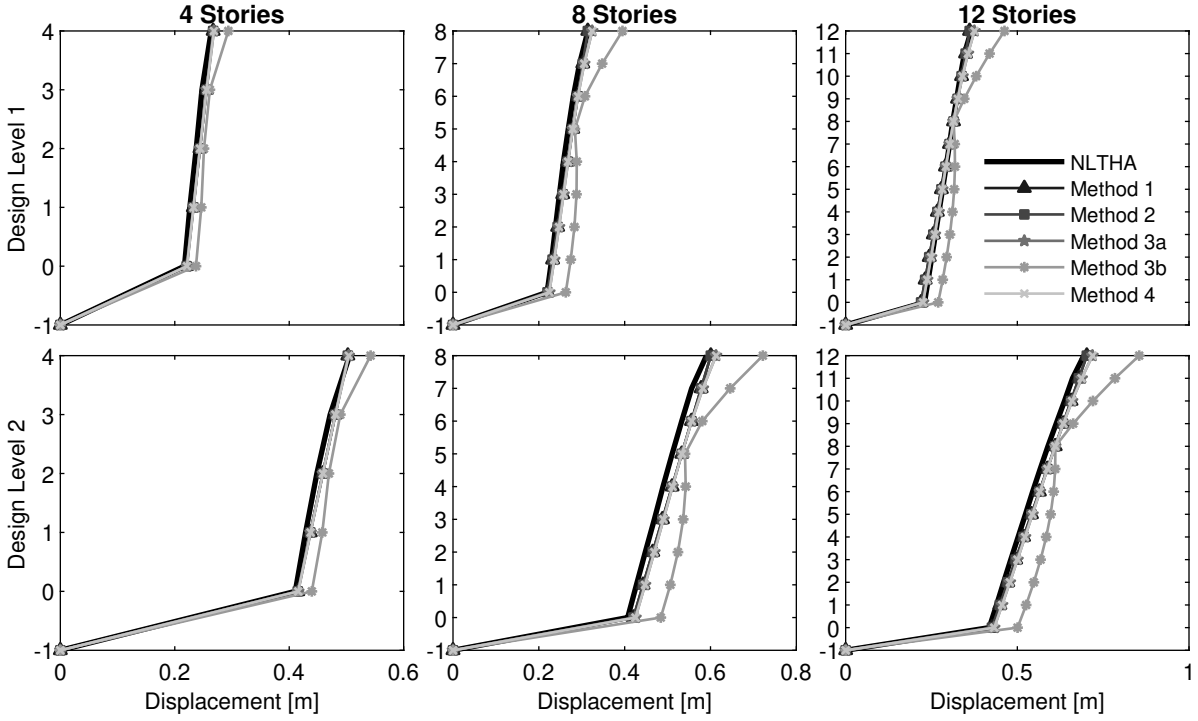

Figure 8.8: Comparison of design Methods 1-4 and analysis for maximum displacement at demand levels 1 and 2 ($\theta_1 = 0.4\%$).

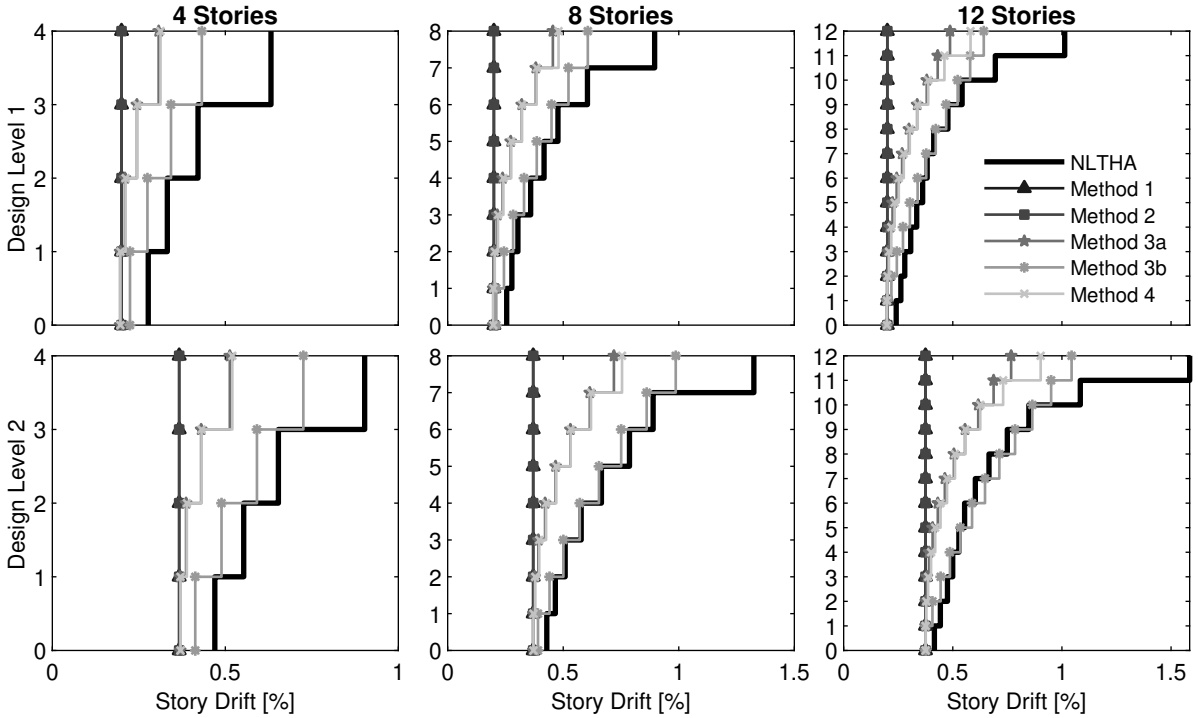

Figure 8.9: Comparison of design Methods 1-4 and analysis for maximum story drift at demand levels 1 and 2 ($\theta_1 = 0.2\%$).

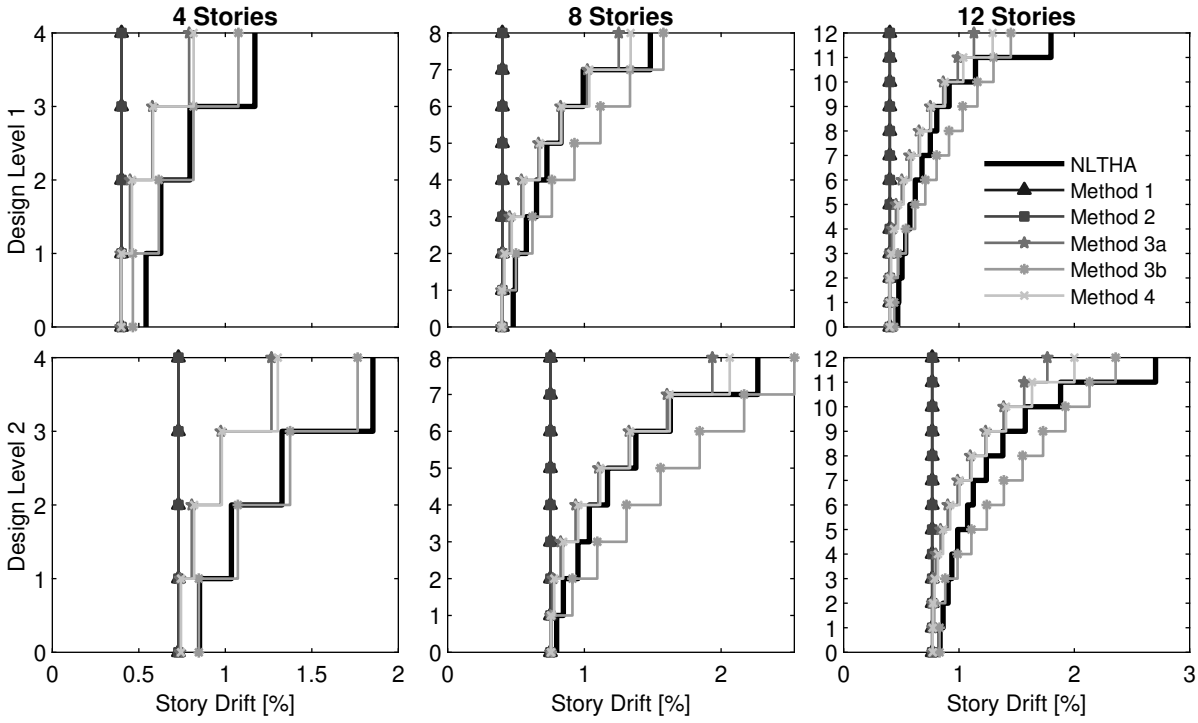

Figure 8.10: Comparison of design Methods 1-4 and analysis for maximum story drift at demand levels 1 and 2 ($\theta_1 = 0.4\%$).

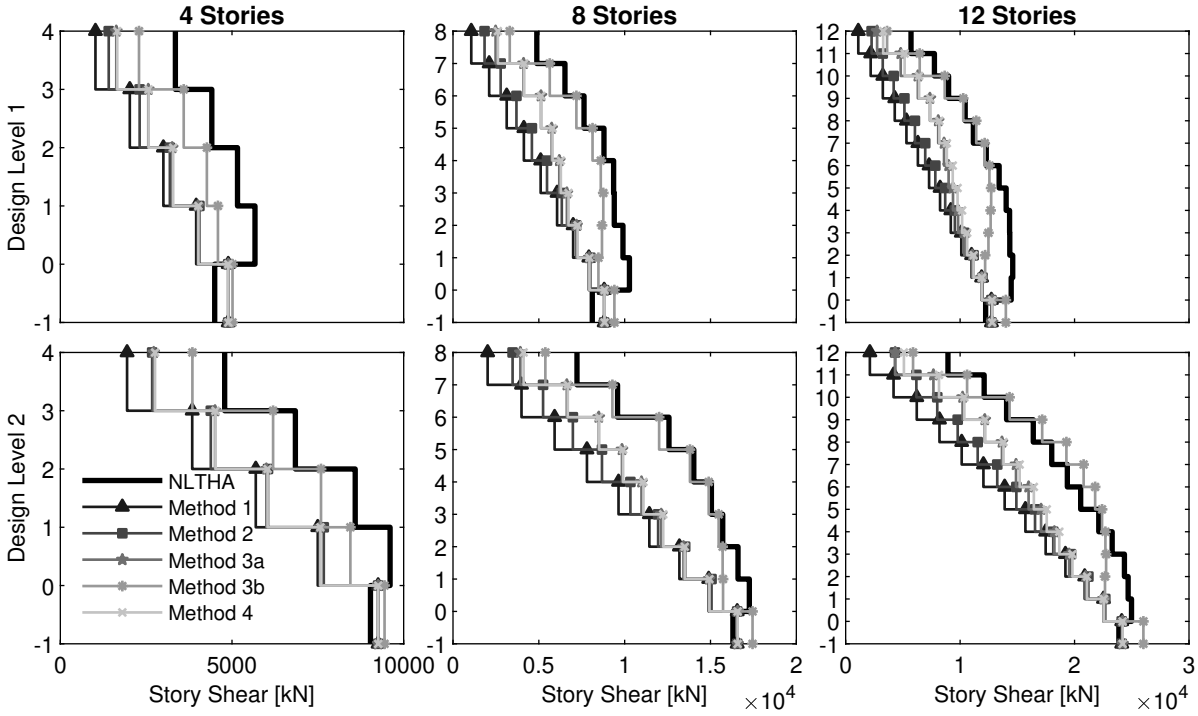

Figure 8.11: Comparison of design Methods 1-4 and analysis for maximum story shear at demand levels 1 and 2 ($\theta_1 = 0.2\%$).

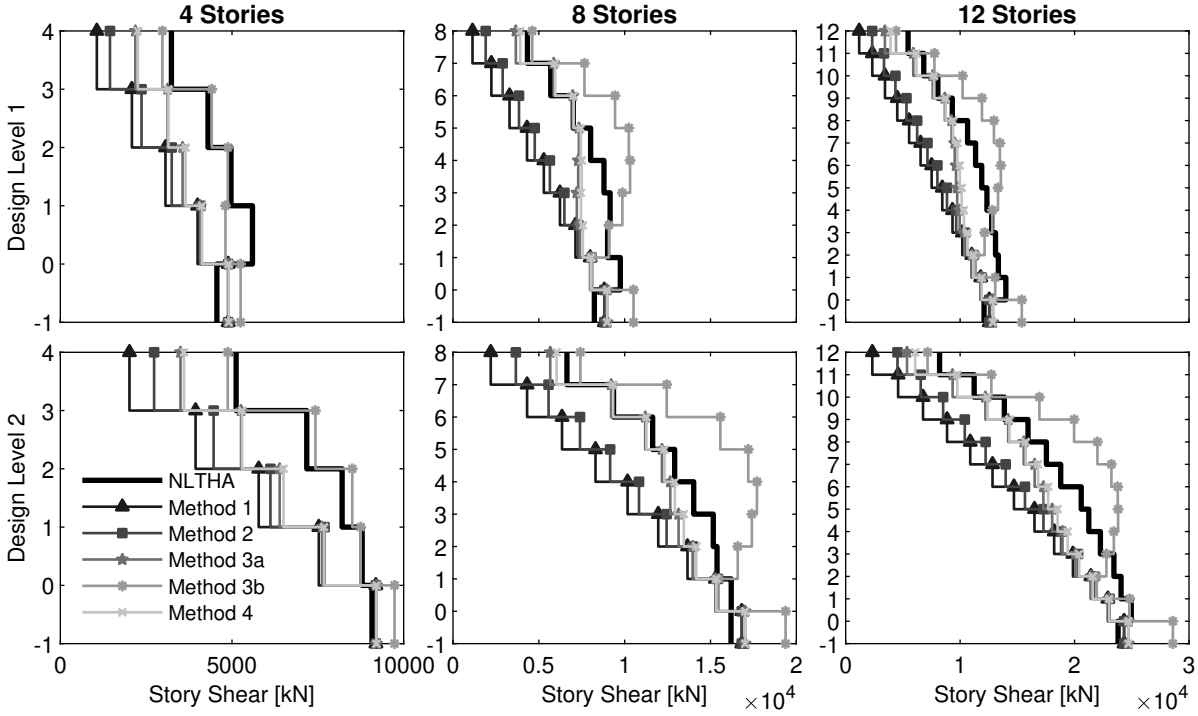

Figure 8.12: Comparison of design Methods 1-4 and analysis for maximum story shear at demand levels 1 and 2 ($\theta_1 = 0.4\%$).

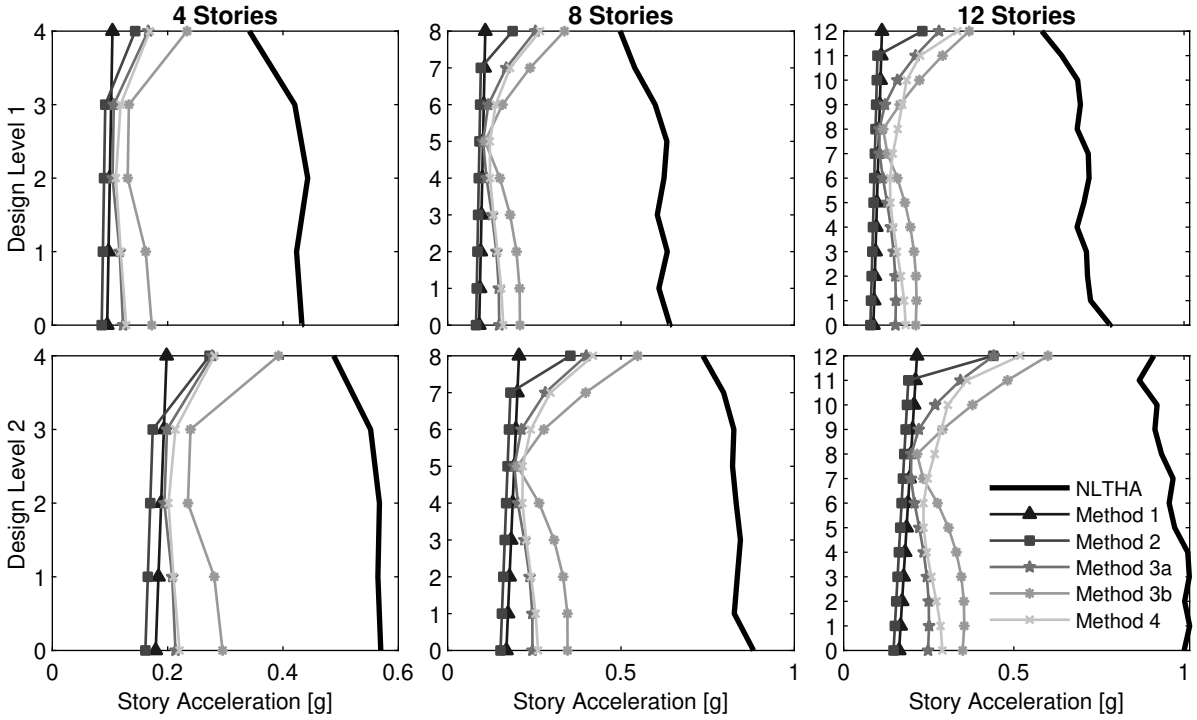

Figure 8.13: Comparison of design Methods 1-4 and analysis for maximum absolute acceleration at demand levels 1 and 2 ($\theta_1 = 0.2\%$).

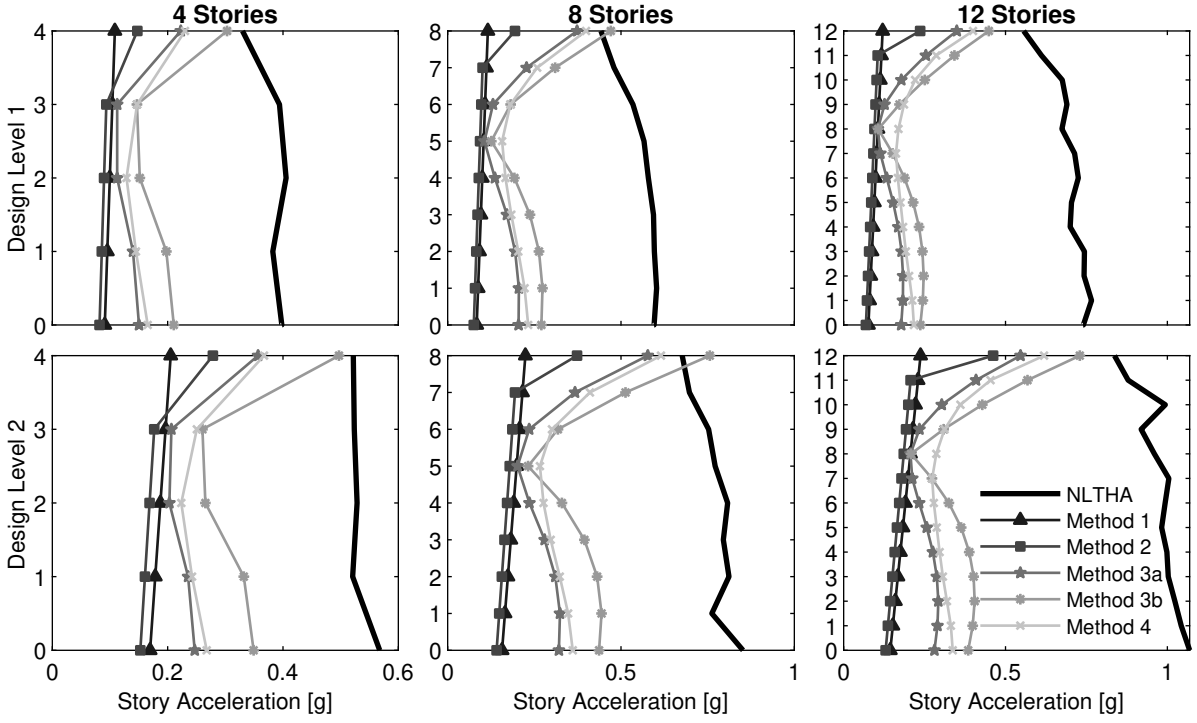

Figure 8.14: Comparison of design Methods 1-4 and analysis for maximum absolute acceleration at demand levels 1 and 2 ($\theta_1 = 0.4\%$).

Table 8.5: Isolator parameters considered in MDOF behavior comparison (Low:Step:High)

Scale Factor	β_2	θ_1 [%]	Number of Stories
1:1:3	1:1:5	0.2, 0.4	4:4:12

in this MDOF behavior comparison are summarized in Table 8.5.

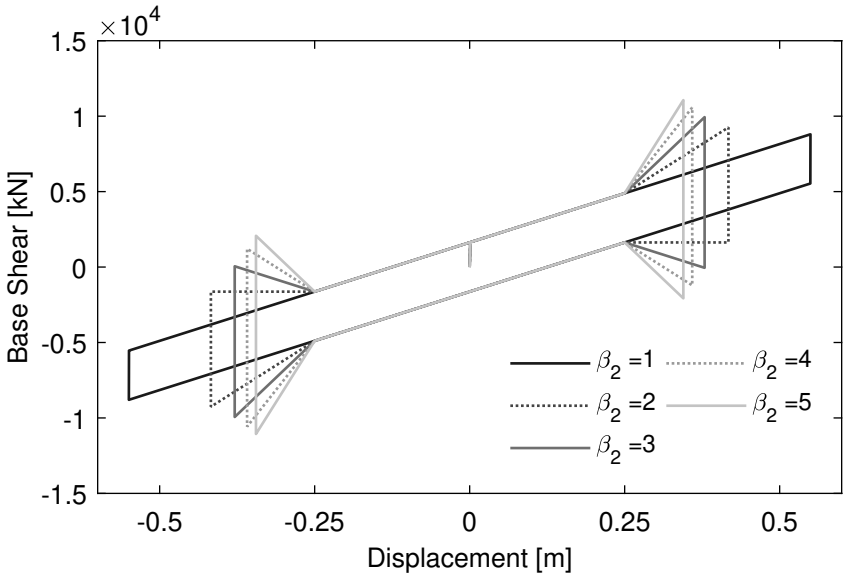

Figure 8.15: Example of compared isolator force-displacement curves (corresponding to the 4 story, $\theta_1 = 0.2\%$ case study structure)

8.5.1 At Isolator Level

The results from the brief MDOF parametric study for maximum isolator displacement, residual displacement, maximum base shear, and maximum acceleration at the isolator level can be seen in Figures 8.16 to 8.19. Similar trends to the SDOF parametric study previously conducted were observed, such as devices with higher β_2 values have higher maximum forces but lower maximum displacements. Figure 8.16 shows that the number of stories had almost no effect on the maximum isolator displacement for all cases considered. A large drop in

maximum displacement is observed at a scale factor of 3 between $\beta_2 = 1$ and 2; for the $\theta_1 = 0.4\%$ structures, the displacement dropped from around 2.5 m to 1.3 m. This is similar to what was observed in the SDOF parametric study, and again confirms that AVF devices have a large advantage over FP devices in extreme earthquakes by achieving a lower maximum displacement.

There are no clear trends for residual displacement, shown in Figure 8.17. Residual displacement is not greatly affected by number of stories for the $\theta_1 = 0.2\%$ case study structures, but increases for the 4 story, $\theta_1 = 0.4\%$ case. The residual displacement is moderately affected by β_2 and is very low for all of the devices, even at high scale factors. This behavior deviates from the trends in the SDOF parametric study (Chapter 4.4) and should therefore be examined in future research. In general, devices with higher β_2 values have higher residual displacements, but it depends on Δ_1 and the ground motion scale factor. For this combination of Δ_1 and ground motion scale factor, the AVF devices studied all have excellent re-centering capabilities, similar to the FP.

The base shear of the studied systems can be seen in Figure 8.18. In general, increasing β_2 corresponds to a small increase in base shear for all case study structures, except at scale factor 3. At this extreme shaking, the FP actually breaks the expected trend and has a higher force than $\beta_2 = 2$, as well as a higher maximum displacement. This again shows that an AVF bearing with $\beta_2 = 2$ can achieve significantly lower maximum displacement for a similar or lower maximum base shear at high seismic levels when compared to a FP. This also further affirms that $\beta_2 = 2$ is the optimal parameter choice for AVF bearings for balancing maximum displacement, base shear, and residual displacement demands, though this should be confirmed by examining a larger number of structures.

The absolute acceleration experienced at the isolator level is pictured in Figure 8.19. The acceleration follows an increasing linear trend for all cases studied, with greatest change between $\beta_2 = 1$ and 2 at scale factor 3. For the 12 story, $\theta_1 = 0.4\%$ structure, the acceleration increases from around 2 g to 3.5 g between $\beta_2 = 1$ and 2. Even though the base shear is lower for $\beta_2 = 2$, the acceleration is higher, thus juxtaposing the benefit of a lower maximum

force and displacement with an increase in acceleration. It should be noted again that the force and acceleration data should be treated with skepticism due to the numerical modeling errors previously discussed.

8.5.2 At Superstructure Level

The effect of the isolator type on the structural performance is shown in Figures 8.20 through 8.23. For each case studied, the smallest isolator and structure displacements were experienced by the isolators with $\beta_2 = 5$. As the flexibility of the structure increases, The displacement at the top of the structure converges for all devices studied, meaning that flexible structures isolated with higher β_2 values may experience higher interstory drifts.

This suggestion agrees with the data shown in Figure 8.21: an increase in drift occurs for increasing β_2, θ_1, and story height. The most significant difference in drift is the drop from about 4.2% to 2.2% between $\beta_2 = 1$ and 5 for the tallest, most flexible structure. Conversely, there is little difference in story drift between $\beta_2 = 1$ and 2 for the shortest, stiffest structure, yet there is a large difference in isolator displacement. This shows that there are some scenarios where the designer can achieve a savings in isolator displacement for a similar story drift profile. However, this increase in drift for increasing β_2 suggests that the design of structures isolated with high β_2 values should be adjusted accordingly to decrease the interstory drift.

The story shear and acceleration, shown in Figures 8.22 and 8.23, experience similar overall trends. Shear and acceleration increase for increasing β_2 and story height, and decrease for more flexible structures (i.e. higher θ_1). There is a greater difference between the force and acceleration at the ground floor for $\beta_2 = 1$ and 2 than the top floor, showing that the decrease in force and acceleration for AVF devices at the ground floor is somewhat lost up the height of the structure. These trends can serve as a basic understanding of the system behavior for shear and acceleration, but these studies should be replicated using a more reliable numerical model.

The observed story shear behavior is presented for a ground motion scale factor of one, or

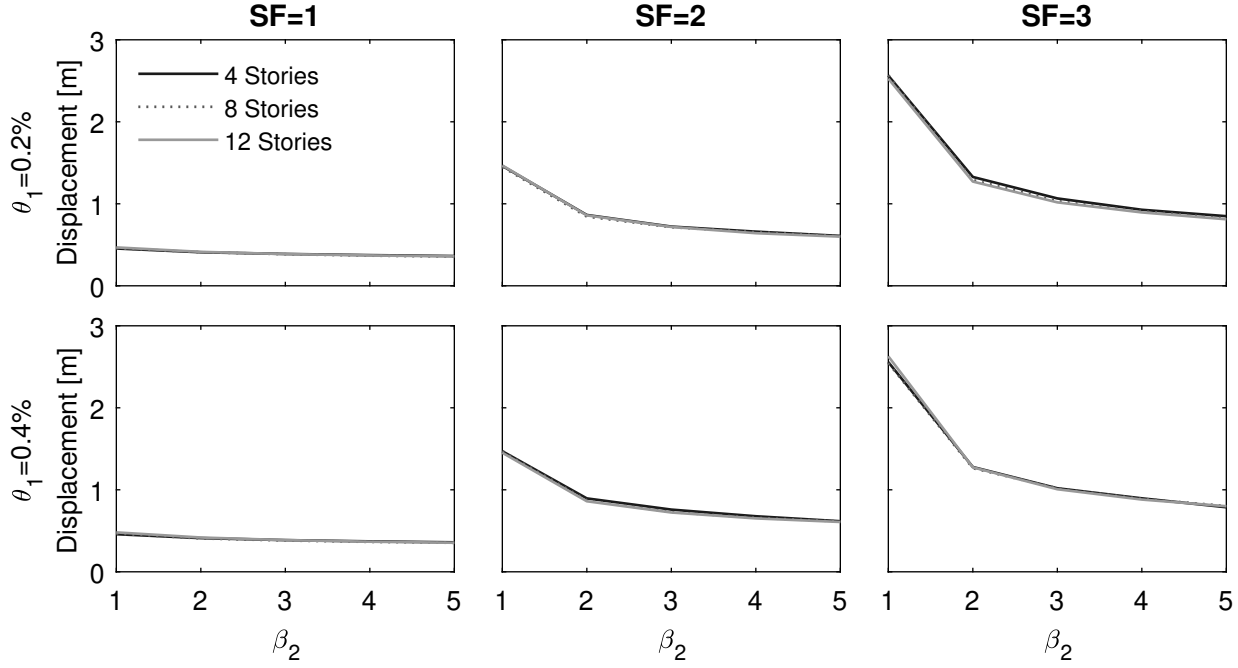

Figure 8.16: Behavior comparison of maximum isolator displacement for various AVF isolated MDOF systems

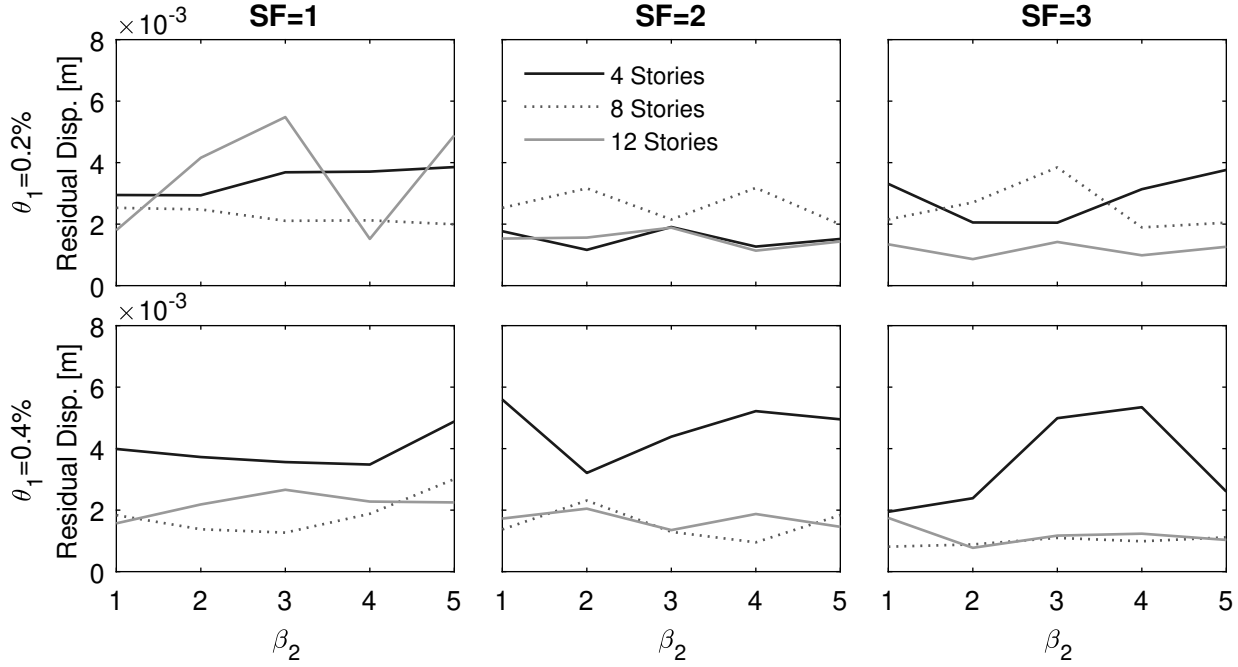

Figure 8.17: Behavior comparison of residual displacement for various AVF isolated MDOF systems

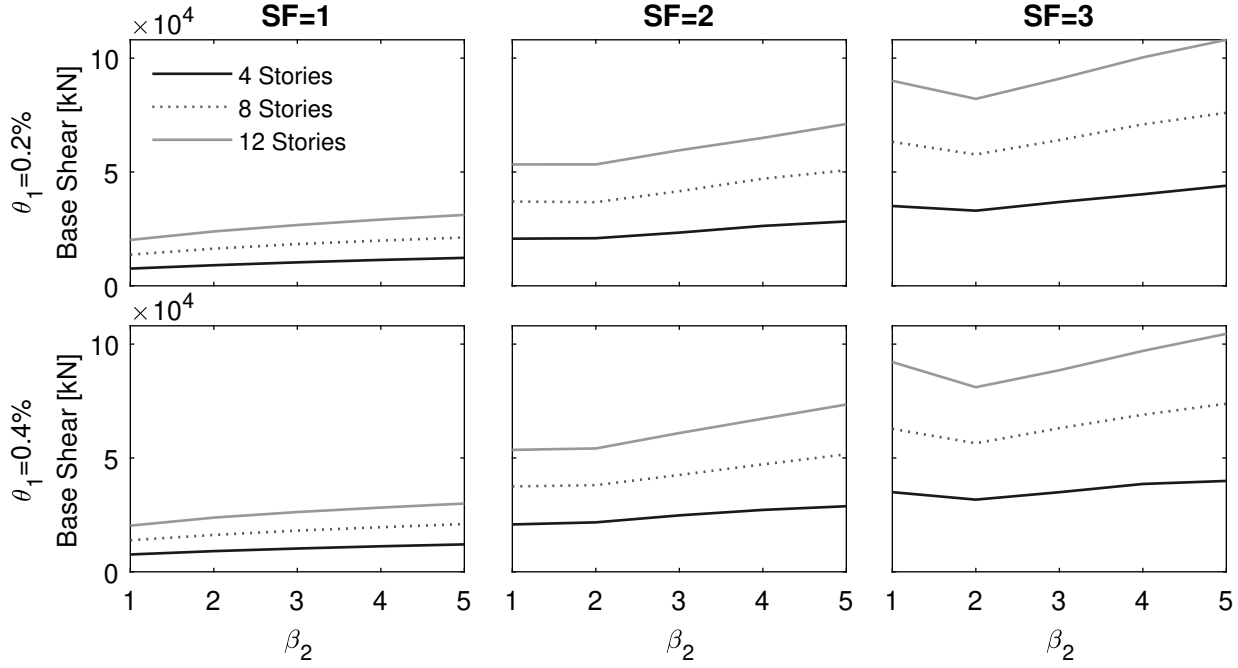

Figure 8.18: Behavior comparison of maximum base shear for various AVF isolated MDOF systems

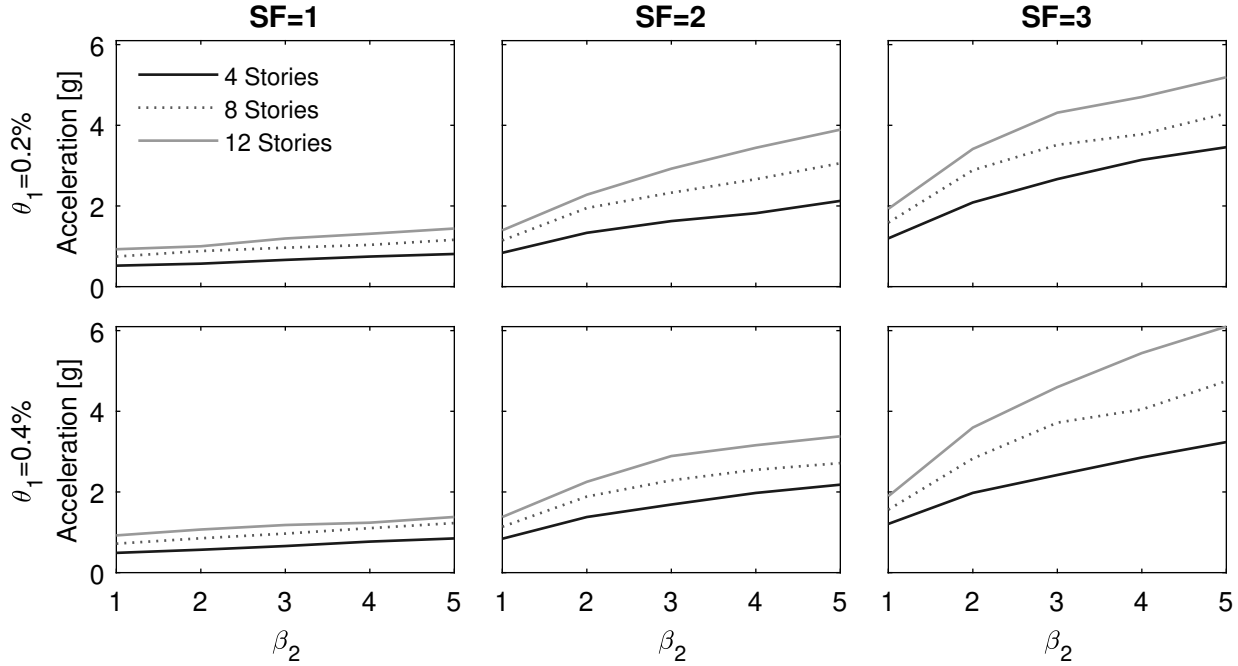

Figure 8.19: Behavior comparison of maximum absolute acceleration for various AVF isolated MDOF systems

the typical maximum considered earthquake demand. However, it may be realistic to consider events larger than the MCE (i.e. scale factor >1) because of effects that are currently not accounted for in the MCE, such as basin amplification or earthquake duration. For example, the city of Seattle sits on a deep sedimentary basin, which is known to increase the effect of seismic waves, and is expected to experience a magnitude 9 earthquake from the Cascadia Subduction Zone which will have a duration much longer than typical crustal earthquakes [Marafi et al., 2017]. Since the base shear for $\beta_2 = 1$ was actually larger than that for $\beta_2 = 2$ in this study, the severity of the earthquake must be considered by the designer and that devices with higher β_2 values may be a better option in extreme earthquake events.

The results presented in this section are preliminary as they do not cover a range of R, μ_1, $\Delta_{1,iso}$ like the SDOF parametric study, nor a broad range of case study structures. Similarly, the numerical model used was simplified and was shown to cause spurious acceleration spikes. However, the behaviors shown can serve as the basis for a preliminary understanding of how AVF isolation affects MDOF structures.

8.6 Conclusions

This chapter extended the design process of AVF devices to MDOF systems and explored many variations on the design. In a comparison of the design methods, it was found that Method 3b worked best for predicting the interstory drift and story shear for shorter, stiffer structures (i.e. 4, 8, and 12 stories with $\theta_1 = 0.2\%$ and 4 stories with $\theta_1 = 0.4\%$). The displacement was not predicted well by Method 3b for any scenario; the rest of the methods do an excellent job in predicting the displacement profile. For the case study structures not previously mentioned, Method 4 was the most accurate for predicting interstory drift and story shear, but there was little difference between Method 3a and Method 4, suggesting that Method 4 may not be worth the extra computational cost. None of the methods considered predicted acceleration well, but the acceleration and force from the NLTHA should be re-evaluated using a more robust numerical model, such as the one developed by [Yang et al., 2019a], due to the acceleration spikes found in the data.

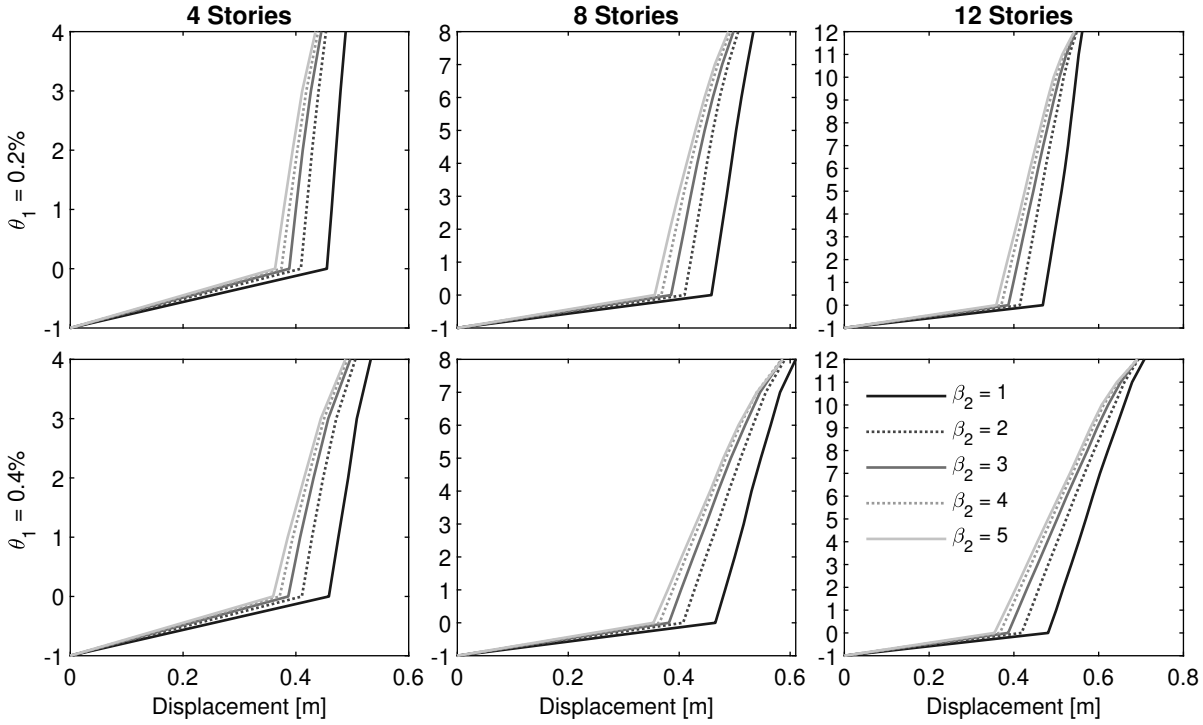

Figure 8.20: Behavior comparison of system displacement for various AVF isolated MDOF systems

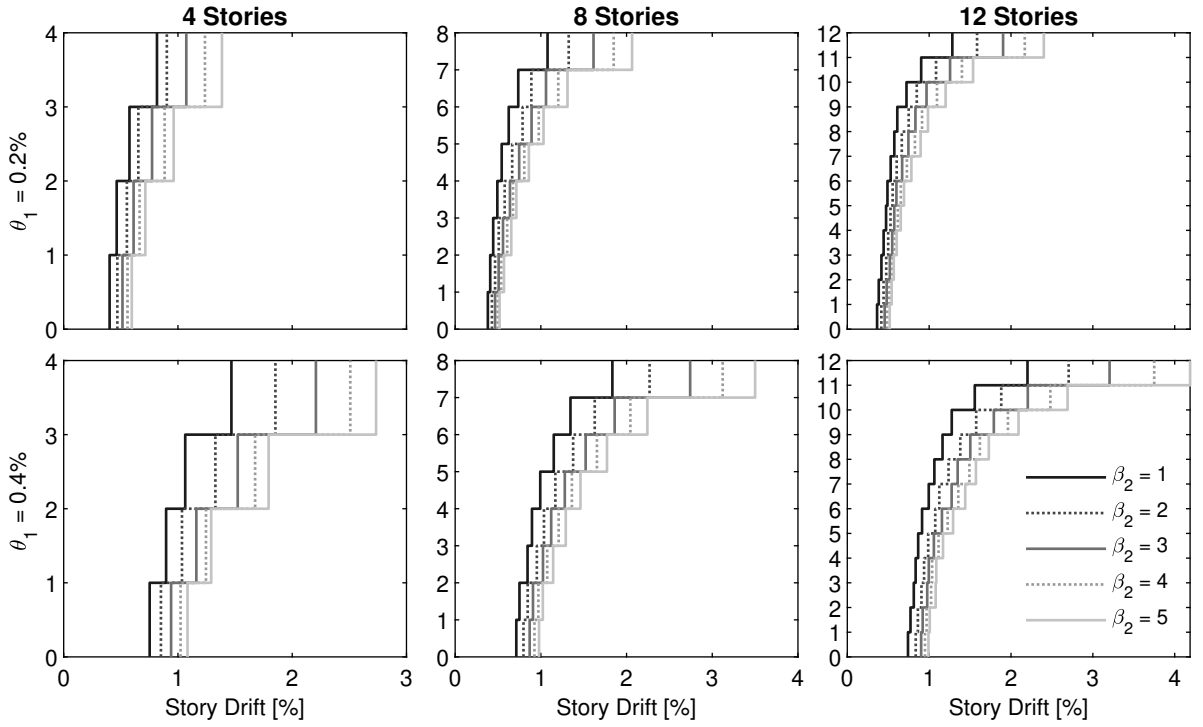

Figure 8.21: Behavior comparison of story drift for various AVF isolated MDOF systems

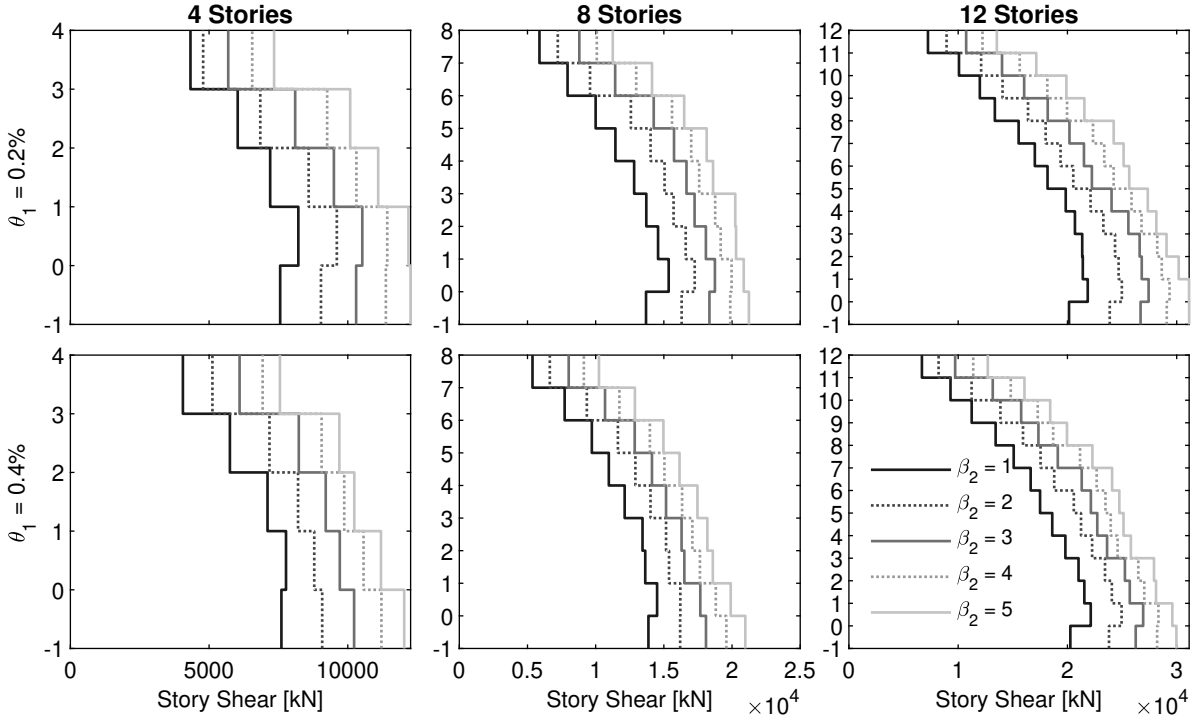

Figure 8.22: Behavior comparison of story shear for various AVF isolated MDOF systems

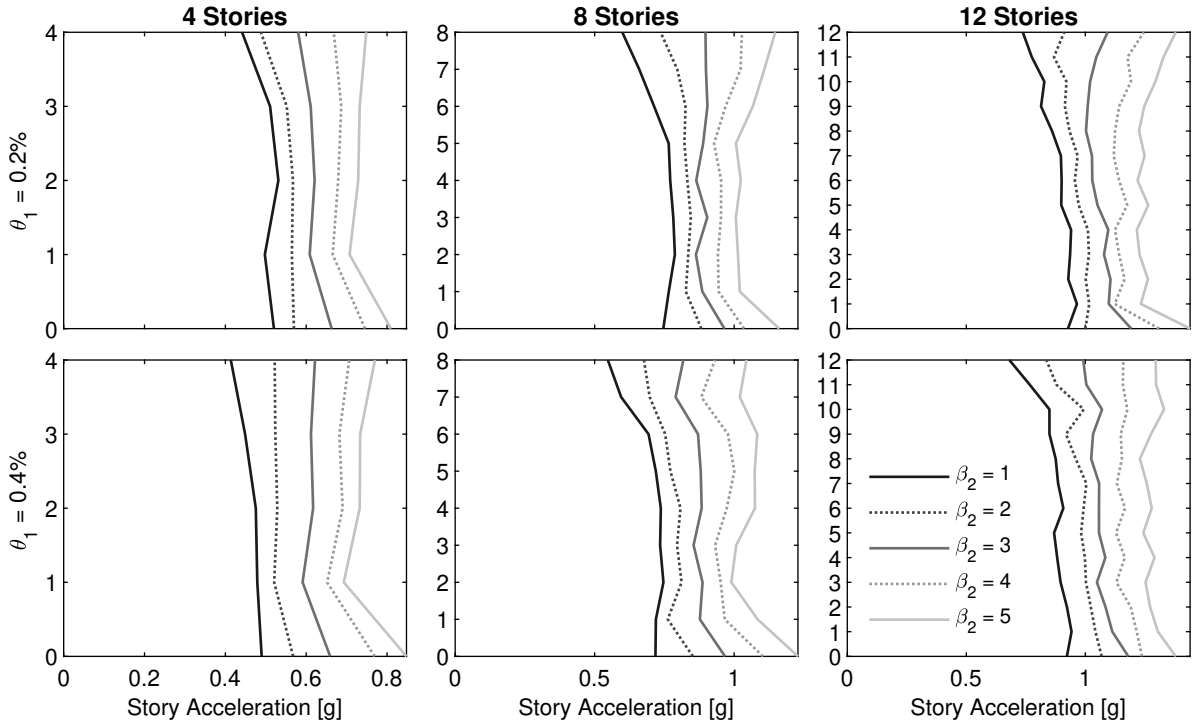

Figure 8.23: Behavior comparison of story absolute acceleration for various AVF isolated MDOF systems

The recommendations for design methods presented in this chapter are preliminary, and it is recommended that a robust study covering more realistic MDOF structures and additional AVF isolators and demand level be conducted in order to further verify the results. It is also recommended that other improvements to the MDOF design process be explored, such as including yielding of structural members and improving the structural behavior (i.e. lower interstory drift). Until the MDOF design process has been more robustly tested and expanded, it is suggested that it be used for preliminary design and in conjunction with NLTHA. Additional questions have been raised in the design verification process about the effects of higher modes in base isolated structures and modeling structural damping. More research should be conducted into higher mode effects in base isolated structures, as it is evident that they play a large role in structural behavior, especially interstory drift. The modeling of structural damping, especially for base isolated structures, is an open research topic and should be more thoroughly addressed by the research community.

This chapter also further characterized the behavior of the AVF device in the most realistic setting yet. The behavior comparison at the isolator level mirrored most of the findings of the behavior comparison in Chapter 4 and further showed that $\beta_2 = 2$ is the most optimal parameter for achieving low maximum and residual displacements for a maximum force comparable to an equivalent FP device. The system behavior comparison showed similarly validating behavior for β_2; all case study structures had similar interstory drifts for a large decrease in isolator displacement when compared to an equivalent FP. Overall, much remains to be explored regarding the behavior and design of AVF systems, but the trends and design processes suggested in this chapter should serve as a starting point for more thorough investigations.

Chapter 9

CONCLUSIONS AND RECOMMENDATIONS FOR FUTURE WORK

9.1 Overall Conclusions

The work in this thesis has made progress in achieving two main objectives: 1) exploring promising VFS devices, and 2) developing a design framework for VFS isolated structures. Under objective one, the mechanics and numerical modeling of an Adaptive VFS were characterized, and an extensive parametric study using many NLTH analyses explored the behavior of the AVF isolator. The second objective involved postulating a AVF bearing design process based on DDBD principles and validating the approach on both SDOF and MDOF base isolated systems. In order to design the AVF device, a reliable expression for estimating the isolator's damping ratio was derived and validated using many NLTH analyses. The design process for SDOF systems was tested by designing and analyzing AVF isolated rigid and flexible structures for various city spectra and parameter ranges. Lastly, the design process was adapted to MDOF isolated systems, and many design alternatives were presented. The overall conclusions from this work are presented below:

1. *Performance of the AVF Bearings*

   (a) *Isolating SDOF Systems*: The parametric study of the AVF bearings in Chapter 4 showed that the AVF device can on average achieve a lower maximum displacement than an equivalent FP while still exhibiting re-centering properties; this is especially evident at higher ground motion scale factors. When comparing AVF devices, a higher β_2, or the ratio between the second and first post-activation stiffness, gives a higher maximum force but a lower maximum displacement and

is less likely to re-center than devices with lower β_2 values. These trends were not greatly affected by changing the radius of curvature R or the initial friction μ_1, and were replicated in the SDOF and MDOF studies. It is recommended that a β_2 value of 2 provides the most favorable trade-off between maximum force, displacement, and residual displacement. This value of β_2 was shown to always have the ability nominally re-center no matter how large the input ground motion in a small study (Section 4.4.1). Additionally, $\beta_2 = 2$ has a large decrease in maximum displacement for a similar maximum force when compared to a FP.

(b) *Isolating MDOF Systems*: A more realistic comparison was conducted using MDOF case study structures, found in Section 8.5. The behavior comparison mirrored the findings of the SDOF study and showed further advantages to using an AVF bearing with $\beta_2 = 2$. For example, when a ground motion scale factor of 3 was considered, the FP had both a higher displacement and higher base shear when compared to an AVF bearing with $\beta_2 = 2$. When comparing the devices for a typical design demand (i.e. scale factor = 1), $\beta_2 = 2$ had slightly higher drifts, story shears, and accelerations than the equivalent FP. This shows that the designer must consider the intensity of the earthquake when choosing a device because AVF devices have clear advantages at high seismic levels.

(c) *In Achieving Adaptive Behavior*: A behavior comparison of the equivalently-designed AVF and FP isolated SDOF systems in Section 7.3 shows how the AVF can achieve multiple performance objectives. The compared AVF and FP devices were designed to have the same response at the first demand level, which was confirmed in NLTHA. At the second demand level, the comparison also confirmed findings from the SDOF parametric study: for both rigid and flexible structures, a higher β_2 value results in a higher maximum force and lower maximum displacement. Reaching the equivalent AVF maximum force on a FP device would require a large displacement capacity, which may not be available to a designer;

therefore, an AVF isolator may be useful to designers who work in regions of high seismicity and need a high capacity but are limited on bearing size.

2. *Validation of Damping Expression for AVF Bearings*: The expression derived to estimate the damping ratio of the AVF device was validated using over 600,000 NLTHA. When the NLTHA results and corresponding EVD expression values were organized by β_2, it was apparent that the expression was least effective at predicting the EVD ratio for a FP ($\beta_2 = 1$), and was most effective when $\beta_2 = 1.5$. When all of the NLTHA results and equation values were graphed together, it was shown that the expression can predict the trend of AVF device damping across a broad range of input parameters, and is therefore sufficiently accurate for design purposes.

3. *Validation of Design Process for AVF Isolated SDOF Systems*: The presented SDOF design process was tested by designing a variety of AVF and FP devices for the demands of different U.S. cities. The average force and displacement results from the NLTH analyses were compared to the design values at two different earthquake intensities (DBE and MCE), and overall, both the force and displacement were in agreement with the design values. The accuracy was better for rigid SDOF systems, but was still acceptable for flexible SDOF systems. Therefore, it was concluded that the proposed design process for AVF isolated SDOF systems is sufficient at predicting force and displacement at two different earthquake intensities.

4. *Presentation of Design Methods for AVF Isolated MDOF Systems*: The validated AVF design method was extended to MDOF systems. The original design method was effective at predicting displacements, but was not effective at predicting forces, drifts, or accelerations. Various design approaches taking into account the effects of higher modes were presented and compared for various case study structures. It was found that some methods were better than other methods in predicting story shear and drift, but no method was able to best predict the response for all systems studied. The

MDOF design method works well for predicting force and displacement at the isolator level, further validating the design process for the isolator itself, but the structural design process should be improved in order to better predict structural response.

5. *Use of an Alternative Numerical Model in Future AVF Studies*: The behavior of the AVF bearing in this thesis has been studied using a one dimensional model for isolating SDOF and MDOF systems. While a one dimensional model may capture some behavior patterns, it fails to capture other important behaviors, such as the change in displacement and acceleration NLTHA predictions due to bi-directional interaction of friction forces [Panchal and Jangid, 2009] or the effect of vertical accelerations on floor diaphragms and nonstructural elements [Ryan et al., 2012]. It is therefore recommended that further studies of AVF isolator use the 3D AVF isolator numerical model concurrently developed by [Yang et al., 2019a]. If a one dimensional model is used for future studies, it is recommended that the model incorporate Bézier curves into the AVF bearing hysteresis in order to help mitigate acceleration spikes [Wiebe and Christopoulos, 2011].

9.2 Recommendations for Future Work

While this thesis answered initial questions on AVF bearing and it's design process, much remains to be explored:

1. *A More Robust Behavior Investigation of AVF Isolated MDOF Structures*: Using the more advanced modeling techniques previously suggested, the behavior of the AVF isolators should be further evaluated in order to show a more realistic overall behavior. A large suite of realistic MDOF structures should be considered for a variety of isolators and input ground motions in order to ensure satisfactory behavior of AVF devices for MDOF structures with various periods. The studied ground motions should include both pulse and subduction zone characteristics, and be more severe in order to mimic demands amplified by basin effects and/or duration [Marafi et al., 2017]. Few tests

have been done subjecting a base isolated system to subduction zone earthquakes; two of those tests show good overall performance in FP and Lead-Rubber bearing systems [Ryan et al., 2012], but a lack of protection against high accelerations in nonstructrual elements [Sato et al., 2011]. It is important to characterize the behavior of the device for all types of input ground motions and consider the effects of nonstructural elements in order to ensure robustness of AVF bearing behavior.

2. *Experimental Testing*: A limited number of static and dynamic tests on bearings with a small change in friction (i.e. a low β_2 value) have been performed [Yang et al., 2019b]. The preliminary results demonstrate slight adaptive behavior in both the static and dynamic tests as well as agreement with the developed 3D VFS numerical model [Yang et al., 2019a]. These bearing tests only represent a small portion of possible VFS devices, and bearing tests for larger β_2 should be performed. Additionally, shake table tests with realistic structures are recommended for testing the device for more realistic scenarios.

3. *MDOF Design Method Improvements and Further Verification*: The design method for AVF isolated SDOF structures was quite accurate at predicting force and displacement of the isolator. The presented design MDOF design procedures were also effective at predicting the performance at the isolator level, but could be improved for predicting interstory drift, story shear, and acceleration up the height of the building. It was shown that the effects of higher modes in base isolated structures is quite prominent in structure behavior, and should be addressed with further research. Design improvements such as design aids for choosing input parameters, including material yielding in the superstructure, and improving overall structural performance could also be the focus of future research. These improvements should then be verified using a more advanced numerical model and a wide range of AVF isolators and realistic, MDOF structures.

4. *Modeling of Structural Damping*: There is little consensus in the research community on how to properly model damping in base isolated structures [Pant et al., 2013]. The difficulties of properly incorporating structural damping in this research were discussed in Chapter 8; in order to eliminate additional sources of error that may occur from an improper damping model, the MDOF structures were modeled with a 0% damping ratio. More research into structural damping in base isolated systems should be conducted. The advance in this topic can then be used to better refine the design and analysis of AVF isolated MDOF systems. It was also shown that structural damping magnified spurious acceleration effects.

5. *Extending Variable Friction Technology to Other Devices*: It has been shown that variable friction is effective on single sliding surface, but the combination of variable friction technology with existing bearings remains largely unexplored. Combining variable friction with a device that has multiple sliding surfaces, such as a TFP, would create an even more adaptive device and give a designer more control over the isolator's force-displacement curve. Another potential variable friction combination would be pre-stressing the AVF bearing, resulting in an adaptive device with tension capacity.

The preliminary results presented in this thesis show that the AVF bearing can achieve favorable behavior, making it a potentially viable alternative for performance based isolation systems. Further study will help move this device and others into practical application, reducing the risk of earthquake-related deaths one isolated structure at a time.

REFERENCES

Structural Design Actions - Part 5 - Earthquake Actions (2004). New Zealand, nzs 1170.5 edition. 74 pp (text), 80 pp (commentary).

Amadeo, K. (2019). "Haiti earthquake facts, its damage, and effects on the economy (January).

ASCE (2000). *Prestandard and Commentary for the Seismic Rehabilitation of Buildings*. FEMA, Washington, D.C., 356 edition (November).

ASCE 7-10 (2010). *Minimum Design Loads for Buildings and Other Structures*. American Society of Civil Engineers (October).

Barucci, C. (1990). *La casa antisismica [The antiseismic house]*. Gangemi (in Italian).

Becker, T. C., Bao, Y., and Mahin, S. A. (2017). "Extreme behavior in a triple friction pendulum isolated frame." *Earthquake Engineering & Structural Dynamics*, 46(15), 2683–2698.

Becker, T. C. and Mahin, S. A. (2012). "Experimental and analytical study of the bi-directional behavior of the triple friction pendulum isolator." *Earthquake Engineering & Structural Dynamics*, 41(3), 355–373.

Calvi, G. M. (2010). "Laquila earthquake 2009: reconstruction between temporary and definitive.

Calvi, P. M. and Calvi, G. M. (2018). "Historical development of friction-based seismic isolation systems." *Soil Dynamics and Earthquake Engineering*, 106, 14 – 30.

Calvi, P. M., Moratti, M., and Calvi, G. M. (2016). "Seismic isolation devices based on sliding between surfaces with variable friction coefficient." *Earthquake Spectra*, 32(4), 2291–2315.

Calvi, P. M. and Ruggiero, D. M. (2016). "Numerical modelling of variable friction sliding base isolators." *Bulletin of Earthquake Engineering*, 14(2), 549–568.

Cardone, D., Palermo, G., and Dolce, M. (2009). "Direct displacement-based design of buildings with different seismic isolation systems." *Journal of Earthquake Engineering*, 14(2), 163–191.

Casarotti, C. and Pavese, A. (2014). "Statistical results of a wide experimental campaign on full scale curved surface sliders (08).

Ceresa, G. M. C. P., Casarotti, C., Bolognini, D., and Auricchio, F. (2004). "Effects of axial force variation in the seismic response of bridges isolated with friction pendulum systems." *Journal of Earthquake Engineering*, 8(sup001), 187–224.

Chopra, A. (2014). *Dynamics of Structures: Theory and Applications to Earthquake Engineering*. Always Learning. Pearson Education Limited.

Constantinou, M., Mokha, A., and Reinhorn, A. (1990). "Teflon bearings in base isolation ii: Modeling." *Journal of Structural Engineering*, 116(2), 455–474.

EC8 (1998). *Eurocode 8: Design of Structures for Earthquake Resistance*. British Standard.

Fagà, E., Ceresa, P., Nascimbene, R., Moratti, M., and Pavese, A. (2015). "Modelling curved surface sliding bearings with bilinear constitutive law: effects on the response of seismically isolated buildings." *Materials and Structures*, 49(6), 2179–2196.

Fenz, D. and Constantinou, M. (2008a). "Mechanical behavior of multi-spherical sliding bearings." *Report No. MCEER-08-0007*, University of Buffalo (March).

Fenz, D. M. and Constantinou, M. C. (2006). "Behaviour of the double concave friction pendulum bearing." *Earthquake Engineering & Structural Dynamics*, 35(11), 1403–1424.

Fenz, D. M. and Constantinou, M. C. (2008b). "Modeling triple friction pendulum bearings for response-history analysis." *Earthquake Spectra*, 24(4), 1011–1028.

Fenz, D. M. and Constantinou, M. C. (2008c). "Spherical sliding isolation bearings with adaptive behavior: Theory." *Earthquake Engineering & Structural Dynamics*, 37(2), 163–183.

FIPIndustriale (2016). "Curved surface sliders.

Gupta, A. and Krawinkler, H. (1999). "Seismic demands for performance evaluation of steel moment resisting frame structures (sac task 5.4.3)." *Report No. 132*, The John A. Blume Earthquake Engineering Center, Stanford, CA (June).

Higashino, M. and Okamoto, S. (2015). *Response Control and Seismic Isolation of Buildings*. Routledge.

Hyakuda, T., Saito, K., Matsushita, T., Tanaka, N., Yoneki, S., Yasuda, M., Miyazaki, M., Suzuki, A., and Sawada, T. (2001). "The structural design and earthquake observation of a seismic isolation building using friction pendulum system.." *7th international seminar on seismic isolation, passive energy dissipation and active control of vibrations of structures.*, Assisi, Italy.

ICBO (1991). *ICBO: Uniform Building Code*.

Jacobsen, L. S. (1960). "Damping in composite structures." Vol. 2, Tokyo and Kyoto, Japan, 10291044.

Kelly, J. (1994). "The implementation of base isolation in the united states." Balkerma, Rotterdam.

Kelly, J. and Hodder, S. (1981). "Experimental study of lead and elastomeric dampers for base isolation systems." *Report No. UCB/EERC-81/16*, Earthquake Engineering Research Center (October).

Kelly, J., Skinner, M., and Beucke, K. (1980). "Experimental testing of an energy-absorbing base isolation system." *Report No. UCB/EERC-80/35*, Earthquake Engineering Research Center.

Lackey, K. (2017). "Deadliest earthquakes of the past decade (September).

Lee, D. and Constantinou, M. C. (2016). "Quintuple friction pendulum isolator: Behavior, modeling, and validation." *Earthquake Spectra*, 32(3), 1607–1626.

Lee, D. and Mediand, I. (1978). "Base isolation - an historical development and the influence of higher mode responses." *Bull. N.Z. National Society of Earthquake Engineering*, 11.

Logiadis, I., Zilch, K., and Meskouris, K. (1996). "Prestressed bearings in the seismic isolation of structures." *Eleventh World Conference on Earthquake Engineering*, E. S. Ltd., ed., number 1895.

Marafi, N. A., Eberhard, M. O., Berman, J. W., Wirth, E. A., and Frankel, A. D. (2017). "Effects of deep basins on structural collapse during large subduction earthquakes." *Earthquake Spectra*, 33(3), 963–997.

Marino, E. M., Nakashima, M., and Mosalam, K. M. (2005). "Comparison of european and japanese seismic design of steel building structures." *Engineering Structures*, 27(6), 827–840.

MATLAB (2018). "Version 9.4 (r2018a).

Mokha, A., Constantinou, M., and Reinhorn, A. (1990). "Teflon bearings in base isolation i: Testing." *Journal of Structural Engineering*, 116(2), 438–454.

Morgan, T. A. (2007). "The use of innovative base isolation systems to achieve complex seismic performance objectives.

Mostaghel, N. and Tanbakuchi, J. (1983). "Response of sliding structures to earthquake support motion." *Earthquake Engineering & Structural Dynamics*, 11(6), 729–748.

Murnal, P. and Sinha, R. (2002). "Earthquake resistant design of structures using the variable frequency pendulum isolator." *Journal of Structural Engineering*, 128(7), 870–880.

Naeim, F. and Kelly, J. (1999). *Design of Seismic Isolated Structures*. John Wiley & Sons.

Nagarajaiah, S. and Xiaohong, S. (2000). "Response of base-isolated USC hospital building in northridge earthquake." *Journal of Structural Engineering*, 126(10), 1177–1186.

Panchal, V. R. and Jangid, R. S. (2009). "Seismic response of structures with variable friction pendulum system." *Journal of Earthquake Engineering*, 13(2), 193–216.

Pant, D. R., Wijeyewickrema, A. C., and ElGawady, M. A. (2013). "Appropriate viscous damping for nonlinear time-history analysis of base-isolated reinforced concrete buildings." *Earthquake Engineering & Structural Dynamics*, 42(15), 2321–2339.

Petrini, L., Maggi, C., Priestley, M. J. N., and Calvi, G. M. (2008). "Experimental verification of viscous damping modeling for inelastic time history analyzes." *Journal of Earthquake Engineering*, 12(sup1), 125–145.

Pettinga, J. D. and Priestley, M. J. N. (2005). "Dynamic behaviour of reinforced concrete framces designed with direct displacement-based design." *Journal of Earthquake Engineering*, 9(sup2), 309–330.

Pietra, D., Pampanin, S., Mayes, R., Wetzel, N., and Feng, D. (2015). "Design of base-isolated buildings: An overview of international codes." 48, 118–135.

Priestley, N., Calvi, M., and Kowalsky, M. (2007a). *Displacement-Based Seismic Design of Structures*. IUSS Press.

Priestley, N., Calvi, M., Petrini, L., and Maggi, C. (2007b). "Effects of damping modelling on results of time-history analysis of rc bridges.

Reys, M. (1993). "An introduction to seismic isolation by r.i. skinner, w.h. robinson and g.h. mcverry." *Strain*, 29(3), 99–100.

Robinson, W. H. (1982). "Lead-rubber hysteretic bearings suitable for protecting structures during earthquakes." *Earthquake Engineering & Structural Dynamics*, 10(4), 593–604.

Roeder, C., Stanton, J., and W. Taylor, A. (1990). "Fatigue of steel-reinforced elastomeric bearings." *Journal of Structural Engineering*, 116.

Rosenblueth, N. N. E. (1971). *Fundamentals of Earthquake Engineering*. Englewood Cliffs, N.J: Prentice-Hall.

Roussis, P. C. (2009). "Study on the effect of uplift-restraint on the seismic response of base-isolated structures." *Journal of Structural Engineering*, 135(12), 1462–1471.

Roussis, P. C. and Constantinou, M. C. (2006). "Uplift-restraining friction pendulum seismic isolation system." *Earthquake Engineering & Structural Dynamics*, 35(5), 577–593.

Ryan, K., Dao, N., Sato, E., Sasaki, T., and Okazaki, T. (2012). "Nees/e-defense base-isolation tests: Interaction of horizontal and vertical response." *15 WCEE*, Lisboa.

Ryan, K., R. Button, M., and L. Mayes, R. (2019). "Asce 7-16 lateral force distribution equations for static design of seismically isolated buildings." *Journal of Structural Engineering (United States)*, 145.

Ryan, K. L. and Polanco, J. (2008). "Problems with rayleigh damping in base-isolated buildings." *Journal of Structural Engineering*, 134(11), 1780–1784.

Sarkisian, M., Lee, P., Hu, L., Doo, C., Zayas, V., Constantinou, M., and Bachman, R. (2012). "Property verification of triple pendulum seismic isolation bearings." *20th Analysis and Computation Specialty Conference*, American Society of Civil Engineers, 12–24 (mar).

Sarlis, A. and Constantinou, M. (2013). "Model of triple friction pendulum bearing for general geometric and frictional parameters and for uplift conditions." *Earthquake Engineering & Structural Dynamics*, 45.

Sato, E., Furukawa, S., Kakehi, A., and Nakashima, M. (2011). "Full-scale shaking table test for examination of safety and functionality of base-isolated medical facilities." *Earthquake Engineering & Structural Dynamics*, 40(13), 1435–1453.

SEAOC (1985). *Tentative lateral force requirements, Blue Book*. Structural Engineers Association of California.

Timsina, S. (2017). "A study of variable friction base isolation systems." M.S. thesis, University of Washington, Civil and Environmental Engineering, More Hall, Seattle, WA 98195.

Timsina, S. and Calvi, P. M. (2018). "Variable friction base isolation systems: Seismic performance and preliminary design." *Journal of Earthquake Engineering*, 1–24.

Touaillon, J. (1870). "Improvement in buildings. (February).

Tsai, C. S., Lin, Y. C., and Su, H. C. (2010). "Characterization and modeling of multiple friction pendulum isolation system with numerous sliding interfaces." *Earthquake Engineering & Structural Dynamics*, 39(13), 1463–1491.

UN (2017). "Global humanitarian overview 2017. Office for the Coordination of Humanitarian Affairs.

Warn, G. P. and Ryan, K. L. (2012). "A review of seismic isolation for buildings: Historical development and research needs." *Buildings*, 2(3), 300–325.

Wiebe, L. and Christopoulos, C. (2010). "Characterizing acceleration spikes due to stiffness changes in nonlinear systems." *Earthquake Engineering & Structural Dynamics*, 39(14), 1653–1670.

Wiebe, L. and Christopoulos, C. (2011). "Using bézier curves to model gradual stiffness transitions in nonlinear elements: Application to self-centering systems." *Earthquake Engineering & Structural Dynamics*, 40(14), 1535–1552.

Wolff, E. and Constantinou, M. (2004). "Experimental study of seismic isolation systems with emphasis on secondary system response and verification of accuracy of dynamic response history analysis methods." *Report No. MCEER-04-0001*, University at Buffalo, State University of New York (January).

Yang, T., Calvi, P. M., and Wiebe, R. (2019a). "Numerical implementation and experimental validation of the behavior of variable friction sliding base isolators. Submitted.

Yang, T., Ozcamur, U., Calvi, P. M., Wiebe, R., Bruschi, E., Quaglini, V., Sucuoglu, H., Lanese, I., and Pavese, A. (2019b). "Experimental investigation of the behavior of variable friction base isolation systems." *7th ECCOMAS Thematic Conference on Computational Methods in Structural Dynamics and Earthquake Engineering*, M. F. M. Papadrakakis, ed., Crete, Greece.

Zayas, V. (1987). "Earthquake protective column support (February).

Zayas, V., S. Low, S., Mokha, A., and Imbsen, R. (1987). "The fps earthquake resisting system experimental report." *Report no.*, Earthquake Engineering Research Center (01).

Zayas, V. A., Low, S., Mokha, A. S., and Imbsen, R. A. (2001). *Seismic Isolation of Benicia-Martinez Bridge*. American Society of Civil Engineers, 1–6.

Zekioglu, A., Darama, H., and Erkus, B. (2009). "Performance-based seismic design of a large seismically isolated structure: Istanbul sabiha gken international airport terminal building." 409–427.

Appendix A

ADDITIONAL EQUIVALENT VISCOUS DAMPING RESULTS

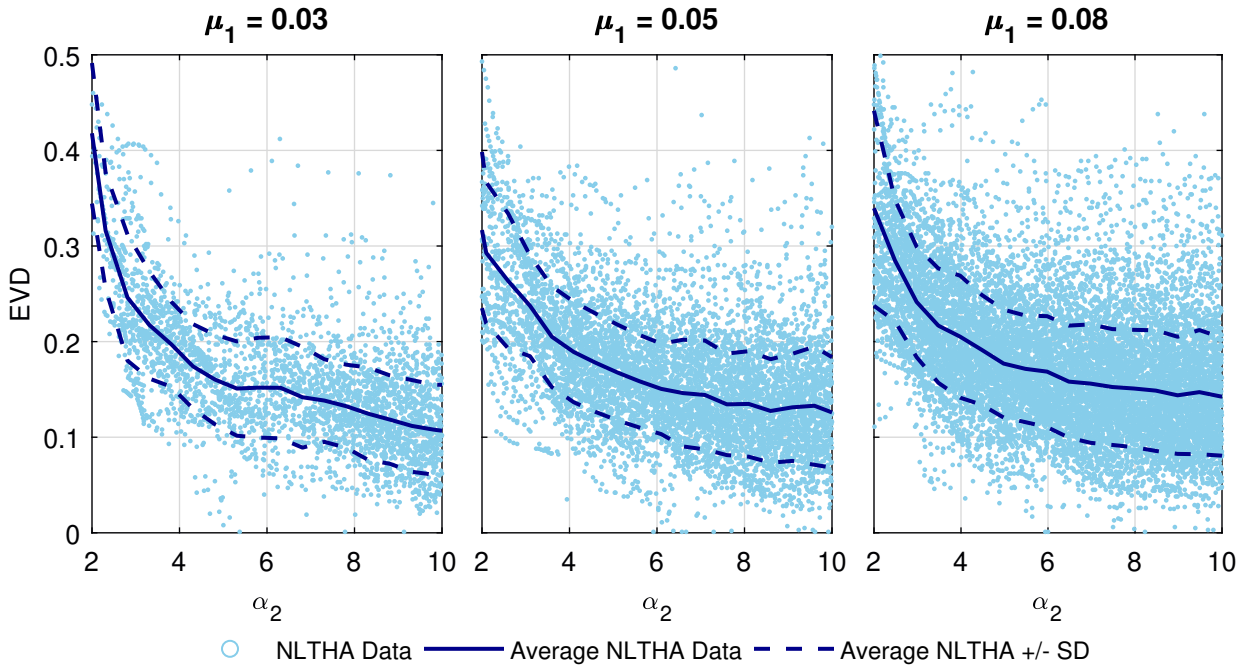

(a)

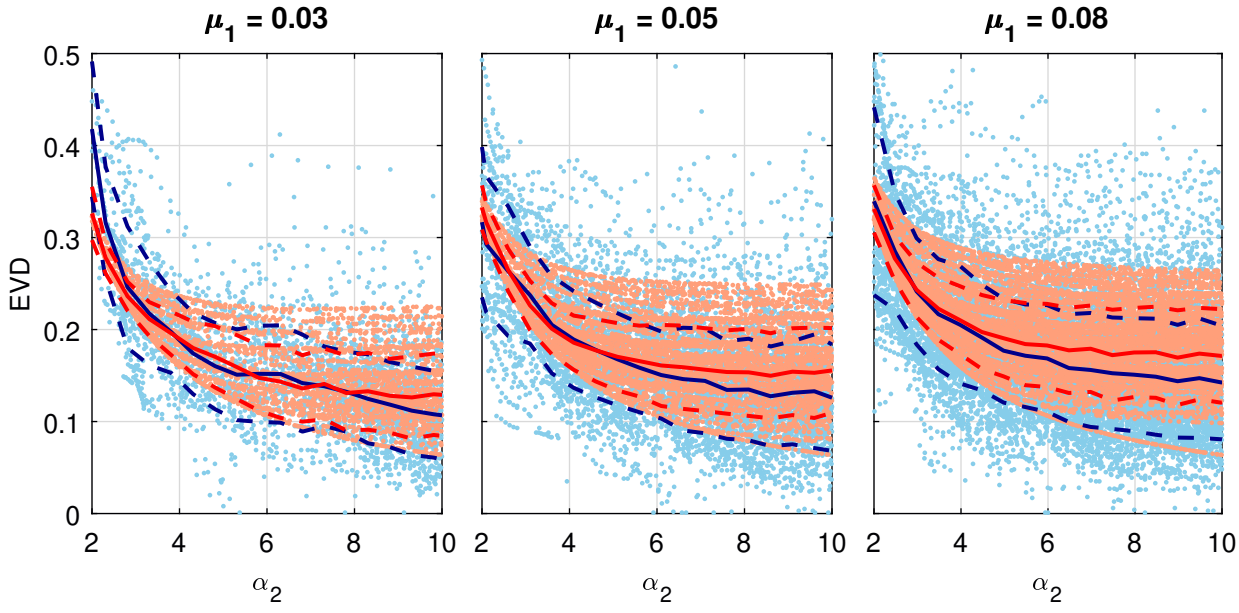

(b)

Figure A.1: (a) all NLTHA data and (b) including EVD equation values grouped by μ_1

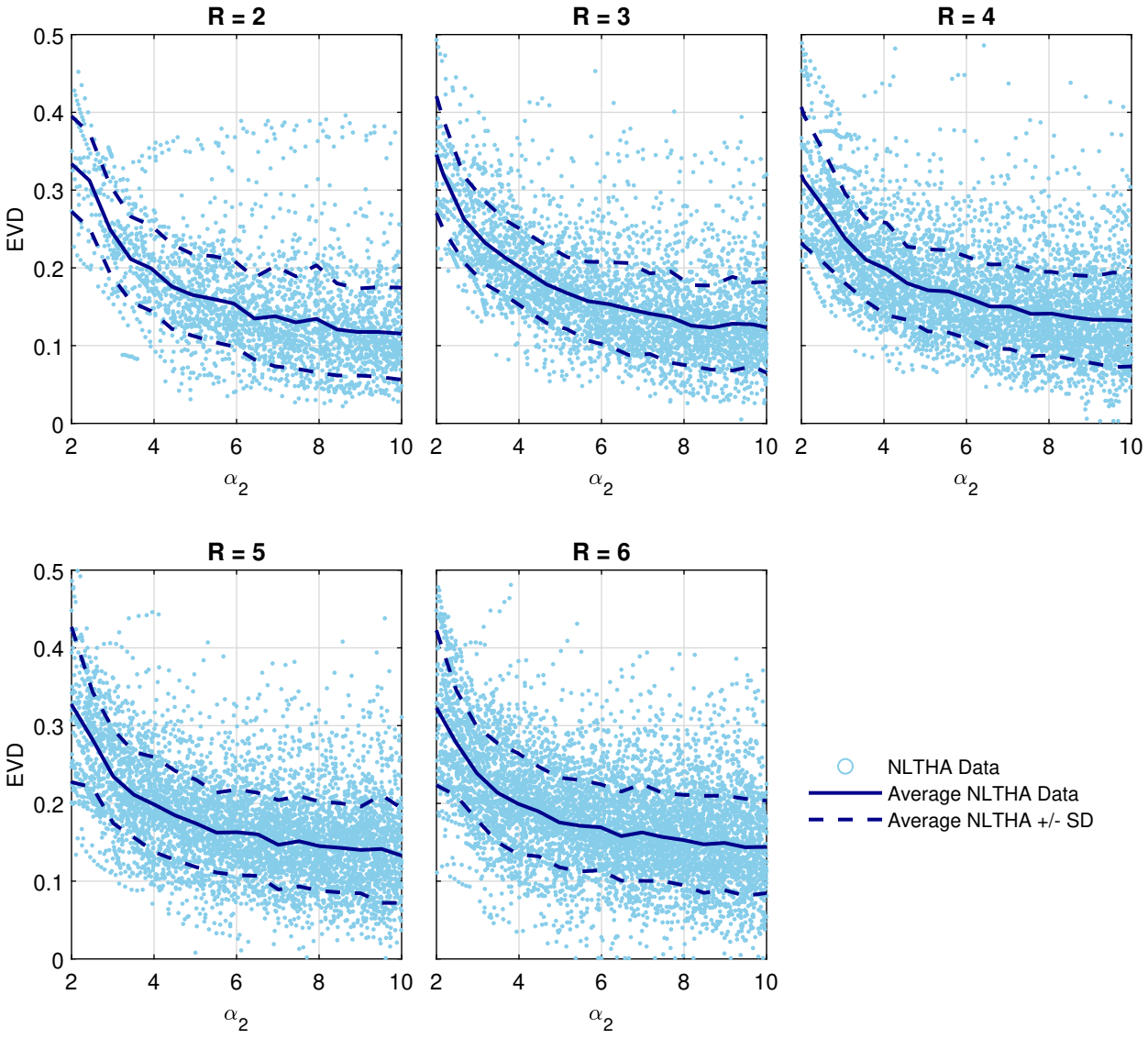

(a)

Figure A.2: (a) all NLTHA data and (b) including EVD equation values grouped by R

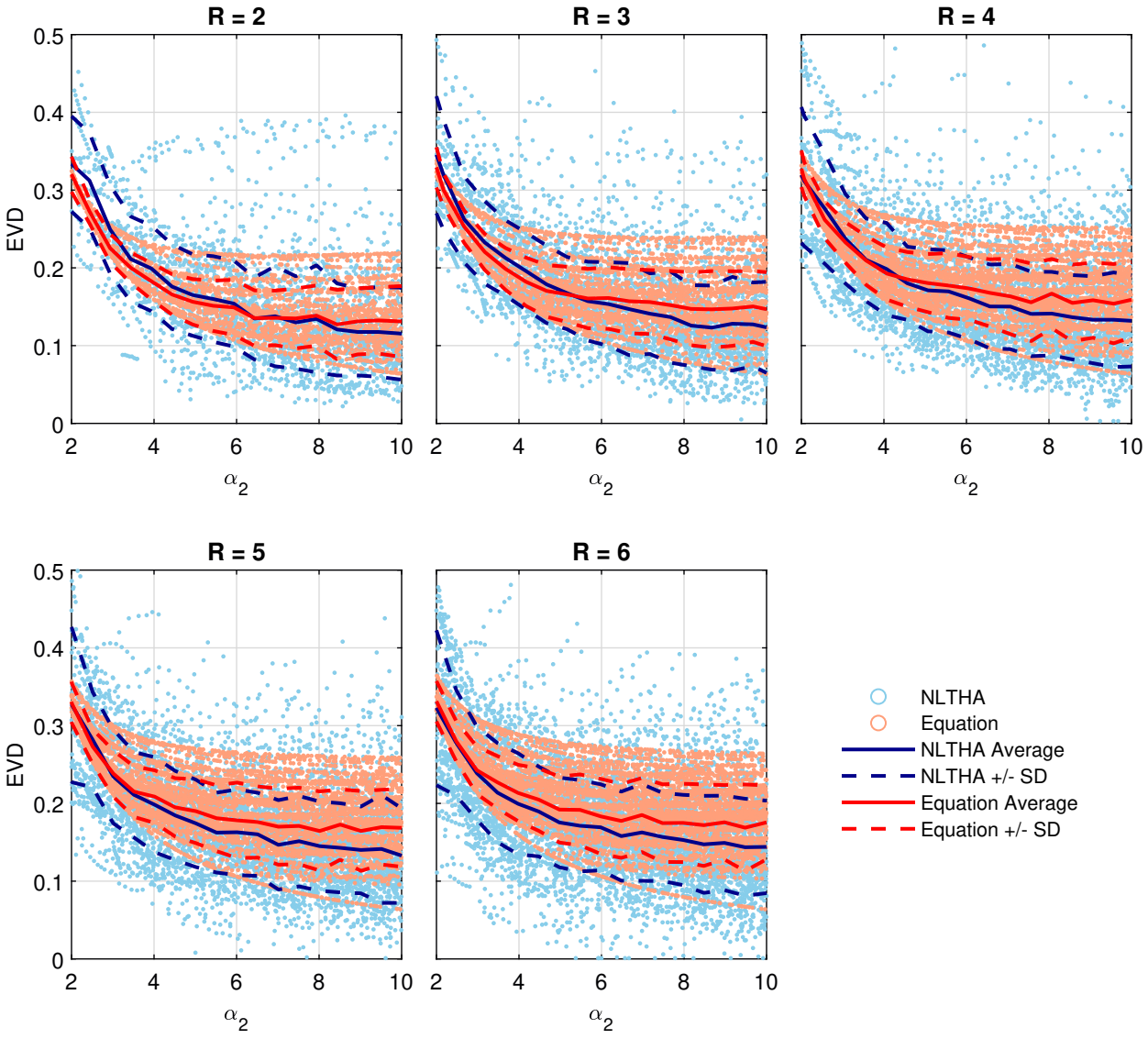

(b)

Figure A.2: (a) all NLTHA data and (b) including EVD equation values grouped by R